The Rise and Fall of Structure in Physics: Polaritonic Photonic Crystals, Melting, and Min-Protein Oscillations

by

Kerwyn Casey Huang

B.S., Physics and Mathematics
California Institute of Technology (1998)
M.Phil., Physics
University of Cambridge (1999)

Submitted to the Department of Physics
in partial fulfillment of the requirements for the degree of

Doctor of Philosophy

at the

MASSACHUSETTS INSTITUTE OF TECHNOLOGY

[Sept. 2004]

August 2004

Author .....
Department of Physics
August 6, 2004

Certified by .....
John D. Joannopoulos
Professor
Thesis Supervisor

Accepted by .....
Thomas J. Greytak ~~Marc A. Kastner~~
Assoc. Head, Department of Physics

The Rise and Fall of Structure in Physics: Polaritonic Photonic Crystals, Melting, and Min-Protein Oscillations

by

Kerwyn Casey Huang

Submitted to the Department of Physics
on August 6, 2004, in partial fulfillment of the
requirements for the degree of
Doctor of Philosophy

Abstract

This thesis is a compilation of theoretical and computational work in condensed matter physics related to three topics in structure development. First, I study photonic crystals composed of polaritonic media, focusing on the unique features of the band structures and Bloch states in dispersive media with and without losses. I discuss three novel localization phenomena in these structures: node switching, flux expulsion, and negative effective permeability. Second, I examine the importance of surface interfaces to melting using density functional theory. I demonstrate that single-layer coatings of Gallium Arsenide on Germanium and vice versa have a huge impact on the substrate melting temperature, causing superheating and induced melting, respectively. Finally, I develop reaction-diffusion and stochastic models of the Min-protein oscillations in bacteria that reproduce all main experimental observations. These models explain the origin of instability that ultimately causes dynamic pattern formation and have successfully been used to predict nucleotide binding rates in *E. coli*. In round cells, I provide evidence that oscillations can be used as a general mechanism for protein targeting and detecting the cell's geometry.

Thesis Supervisor: John D. Joannopoulos
Title: Professor

Figure 0-1: The magnetic field intensity of a Bloch state of an infinite polaritonic photonic crystal of the unit cell shown. The geometry of the polaritonic medium ($LiTaO_3$) is chosen to localize the field inside the structure when the frequency is near a Mie resonance. (see Chapters 2-4)

Acknowledgments

If a certain mustachioed, cigar-smoking comedian were to read this thesis, he would probably conclude: "A child of five would understand this. Send someone to fetch a child of five." Be that as it may, a lot of blood, sweat, and tears has gone into this work, and not just my own (although I have obtained a few gray hairs on its behalf).

To my supervisor, John Joannopoulos, who has been over the course of five years any and all of teacher, mentor, confidante, and friend, you have truly provided me with the tools to greet any challenge with the greatest of confidence and an air of excitement as I wait for the next "Attaboy!"'. As for the future, the freedom allowed to me by John to expand my interests has given me the opportunity to work with Ned Wingreen, who has convinced me with his energy and encouragement that biology is not only the story of life but should be the story of my life as well, if ever it is written.

It is my great fortune in life that as I write more theses, the list of people to thank grows larger and larger. In as random an order as I can muster: Michelle Povinelli, Groucho, Harpo, and Chico, Diana Dorinson, Ronak Bhatt, Carmen and Mike Berg(om), Alexis Johnson and the rest of the Johnson family, John and Johanna Higgins, Michael Jordan, Jay Turner, Chris Arnesen and Jessica Halverson, Jessica Lages, Ikari Shinji, Emmi Snyder, Kevin Beach, Ghislain Granger, Marin Soljacic, Lefteris Lidorikis, Scott Todd, Tairan Wang, Peter Bienstman, Peter Bermel, Chiyan Luo, Niko Moll, Steven Johnson, David Chan, Aristos Karalis, Kyri Joannopoulos, Evan Reed, the Lamb, and the entire class of ABG2004.

Michelle, is this defense going to feel as good as finishing those triathlons? Chris, thanks for letting me beat you in 21 once in a while. Evan, thanks for that flight to Fitchburg that convinced me to spend $10K on a pilot's license. Tairan, thanks for having that gleam in your eye that reminds me physics is cool. Lefteris, thanks for coming to get me before going down to the bar at the W. Jay, thanks for mixin' it up and hating my choice of ringtones. Alexis and Somes, thanks for always letting me win at Wheel of Fortune. Ronak, thanks for getting me the best view of Boston. Ghislain, thanks for all playing along with all my "would you rather" scenarios.

... and now for the rest of you dekes. Toby, thanks for making lots of money to support me when I'm a grown-up physicist; Emma, thanks for wasting my life one SprintPCS minute at a time; Roger, thanks for 15 glorious hours of NGE; the Illustrious Pip Huangye, thanks for educating me about medical information that makes me glad I'm not a real doctor; Japa, thanks for 20 years of physics conversations; Grandpa and Grandma, thanks for caring about my education and future before I had the sense to; and Mom and Dad, thanks for letting me trash your house and empty your refrigerator every time I came home: Couldn't've done it without y'all. Get low, get low. Last, but definitely not least, to Molly and Yuki: Woof.

This thesis was paid for by DoD/ONR MURI Grant No. N00014-01-1-0803, the MRSEC program of the NSF under Award No. DMR-0213282, a Graduate Student Fellowship from the National Science Foundation, a Robert Stockbarger Fellowship from MIT, and by NEC Laboratories, America. Money well spent? You be the judge.

To the numbers 1 and 3, and the letters D and K...

Contents

List of Figures

List of Tables

Chapter 1

Introduction

Philip Anderson condensed condensed matter physics with the phrase "more is different". This comment is derived from the observation that as the size of a system grows, new levels of organization can arise, which often give a much simpler picture of the underlying physical properties that govern the system. At least in relation to the topics in this thesis, I would say instead "more is more interesting". By adding new components to or combining well-understood physical systems, the result is entirely new phenomena that are often suprising but more easily understood than the input components. I will investigate the various forms of electromagnetic radiation localization achieved in periodic dielectric structures when vibrational modes are introduced, the effect on the solid-liquid phase transition when the surface interface is interchanged, and the generation of spatiotemporal dynamic motion through combined reaction and diffusion of biomolecules.

For the most part, we have approached the problems in this thesis from an *ab initio* perspective. That is to say, only the minimal set of information such as the geometry and material composition is used to calculate the electromagnetic, electronic, or dynamic properties of the system. While the lack of assumptions relative to a more empirical approach adds to the computational complexity, the solution that results often provides a more fundamental description of the physics.

A large portion of problems in condensed matter rely on the interplay between theory and computation to provide insight into physical processes. The challenge,

therefore, is to choose a system size for the problem at hand which is at once tractable and informative. As technology has advanced rapidly in recent decades, it has become feasible - indeed necessary - to quickly balance our concept of what questions are answerable in a reasonable timeframe. A considerable part of this thesis has consisted of efforts to design and implement software that can efficiently provide answers and adapt to the ever-increasing availability of new computing resources.

The aforementioned research topics contained in this thesis are tied together more in spirit than in form. From polaritonic photonic crystals, to the electronic structure of melting, to biological pattern formation, the story of the development of structure is built from simple elements. In this introduction, I will describe the building blocks that have formed the foundation for this work. In Section 1.1, I discuss the properties of the polariton excitation - a coupled light and sound wave. These properties in the background of a periodic dielectric structure are the focus of Chapters 2-4. In Section 1.2, I discuss experiments that have motivated the study of changes in melting temperature due to modifications in the surface interface, leading to the *ab-initio* simulations in Chapter 5 at semiconductor interfaces that reveal superheating or induced melting. Finally, in Section 1.3, I discuss the experimental evidence for spatial oscillations in the Min protein system, which are modelled in different geometries in Chapters 6-8.

1.1 Optical phenomena in polaritonic photonic crystals

A photonic crystal is a periodic array of dielectric materials (see Fig. 1-1) [41]. In the same way that electrons are guided by scattering from the underlying atomic crystal, the flow of electromagnetic readiation can be controlled by a photonic crystal. For most technological applications of photonic crystals, the wavelength scale of interest is microns and higher. At this macroscopic length scale, it is the classical Maxwell's equations rather than quantum mechanics and quantum electrodynamics which hold

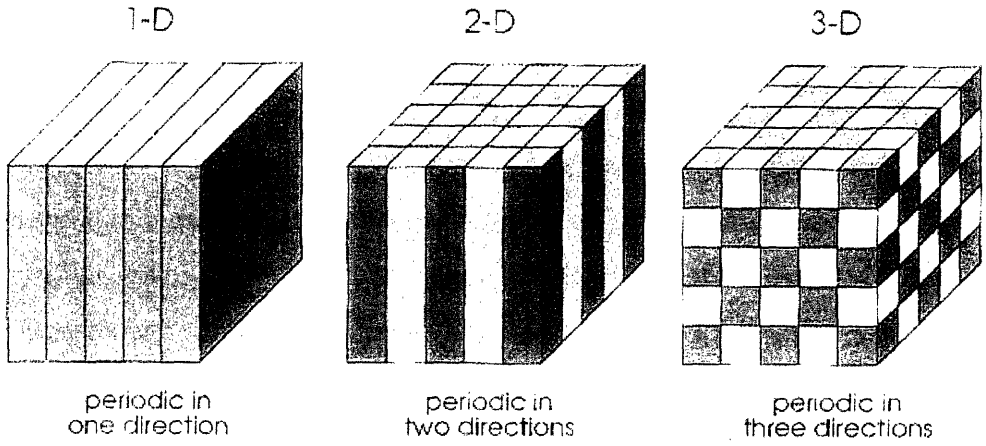

Figure 1-1: Periodic arrays of dielectric materials (photonic crystals) in one dimension, two dimensions, and three dimensions. The different colors represent materials with different dielectric functions. (originally published in Ref. [41])

sway.

An operator equation similar to the Schrödinger equation can be derived from Maxwell's equations. The solutions in an infinitely periodic system are Bloch waves, and the dispersion can be described by a band structure of the form $\omega_n(k)$ [41]. The band structure can exhibit, for suitable choices of geometry and materials, a photonic band gap in which the propagation of light is forbidden [97, 42]. The search for systems with a complete band gap across all wave vectors has been a subject of intensive research. By creating defects inside the photonic crystal, it is possible to achieve a wide array of remarkable optical phenomena, including waveguide and cavity localization [43, 23, 21].

The atomic character of the materials can also be important for introducing frequency dispersion into the dielectric function. In particular, some polar materials have transverse-optical phonon modes that couple strongly to electromagnetic radiation to produce polariton excitations [3]. This interaction results in a band gap (the *polariton gap*) above the phonon resonance, even in a bulk system without periodicity, where light is forbidden to propagate [46].

The polaritonic dielectric function essentially splits into two primary frequency

regimes of interest. Below the phonon resonance, the index of refraction is large and grows with increasing frequency, which tends to concentrate light into the material. Directly above the phonon resonance, the dielectric function is large and negative, so the material has a strong metallic character and will reflect light. A key feature of two-dimensional (and higher-dimensional) photonic crystals is the existence of propagating states even when one of the materials is metallic. It is these high-index and metallic regimes within which much of our analysis will focus in *polaritonic photonic crystals*, which are formed when at least one of the dielectric materials in a photonic crystal is replaced by a polaritonic medium.

In a polaritonic photonic crystal, the interplay between the polariton gap and the photonic band gap of the periodic crystal creates new optical phenomena which are the focus of Chapters 2-4. In Chapter 2, we analyze the key features of one- and two-dimensional crystals for a variety of materials and lattice sizes. The Bloch states exhibit new localization phenomena stemming from both the high index contrast and the dispersion of the polaritonic dielectric function. In two dimensions, intraband transitions below the phonon resonancec result in continuous shifts in the nodal pattern of the light, which is localized inside the polariton material. Interband transitions across the phonon resonance result in wholesale flux expulstion into the air region due to the metallicity of the polariton gap.

To compare our theoretical predictions with potential experiments designed to observe these phenomena, we focus on the band structure and field-localization effects in a two-dimensional crystal composed of a common polaritonic medium, lithium tantalate ($LiTaO_3$) [14]. This material has a very large index of refraction at both low and high frequencies - an important criterion for achieving the node switching and flux expulsion localization phenomena. However, lithium tantalate also has non-negligible losses around the phonon frequency due to absorption [78]. These losses are manifested in the band structure by an imaginary wave vector or frequency component in each Bloch state.

In Chapter 3, we ask how strongly losses affect the dispersion relation and the field localization effects inside a polaritonic photonic crystal. We approach the more

general problem of calculating the band structure of a photonic crystal composed of lossy materials by utilizing two different computational approaches. The time-domain approach uses a periodic excitation that consequently has real wave vector, while the frequency-domain approach uses a constant-frequency plane-wave input. Although the distinction between these methods is purely cosmetic for lossless systems, we demonstrate that the band structures generated by these two methods can be very different, especially in systems with strong localization properties. We reconcile these differences and provide analytic criteria for instances in which the time-domain and frequency-domain band structures do overlap. We also demonstrate specifically in Chapter 3 that losses in the $LiTaO_3$ polaritonic photonic crystal in Chapter 2 do not prevent observation of the node-switching and flux-expulsion behaviors.

Although absorption losses are obviously detrimental to the propagation of light, recent theoretical [95, 67] and experimental studies [66, 86, 88, 79] have shown that a lossy photonic crystal structure can behave as an effective bulk medium with novel properties. These so-called metamaterials can exhibit negative effective permittivity [67] and/or permeability [63] - properties which have not been observed in bulk materials. The result when both are negative is several reversed electromagnetic-wave properties including negative refraction [79]. In Chapter 4, we demonstrate that negative effective permeability can be achieved in the photonic band gaps of a two-dimensional polaritonic photonic crystal slab, and that the wavelength interval over which this occurs increases with increasing dissipation. We discuss the origin of this effect and show that the potential operating wavelength range can extend from two to hundreds of microns through the use of different polaritonic materials.

1.2 Molecular dynamics of melting in semiconductors

Melting is the transition from a solid to a liquid phase. It is a typical example of a common physical phenomenon that is at once easy to identify, and difficult to under-

stand [94, 7, 13, 12, 8, 9]. Theoretical investigations of the causes and properties of the melting transition have, to a large degree, followed one of two paths investigating: (*i*) the thermodynamic stability of the free energy of the liquid phase relative to the solid phase, or (*ii*) instabilities in the solid that initiate the transition. The second path is particularly intriguing from an *ab initio* point of view because it infers a macroscopic change of state from microscopic defects within the solid. Comprehensive reviews of the effects of melting on crystal structure can be found in Refs. [93, 94, 7].

Superheating, or preserving of the solid phase above the normal melting temperature T_m, is at most possible for many materials only in a very small interval about this point. This seems to indicate an inherent stability limit of the solid which is overcome at T_m in the transition to a liquid phase. As early as 1910, Lindemann proposed a simple criterion for the melting instability correlating T_m with a critical value of the ratio of the vibrational amplitude to the spacing between atoms [94]. The idea that melting can be predicted from the motion of the constituent atoms has led to many theoretical studies using molecular dynamics [90, 69, 68].

Previous work has focused on the initiation of melting from defects in the solid such as point defects, line defects, and grain boundaries. Phillpot *et al.* [69] have analyzed the propagation of the solid-liquid interface generated from a grain boundary or a free surface in a silicon crystal using interatomic potentials. Takeuchi *et al.* [92] studied melting at the (111) surface of a germanium crystal and found that on the picosecond time scale, the first few layers of the surface will melt while the bulk remains solid (surface melting). An understanding of the role of surfaces in the melting process is crucial since every experimental sample has a free surface and it is very difficult to controllably initiate and study melting from inside the bulk rather than at the surface.

Perhaps the fact that melting starts at the surface can be used advantageously. There are many examples of materials that differ greatly in melting temperature, but have similar lattice constants and so can form strong interfaces. For instance, silver and gold differ by only a single row in the periodic table, yet T_m differs by 103 K (T_m(Ag)= 1235 K, T_m(Au)= 1338 K [46]). Experiments by Daeges *et al.* [15]

demonstrated that a silver sphere with a thin ($\sim 10-20\mu$m) coating of gold achieved superheating of 25 K for one minute (see Fig. 1-2). These experiments followed similar examples of superheating behavior in quartz/cristobalite crystals surrounded by fused silica [1] and argon bubbles in aluminum [76].

The idea of changing the free surface, thereby altering the melting behavior, using a *macroscopic* coating in the same fashion as the experiments listed above has yet to be explored theoretically due to computational intractability. Whether or not the superheating phenomenon can be observed using only a microscopic coating (on the order of a single atomic layer in thickness) has not been previously studied either experimentally (due to difficulty of fabrication) or theoretically. However, this is a problem ideally suited to molecular dynamics approaches. In terms of the choice of interface, a textbook example of similar materials with contrasting melting points in condensed matter physics along the same line of thought as the Au/Ag example is the semiconductors germanium and gallium arsenide. Despite having nearly identical lattice constants and average masses, T_m differs by over 300 K (T_m(Ge)= 1211 K, T_m(GaAs)= 1540 K) [46].

In Chapter 5, we study the (110) surfaces of Ge and GaAs, the natural cleavage plane of both materials, with and without single-layer coatings of GaAs and Ge, respectively. We utilize density functional theory to minimize the total electronic free energy at each time step, replacing the many-electron Schrödinger equation with an equivalent set of self-consistent single-electron equations [27, 47, 65]. One component of these equations is an unknown exchange-correlation energy functional that is often approximated using the local density approximation. The evolution of the ionic coordinates is computed from the interatomic forces using the Verlet algorithm, while the temperature is fixed using a Nose thermostat. This *ab-initio* approach not only generates the dynamic motion of the ions, but by treating the electrons quantum mechanically also provides band structure and charge density information that can be used to reveal the electronic signals of melting at a fundamental level.

Our simulations were performed at an intermediate temperature of 1240 K - in between the melting points of Ge and GaAs. The effects of the minimal-thickness

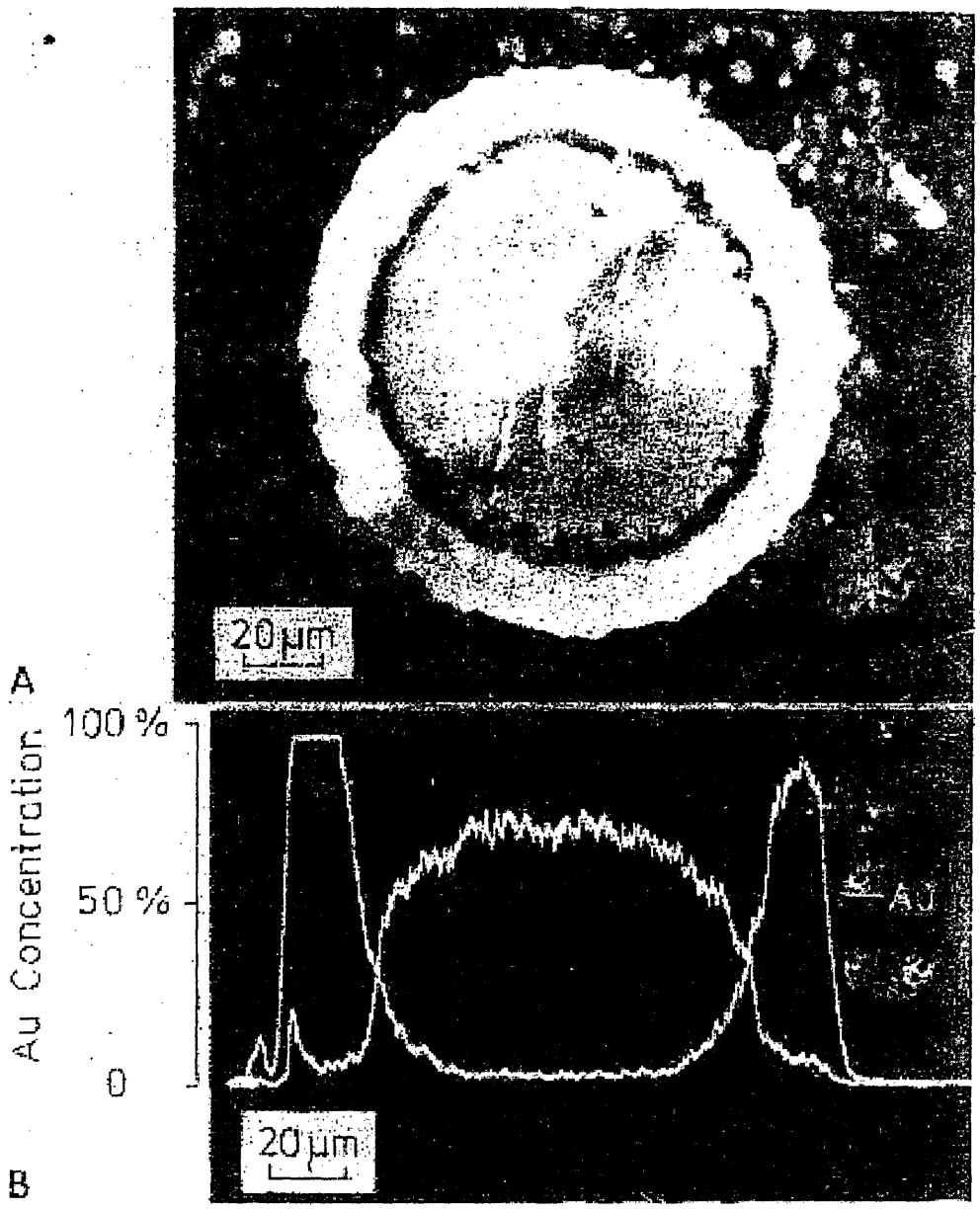

Figure 1-2: Superheating of a silver crystal using a gold coating: (a) The Ag crystal remains stable at a temperature 25 K above its melting point when coated with Au. (b) The composition of Ag and Au in a radial slice indicates the stability of the Ag core. (originally pulished in Ref. [15])

single-layer coatings are stunning. The rapid diffusive motion of the atoms on the Ge surface are significantly slowed by the presence of the GaAs layer. Furthermore, the layers of Ge atoms deeper in the bulk (which are completely melted without the coating) remain solid for the duration of our run, even at a temperature 30 K above the melting point of Ge. Despite the minimal thickness of the coating, the stabilizing influence of the GaAs is apparent. The Ge-coated GaAs system displays the opposite behavior. A bare GaAs surface is incredibly stable at 1240 K, but the single-layer coating of Ge contains mobile atoms that penetrate into the surface, inducing melting in the GaAs layer below despite being 300 K below the melting point of GaAs.

1.3 Spatial oscillations of proteins in bacteria

Until recently, the central dogma of reaction-kinetics in bacteria featured the cell as a well-stirred reactor. That is, without the organelles which are present in cells of higher organisms to localize products of cell function, a combination of diffusion and high copy numbers of proteins can keep concentrations inside the cytoplasm homogeneous. However, it was necessary to revisit and alter this picture of protein concentration and (de)localization after the discovery of dynamic structures which form in spatiotemporal oscillations of the Min-protein system in *Escherichia coli* [16, 74, 32, 24].

E. coli is a rod-shaped bacterium, 2 to 4 microns in length, which divides approximately every 40 minutes near the mid-point of the cell with a high degree of precision (see Fig. 1-3). The source of this precision is at least partially due to the Min proteins: MinC, MinD, and MinE. A min^- mutant which lacks the ability to produce the Min proteins not only divides at more haphazardly-chosen locations around the mid-point, but also divides asymmetrically near the poles, creating small, round minicells [16]. These cells lack a chromosome and hence are nonviable.

The process by which the Min proteins regulate the selection of the division site was revealed by tagging the Min proteins with the jellyfish protein, Green Fluorescence Protein (GFP) [74, 32, 24]. This made it possible to image the positions of

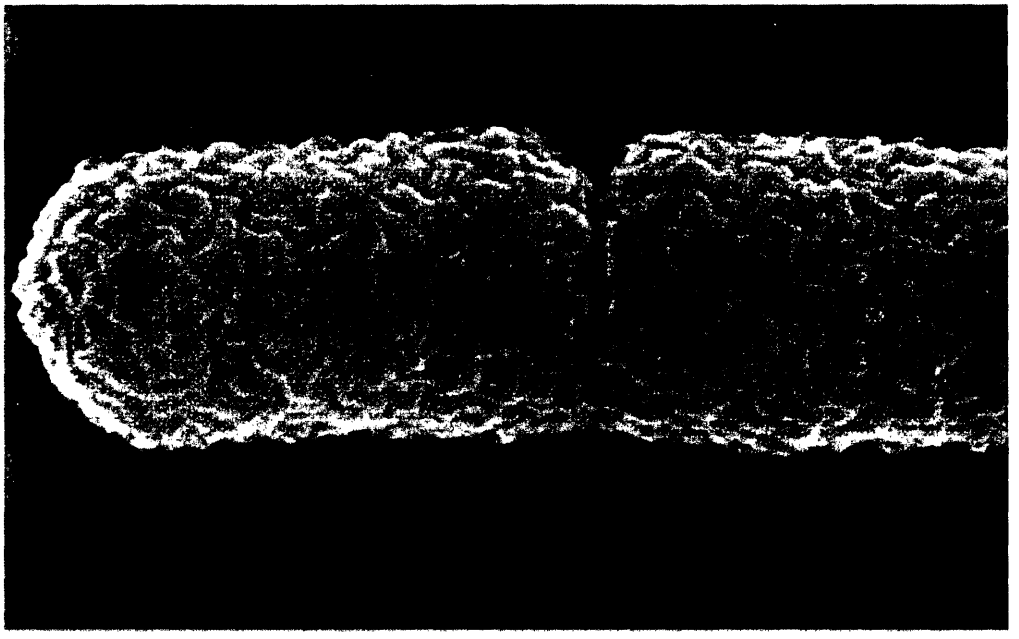

Figure 1-3: An *Escherichia coli* cell in the process of division.

the tagged molecules inside the cell using fluorescence microscopy. The surprising discovery was made that all three of the Min proteins move from pole-to-pole in a persistent oscillatory pattern [74, 26].

By disabling the production of one or some combination of the Min proteins, genetic experiments have pinpointed the roles of each protein in driving the oscillations and ultimately in division site selection. In isolation, MinC results in filamentous growth when the concentration is highly overexpressed [17]. This division inhibition is caused by MinC blocking the polymerization of the FtsZ protein [4], a necessary step in the machinery for dividing the cell membrane [5]. At wild-type (normal) levels, both MinC and MinE are cytoplasmic, except in the presence of MinD and ATP [34, 31]. MinD binds ATP and goes to the membrane, where it recruits MinC and MinE [31].

In vivo observations of the spatial oscillations of MinD and MinE are shown in Fig. 1-4 [26]. In each oscillation period, the MinD population forms a polar zone of accumulation on the membrane at one pole of the cell. It then shrinks back toward the pole and reforms at the opposite end. Experiments with simultaneously-tagged

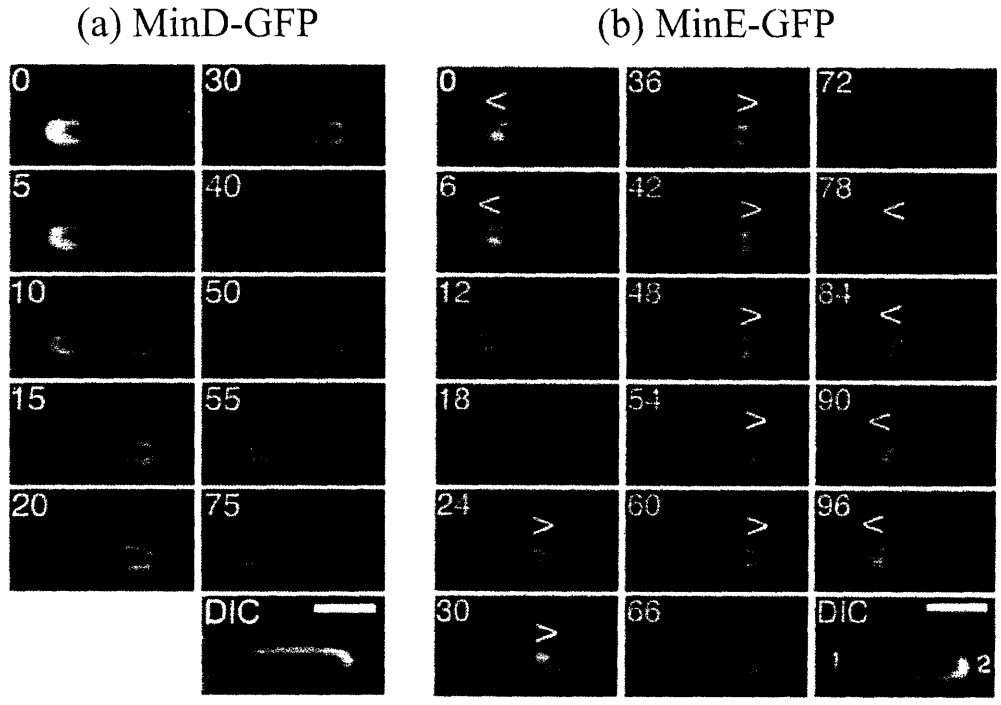

Figure 1-4: (a) The MinD-GFP is primarily membrane-bound, forming a polar zone which oscillates between the left and right poles. The MinD-GFP concentration is always low near the center of the cell. (b) MinE forms a membrane-bound "ring" which appears near the cell center and moves toward the pole. (originally published in Ref. [26])

MinD-GFP and MinE-GFP have shown that MinE oscillates with the same period as MinD [101]. The MinE accumulates as a membrane-bound "ring" which reforms near the center of cell and moves toward the pole at the medial edge of the MinD polar zone. MinC forms complexes with MinD, but the primary role of MinC is as a division inhibitor. The oscillations require both MinD and MinE, but not MinC [74].

The biochemical function of the oscillations is clear: the MinC/D concentration is always much higher at the ends of the cell than in the center (cf. Fig. 1-4(a)), establishing a preference for the center of the cell as the division site and eliminating minicelling. This can also be viewed physically as a fascinating occurence of pattern formation. Filamentous cells with lengths ranging to upwards of 40 microns can be grown by knocking out production of FtsZ. These mutants have a "zebra-stripe" pattern of oscillations. In the 10-micron cell in Fig. 1-5(a) [26], the MinE-GFP

(a) MinE-GFP (b) MinD-GFP

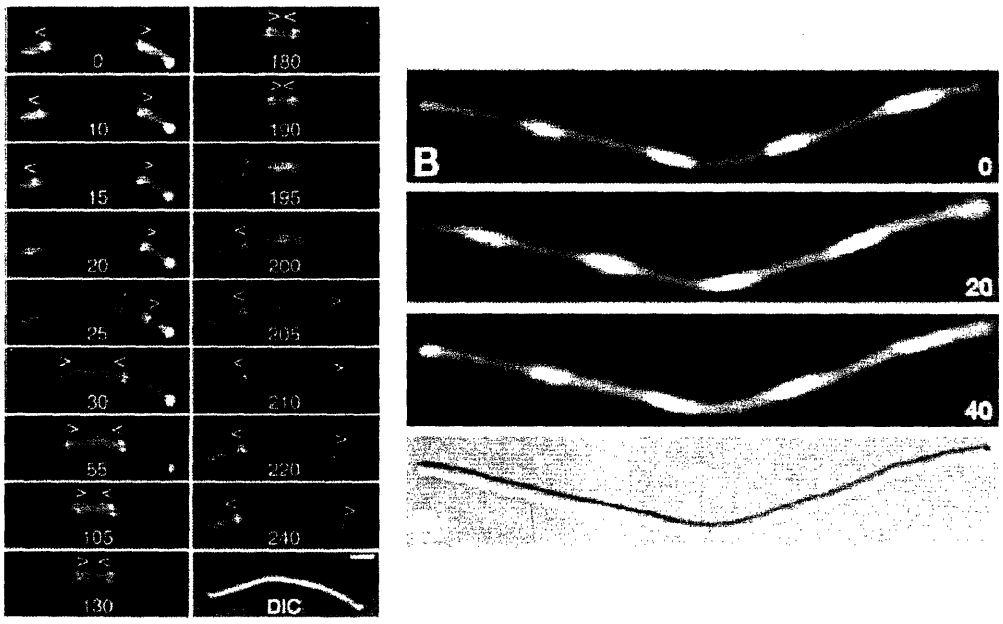

Figure 1-5: (a) 10-micron cell: MinE-GFP forms a doubled pattern with two rings that move in separate halves of the cell 180 degrees out-of-phase in oscillations similar to Fig. 1-4(b). (b) 40-micron cell: MinD-GFP establishes a regular oscillatory pattern with a wavelength of around 10 microns. (originally published in Refs. [26] and [74])

simultaneously accumulates in two rings which move either toward opposite poles or inward toward the cell center. In Fig. 1-5(b) [74], the distribution of MinD-GFP in a 40-micron cell has a distinct wave-like pattern with a characteristic wavelength of around 10 microns.

Given the wealth of biochemical information regarding the Min proteins, we would like to find a minimal theoretical model that contains only known interactions. In Chapter 6, we introduce a system of reaction-diffusion equations which successfully reproduce the observed behavior in wild-type cells and in filaments, as well as MinE fragment mutants which have smeared protein concentrations and much slower oscillation periods. One crucial difference between our model and previous attempts to study the Min system is the requirement of a finite nucleotide exchange time of around one second. This is the time required for a freshly hydrolyzed MinD:ADP complex

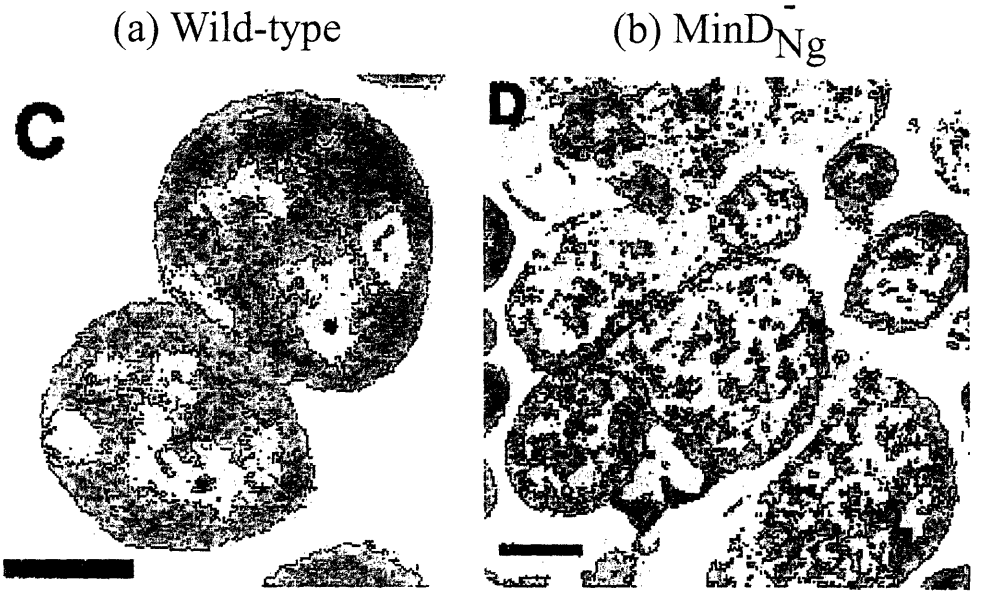

Figure 1-6: (a) In wild-type *N. gonorrhoeae*, cell division results in round, equally-sized daughter cells. (b) Mutants without the MinD_{Ng} protein divide abnormally into different shapes and sizes. (originally published in Ref. [91])

coming off the membrane to rebind to a new ATP molecule and become competent for rebinding. The nucleotide exchange process is crucial to our understanding of the origin of the length scale as a molecular clock that allows the instability to shift from one pole to the other and establishes the oscillatory pattern in filaments. Recent experiments have shown that the nucleotide exchange rate is around two events per second - remarkably close to our prediction considering such rates can vary over five orders of magnitude [55].

Many other bacteria, such as *Bacillus subtilis* and *Neisseria gonorrhoeae*, possess homologs of the Min proteins. The loss of the MinD_{Ng} protein in round *N. gonorrhoeae* results in abnormal cell division with asymmetric daughter cells (see Fig. 1-6) [91, 71]. In Chapter 7, we apply our numerical model for rod-shaped cells to spherical cells and find that Min oscillations occur. The oscillatory pattern is slightly different, with no signature of a MinE ring. In Chapter 7, we discuss our finding that this is a natural consequence of the round geometry of the cell. The other key question in a cell with a

high degree of symmetry is: How does the cell choose an axis of oscillation? We find that in ellipsoidal cells, the oscillations spontaneously orient along the long axis of the cell due to a preferred wavelength of instability that is greater than the dimensions of the cell. Remarkably, these results indicate that protein oscillators may form a general mechanism by which the cell detects and exploits its own geometry, in this case for targeting proteins to the poles. In Chapter 8, we derive analytically how a preferred length scale arises from any simple reaction-diffusion system and apply these results to the mean-field model of Chapters 6 and 7.

Chapter 2

Phonon-Polariton Excitations in Photonic Crystals

Segments of this chapter have previously appeared in: Huang, Bienstman, Joannopoulos, Nelson and Fan, Phys. Rev. B ***68*** *075209 (2003) and Huang, Bienstman, Joannopoulos, Nelson, and Fan,* Phys. Rev. Lett. ***90*** *196402 (2003).*

In recent years, the study of polar media which permit transverse phonon polariton excitations has commanded great attention both experimentally [14] and theoretically [3] due to the unique and well understood frequency-dependent dielectric function. In bulk polaritonic materials, there is a frequency range (the *polariton gap*) in which the propagation of electromagnetic (EM) waves is prohibited. Such a frequency range is generally called a photonic bandgap (see Fig. 2-1). This photonic bandgap (PBG) is unrelated to translational symmetry, unlike the PBG properties of crystals of constant dielectric materials, known as photonic crystals. Since the groundbreaking work of Yablanovitch [97] and John [42], the explosion of research into the design and fabrication of photonic crystals with complete PBGs [41] has inspired a wealth of potential telecommunications applications, including waveguides, channel drop filters, and omnidirectional reflectors [43, 23, 21]. We will demonstrate how the substitution of polaritonic materials into photonic crystals introduces a whole range of exciting new physical phenomena.

At a resonance between a transverse optical phonon at frequency ω_T and a trans-

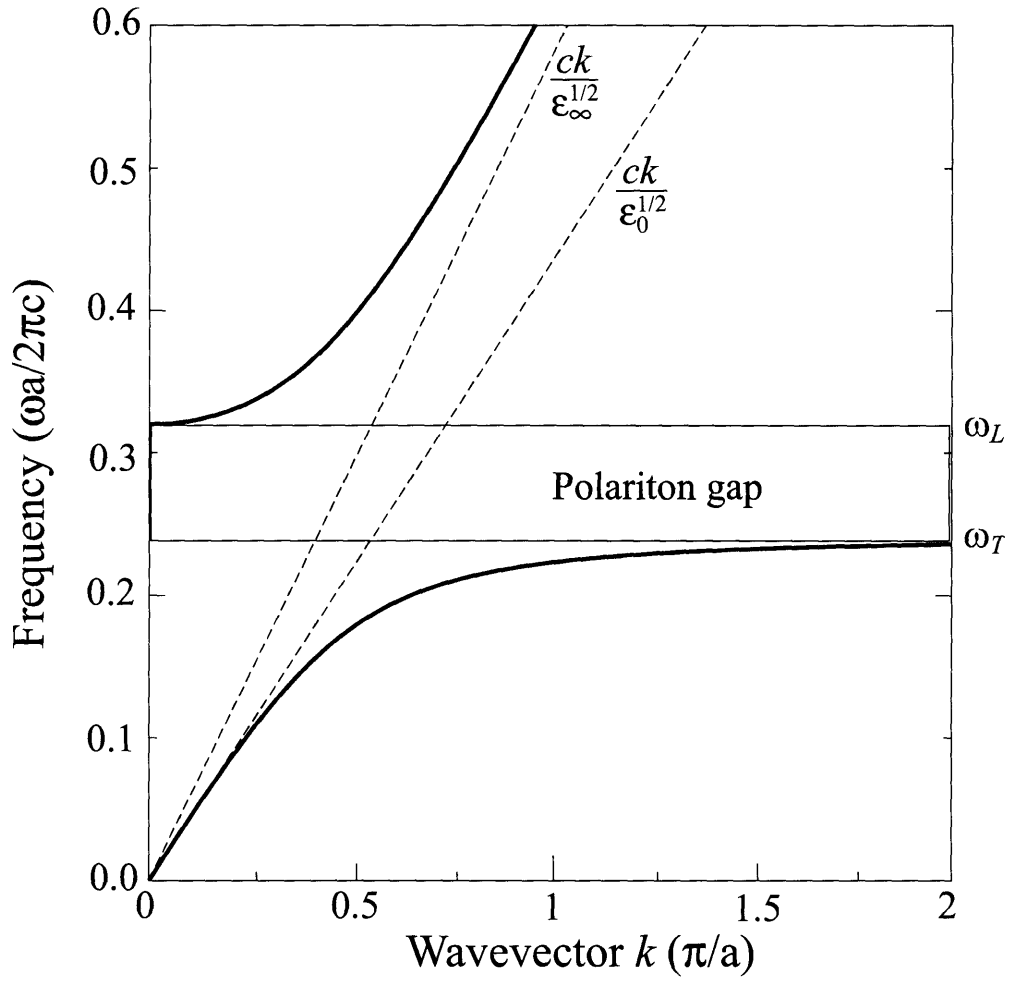

Figure 2-1: Dispersion relation for a material with polariton dielectric function given by equation (2.1).

verse EM wave, the phonon-photon coupling induces a radical change in the material's optical response. At low wavevectors, a simple model with dispersionless phonons yields the dielectric function [46]

$$\varepsilon(\omega) = \varepsilon_\infty \left(\frac{\omega^2 - \omega_L^2}{\omega^2 - \omega_T^2} \right), \tag{2.1}$$

where ε_∞ is the dielectric response at high frequency, and ω_L is related to ε_∞ and ω_T through the well-known Lyddane-Sachs-Teller relation $\omega_T \sqrt{\varepsilon(0)/\varepsilon_\infty}$. Clearly, the power of polaritonic materials lies in the opportunity to study the large epsilon and negative epsilon regimes using the same physical structure by merely choosing the frequency of light below ω_T or inside the polariton gap between ω_T and ω_L.

Various aspects of photonic band gaps and band structures of polaritonic photonic crystals (PPCs) have been previously studied using a diverse set of theoretical tools [83, 84, 100, 51, 85, 20]. Work by Sigalas *et al.* [83, 84] focused on determining the photonic bandgaps in a two-dimensional photonic crystal slab composed of polar materials by analyzing the transmission coefficient as a function of frequency using the transfer matrix method. To our knowledge, the first 2D PPC band structures were calculated by Zhang *et al.* [100] and followed by Kuzmiak, Maradudin and McGurn [51]. In both works, the authors identify as the major development the presence of flat, almost dispersionless bands below the phonon frequency ω_T.

Kuzmiak *et al.* postulate an explanation for these bands as coupling to the localized cavity modes of an isolated rod. We show that this proposition is indeed correct, by providing a fundamental model applicable in 1D, 2D, or 3D for photonic crystal properties in the large ε regime that quantitatively explains the locations of the PPC bands below ω_T. In doing so, we demonstrate how the coupling can occur in totally different manners for the TE and TM modes depending on the location of ω_T relative to the bands of a metallodielectric crystal, with the polaritonic material replaced by a perfect metal. In some cases, the crystal will manifest an anticrossing behavior of the TE bands (**H** out of plane) that has not been previously observed (due to the choice for $\omega_T a/2\pi c$, where a is the PPC lattice spacing, of either 0.5 or 1.0 in the two

other works [100, 51]).

In addition, we provide a description of the bands directly above ω_T, a metallic regime that has not been previously investigated. The presence of TE and/or TM bands which converge to ω_T is again regulated by the positon of ω_T relative to the bands of the metallodielectric crystal. The situations when bands exist arbitrarily close to ω_T both above and below lead to the introduction of a unique *flux expulsion* phenomenon, where light can be transferred completely in and out of the polaritonic material into the interstitial photonic crystal medium as ω sweeps across ω_T in an extremely small interval.

The paucity of previous PPC calculations is perhaps due to computational obstacles in traditional time-domain and plane-wave method (PWM) codes that crop up near the poles and zeroes of ε at ω_T and ω_L, respectively. However, it is precisely these frequency ranges, where the materials divert from normal optical behavior, which we have found to be of particular interest. To overcome these difficulties, we employ a technique based on vectorial eigenmode expansion, discussed in section 2.1, which is ideally suited for frequency-dependent dielectrics and is accurate over an extremely large range of ε.

In section 2.2, we provide a comprehensive description of the band structures of 1D PPCs. We introduce our model for the flat bands below ω_T, and demonstrate the excellent agreement with our numerical results. We also characterize the bands inside the polariton gap at Γ, and demonstrate that for certain values of ω_T, ω_L, and ε_∞, there can be a characteristic frequency where the entire crystal becomes transparent. In addition, the simplicity of the 1D crystal allows us to provide an analytic solution for the wavevector of the bands at ω_L where $\varepsilon(\omega)$ goes to zero.

In section 2.3, we adapt our model of the flat bands below ω_T to a 2D square lattice of polaritonic rods, and demonstrate the difference in behavior between TE and TM polarizations. The metallic bands directly above ω_T appear, and we explain how the band structure in these two regions can be simply tuned by varying ω_T, in particular to exhibit flux expulsion.

In section 2.3.5, we extend our results to a two-dimensional photonic crystal com-

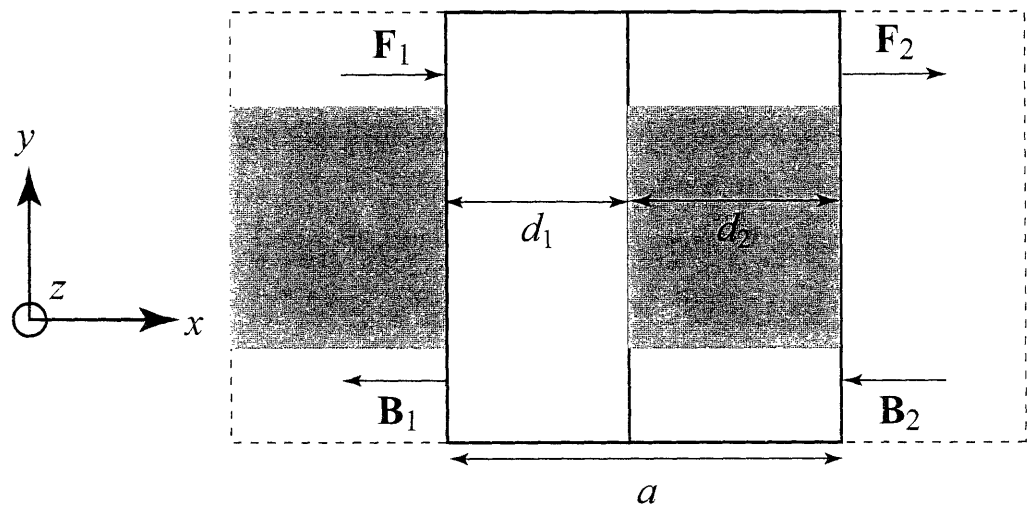

Figure 2-2: Unit cell in a periodic structure marked by solid outline. Note the axis convention which will be adhered to henceforth.

posed of a polaritonic material, $LiTaO_3$, which is commonly used experimentally due to its large polariton gap. Finally, in section 2.4 we discuss the effects of losses in the polaritonic material.

2.1 Computational Method

To calculate the Bloch modes of a structure consisting of frequency-dependent materials, we use an approach based on vectorial eigenmode expansion [6]. We identify a unit cell in the crystal oriented along a certain propagation direction (see Fig. 2-2), and subsequently divide this cell in layers where the index-profile does not change in the propagation direction. In each of these layers, we expand the field in the local eigenmodes of that particular layer. The only approximation is the size of the eigenmode basis.

Using mode matching, we can eventually derive reflection and transmission matrices that completely describe the scattering behavior of the unit cell:

$$\mathbf{F}_2 = \mathbf{T}_{12} \cdot \mathbf{F}_1 + \mathbf{R}_{21} \cdot \mathbf{B}_2 \tag{2.2}$$

$$\mathbf{B}_1 = \mathbf{R}_{12} \cdot \mathbf{F}_1 + \mathbf{T}_{21} \cdot \mathbf{B}_2 \tag{2.3}$$

Here, $\mathbf{F}$ and $\mathbf{B}$ are column vectors containing the expansion coefficients of the forward and backward propagating fields, respectively, and $\mathbf{T}_{12}$, $\mathbf{R}_{21}$, etc. are explicit functions of frequency. We then impose Bloch boundary conditions:

$$\mathbf{F}_2 = e^{-ika}\mathbf{F}_1 \tag{2.4}$$

$$\mathbf{B}_2 = e^{-ika}\mathbf{B}_1 \tag{2.5}$$

Equations 2.2 and 2.4 can be recast as a generalized eigenvalue problem, which can be solved for each frequency, where $\mathbf{I}$ is the unit matrix and $q = e^{-ika}$:

$$\begin{bmatrix} \mathbf{T}_{12} & \mathbf{R}_{21} \\ 0 & \mathbf{I} \end{bmatrix} \begin{bmatrix} \mathbf{F}_1 \\ q\mathbf{B}_1 \end{bmatrix} = q \begin{bmatrix} \mathbf{I} & 0 \\ \mathbf{R}_{12} & \mathbf{T}_{21} \end{bmatrix} \begin{bmatrix} \mathbf{F}_1 \\ q\mathbf{B}_1 \end{bmatrix}$$

In contrast to other approaches which compute the eigenvectors of the transfer matrix [57, 62], no matrix inversions are required in our approach and therefore the method is numerically more stable. We also want to point out that in 1D, this method is equivalent to the well-known transfer matrix method (TMM).

Since the independent variable in these calculations is frequency rather than wave vector, it is trivial to account for material dispersion. Moreover, it is possible to increase the frequency resolution locally, an advantage over time domain simulations where a frequency grid of increased resolution is implemented through a global increase in the number of time steps. This flexibility is exceedingly important for polaritonic materials, since there are rapid changes in the dielectric function over very small frequency intervals near ω_T.

These techniques were implemented in our generic photonic simulation tool CAMFR, which is freely available from http://camfr.sourceforge.net.

A further restriction on time-domain and PWM calculations involving frequency-dependent dielectric functions is the necessity for a self-consistency loop when solving

for the bands. In addition to the increased computational time, we have found the self-consistency step to introduce serious numerical instabilities in certain ranges, particularly where ε is very small. Kuzmiak *et al.* [52] also mention the danger of missing zeroes in the determinant of the matrix of expansion coefficients in the plane wave expansion if the increment in frequency is too small. For the specific case of a polariton dielectric function, it is possible to recast the solutions to Maxwell's equations as a generalized eigenvalue equation using the plane wave method to avoid the self-consistency loop [51], but for general frequency-dependent dielectric functions this simplification is impossible.

2.2 1D Polaritonic Photonic Crystal

We first examine the band structure of a 1D photonic crystal with propagation in the $\hat{\mathbf{x}}$ direction. The modes are TEM in this case, with both $\mathbf{E}$ and $\mathbf{H}$ parallel to the interface. For definiteness, we consider the polariton material CsI, with $\omega_T = 12 \times 10^{12}\text{rad}/s$, $\omega_L = 16 \times 10^{12}\text{rad}/s$, and $\varepsilon_\infty = 3.0$ [46]. With a lattice constant of $a = 6\mu\text{m}$, the polariton gap occurs between the normalized frequencies $\omega_T = 0.24$ and $\omega_L = 0.32$ (in units of $2\pi c/a$). For the most part, we will use air as the ambient material between polaritonic layers ($\varepsilon_{\text{ambient}} = 1$). The dielectric function and band structure are shown in Fig. 2-3.

There are three interesting features of Fig. 2-3(b) that are immediately apparent: (i) the flat bands below ω_T, (ii) the modes existing inside the polariton gap below ω_L, and (iii) the portion of the band around the frequency $\omega = 0.3533$ where $\varepsilon = 1$ and the band intersects the line $\omega = ck$. One important question is whether our choice of polariton parameters $\{\omega_T, \omega_L, \varepsilon_\infty\}$ holds any importance. In 1D, the location of the polariton gap has little effect, but a different picture will emerge in 2D.

We will study (i) by examining the modes of photonic crystals in the large index contrast limit. Our understanding of (ii) will come from an analytic solution of the wavevector at ω_L given by the TMM, and (iii) is a simple by-product of the transparency of the crystal at a particular frequency.

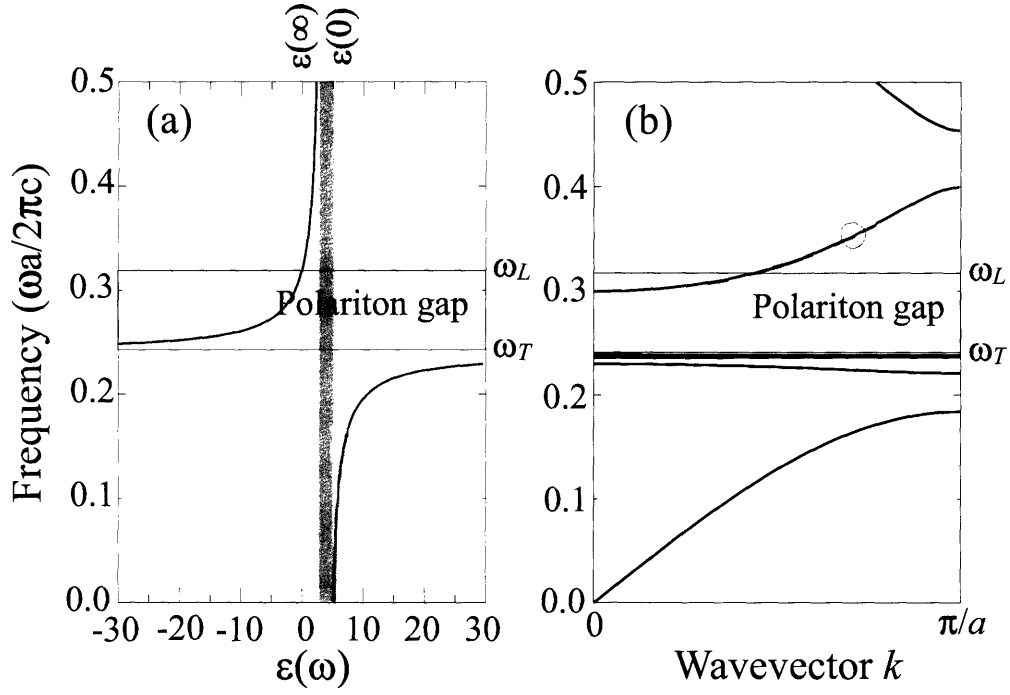

Figure 2-3: (a) Polariton dielectric function of CsI with $\omega_T = 0.24$, $\omega_L = 0.32$, and $\varepsilon_\infty = 3.0$. (b) Band structure of a 1D photonic crystal composed of CsI and air, with $d_1 = a/2$. Note the flat bands below ω_T, the penetration of the phonon-like part of the band near ω_L into the polariton gap, and the transparency point (represented by the open circle) where $\varepsilon = 1$ and the band intersects the line $\omega = ck$.

2.2.1 Large n Slab Modes

As previously mentioned, other authors [100, 51] have observed the flat band phenomenon in PPCs below ω_T. However, what is missing is a theory to describe both qualitatively why the dispersion is so small, and quantitatively where these bands occur. We will provide an answer to both of these issues in detail for a 1D PPC with a mind toward facilitating our future discussion in 2D. Directly below ω_T, the polariton material has a large index of refraction, and so in order to understand the flat bands in this frequency range, we initially ignore the frequency dependence of the material and consider a slab with fixed, large n. As $n \to \infty$, the reflectivity normal to an air interface may be shown to behave as

$$R = \left|\frac{n-1}{n+1}\right|^2 \to 1.$$

Hence, there are localized modes within the dielectric of the form

$$\varphi_m = \sin(\omega_m x), \text{ with frequencies } \omega_m = \frac{m\pi c}{nd}.$$

We note that these are of course only true localized modes in the limit $n \to \infty$; for finite n, the leakage of the fields into the air region allows for coupling between adjacent slabs and introduces frequency dispersion.

If we now assume a frequency-dependent dielectric function, the slab resonances also become frequency-dependent. We can solve the equation $\hat{\omega}_m = \omega_m(\hat{\omega}_m) = m\pi c/d\sqrt{\varepsilon(\hat{\omega}_m)}$ to obtain

$$\hat{\omega}_m^2 = \frac{1}{2}\left(\omega_L^2 + \Omega_m^2 - \sqrt{(\omega_L^2 + \Omega_m^2)^2 - 4\Omega_m^2\omega_T^2}\right), \tag{2.6}$$

where $\Omega_m = m\pi c/d\sqrt{\varepsilon_\infty}$.

In the limit of extremely localized fields, we expect the bands of the 1D polaritonic photonic crystal to follow a simple tight-binding model with a Hamiltonian

$$H\varphi_m = \hat{\omega}_m\varphi_m + T(\varphi_{m+1} + \varphi_{m-1}),$$

m	$\omega(\pi/2a)$	$\hat{\omega}_m$	$\varepsilon(\hat{\omega}_m)$
2	0.2362	0.235900	71.88
3	0.238256	0.238194	158.6
4	0.239008	0.238988	280.1
5	0.239361	0.239353	436.4
6	0.239555	0.239551	627.3
7	0.239672	0.239670	853.0
8	0.239749	0.239748	1113
9	0.239801	0.239801	1408
10	0.239839	0.239839	1738
11	0.239867	0.239867	2103

Table 2.1: Comparison of the band frequencies at $k = \pi/2a$ to $\hat{\omega}_m$ from equation 2.6 for a 1D crystal of CsI in air with $d_1 = d_2 = a/2$. In the last column is the value of ε at $\omega = \hat{\omega}_m$.

and bands of the form $\omega(k) = \hat{\omega}_m + T\cos(ka/\pi)$. The Hamiltonian has been linearized to obtain eigenvalues ω rather than the standard ω^2 by expanding in the small nearest-neighbor coupling integral T. Similar tight-binding models of photonic crystals have shown excellent agreement when the dielectric material has large ε [54].

In table 2.1, we compare the frequencies at $k = \pi/2a$ to $\hat{\omega}_m$ and find excellent agreement, to within 0.1% for all $m > 1$. This clearly indicates that the localized mode model works beautifully and allows for the precise determination of not only the location of every band below ω_T but also, as we will examine more closely in 2D, the shape of the highly localized fields inside the polariton material.

2.2.2 Defect-Like States in the Polariton Gap

We now turn our attention to the other side of the polariton gap. In Fig. 2-3(b), we see that in the range $\omega \in [0.2997, \omega_L]$ there are states inside the polariton gap, where $\varepsilon(\omega) < 0$. There is a simple interpretation of these modes. In the crystal, the slabs of air can be treated like defects in an otherwise homogeneous polariton material, drawing the states near $k = 0$ around ω_L down into the gap. This is the opposite of the normal effect of air defects in a photonic crystal; the air becomes the higher index material when ω is near ω_L.

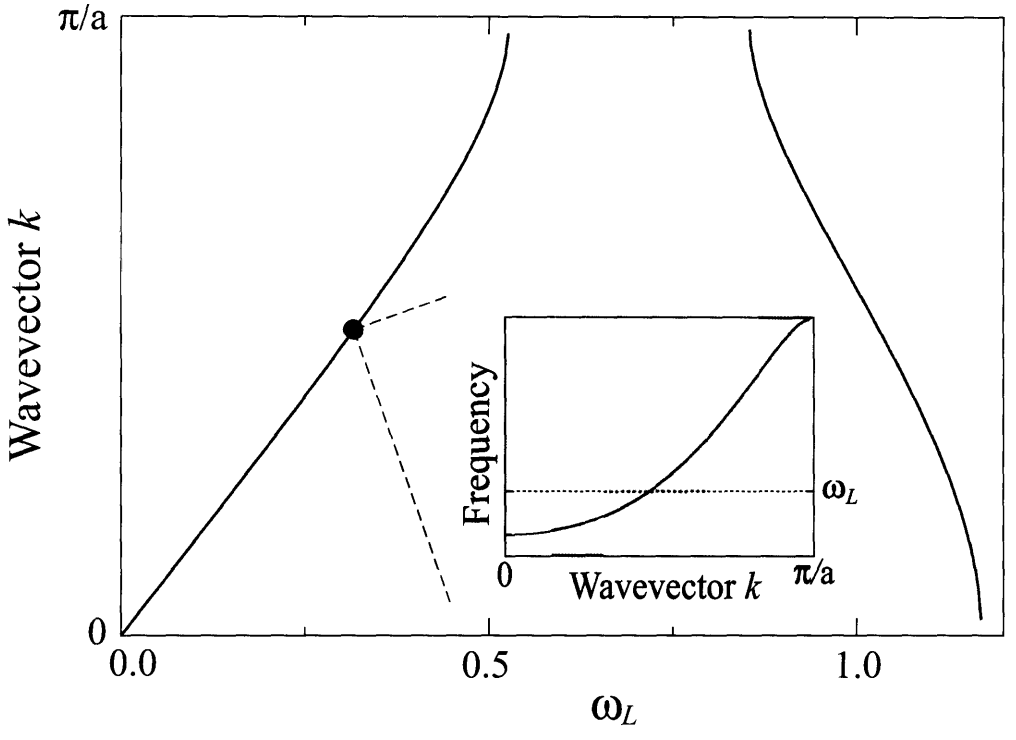

Figure 2-4: The dependence of the wavevector k at $\omega = \omega_L$ on ω_L, according to equation 2.7. The black dot refers to the value of ω_L used to calculate the band shown in the inset intersecting $\omega_L = 0.32$ at $k = \pi/2a$ for a 1D crystal of CsI in air. Note that for $0.527 < \omega_L < 0.854$, there is a band entirely within the gap.

At $\omega = \omega_L$, the wavevector is given analytically by the TMM as

$$k(\omega_L) = \arccos\left[\cos\frac{\omega_L d_1}{c} - \frac{\omega_L d_2}{2}\sin\frac{\omega_L d_1}{c}\right]. \tag{2.7}$$

This wavevector is plotted in Fig. 2-4. Note that for $0.527 < \omega_L < 0.854$ there is a band in the polariton gap that extends throughout the Brillouin Zone.

For the bands inside the polariton gap, we can characterize the decay rate of the field strength inside the polariton material of a mode of frequency ω_0 at $k = 0$ by $\sqrt{|\varepsilon(\omega_0)|}$, which we plot in Fig. 2-5 as a function of ε_∞ for various values of ω_T and ω_L. We see that the decay rate increases with increasing ω_T or ω_L, and asymptotes as a function of ε_∞.

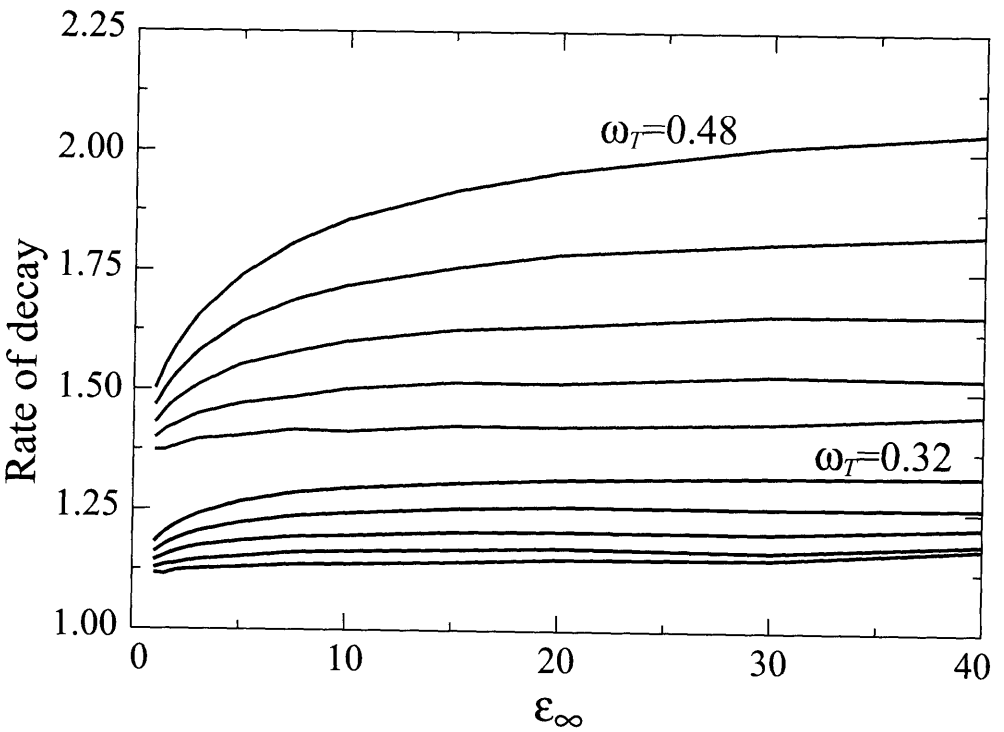

Figure 2-5: The rate of decay of the field strength inside the polariton material of a mode of freqency ω_0 at $k = 0$, given by: $\sqrt{|\varepsilon(\omega_0)|_{k=0}}$, as a function of ε_∞. The black lines are for $\omega_T = 0.32(2\pi c/a)$ and red are for $\omega_T = 0.48(2\pi c/a)$. From bottom to top, the successive curves of each color are for ω_L from $\omega_T + 0.04(2\pi c/a)$ to $\omega_T + 0.2(2\pi c/a)$ in increments of $0.04(2\pi c/a)$.

2.2.3 Crystal Transparency

The crystal becomes transparent to light at a frequency of $\omega_t = 0.3533$ in Fig. 2-3(b), where $\varepsilon = 1$ and the band intersects the line $\omega = ck$. In general, $\varepsilon(\omega) = \varepsilon_{\text{ambient}}$ when

$$\omega^2 \equiv \omega_t^2 = \frac{1}{\varepsilon_\infty - \varepsilon_{\text{ambient}}} \left(\varepsilon_\infty \omega_L^2 - \varepsilon_{\text{ambient}} \omega_T^2 \right) = \frac{\varepsilon_0 - \varepsilon_{\text{ambient}}}{\varepsilon_\infty - \varepsilon_{\text{ambient}}} \omega_T^2. \tag{2.8}$$

Note that when the slabs are in air, $\omega_t > \omega_L$. However, the point of transparency will be below ω_T when $\varepsilon_{\text{ambient}} > \varepsilon_\infty$ and $\omega_T^2 > \omega_L^2(\varepsilon_\infty/\varepsilon_{\text{ambient}})$. This provides a unique tuneability to a polaritonic system, since the transition to transparency can occur in a region of either rapidly or slowly varying index. In addition, note that there is no ω_T when $\varepsilon_\infty < \varepsilon_{\text{ambient}} < \varepsilon_0$.

2.3 2D Photonic Crystals

We will use our understanding of 1D crystals from the previous section to infer much of the relevant behavior in 2D. However, the existence of bands in a metallodielectric crystal will add rich, new phenomena and control possibilities that open the door for many exciting applications.

The band structure calculations of Zhang *et al.* [100] use exclusively a polariton gap between $[0.5, 1.0]$, while those of Kuzmiak *et al.* use $[1, 1.08]$. However, we will demonstrate that it is impossible to describe all of the complex elements of the band structures of 2D PPCs using a single choice of dielectric function parameters.

The two-dimensional polaritonic photonic crystal that we will examine consists of square rods of side $2r$ in air, with $2r/a = 0.25$, along the direction Γ to X.

2.3.1 Large n Cavities

We can understand the physics of a polaritonic crystal in two dimensions at frequencies below ω_T by first considering the modes of a square cavity in air with $k = 0$ along the rod. As $n \to \infty$, the reflectivity goes to 1 at all angles away from Brewster's an-

gle. To see how well this picture works for finite n, we compare the resonances of the square cavity to the metallic waveguide modes with frequencies

$$\omega_{lm} = \frac{\pi c}{2r\sqrt{\varepsilon}} \left(l^2 + m^2\right)^{1/2}, \tag{2.9}$$

where the modes with $l = 0$ or $m = 0$ are excluded from consideration since the fields should go to zero at the boundary. It is important to note, as in 1D, that there is are no true modes of the isolated rod with out-of-plane $k = 0$, but rather pseudomodes that become exact only in the limit of infinite n. Keeping this is mind, we will nevertheless refer to them as resonance modes, or resonance frequencies, since the true PPC states will retain the characteristics of these pseudomodes at finite n.

In Fig. 2-6, we plot the cavity resonance modes for a square rod with $n = 20$ for both TE and TM polarizations and compare them to the model frequencies ω_{lm}. The correspondence was made by examining the field pattern inside the rod to determine the nodal pattern; the TE modes show slightly better agreement with the frequencies ω_{lm}.

We have used square rods because of the simple, analytic solution given in Eq. (2.9) for the metallic waveguide modes confined to the plane with zero out-of-plane wavevector component. We infer that in a general 2D large n photonic crystal, the band structure are governed primarily by the resonances of a single rod, whose frequencies are determined by the rod's geometry, where the periodicity of the crystal will only introduce slight dispersion.

2.3.2 2D Band Structure

In this section, we use the insight gathered in section 2.3.1 to understand the band structure of a 2D PPC in the high index region. In Fig. 2-7, we show the band structure for the polaritonic material TlCl with $\omega_T = 12 \times 10^{12}\text{rad}/s$, $\omega_L = 30 \times 10^{12}\text{rad}/s$, and $\varepsilon_\infty = 5.1$ [46] (in normalized units, $\omega_T = 0.4$ and $\omega_L = 1$ for $a = 10\mu\text{m}$).

The most striking feature is that the TE and TM bands exhibit very different be-

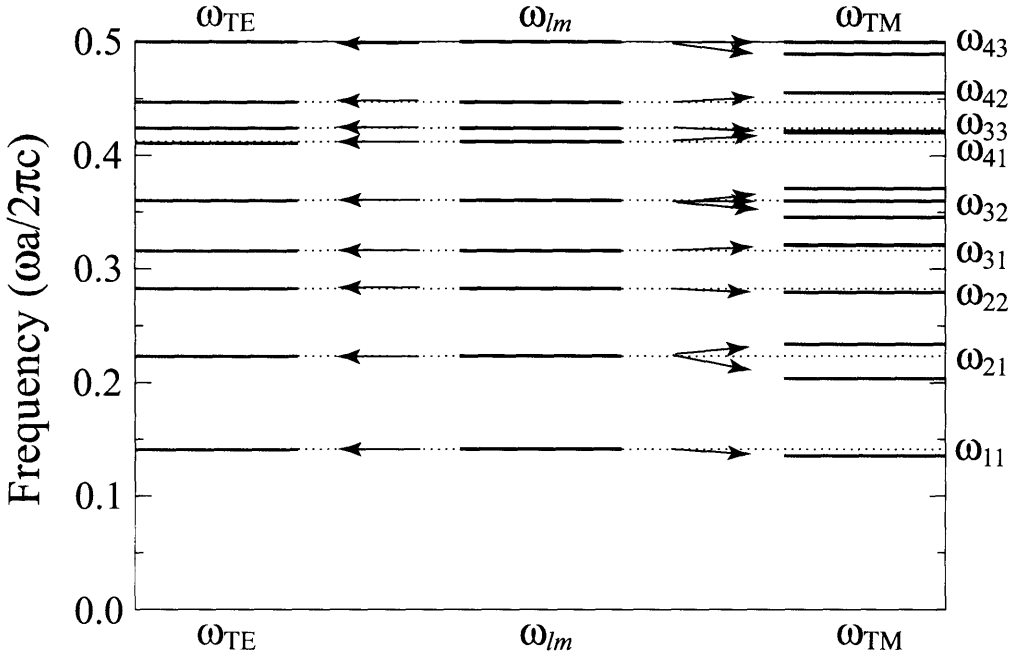

Figure 2-6: Resonance frequencies of a square cavity with $n = 20$ compared with the metallic waveguide frequencies ω_{lm}, shown as black horizontal lines in the center. TE modes are shown in red, TM in blue. The arrows indicate association between modes with fields of the same nodal structure.

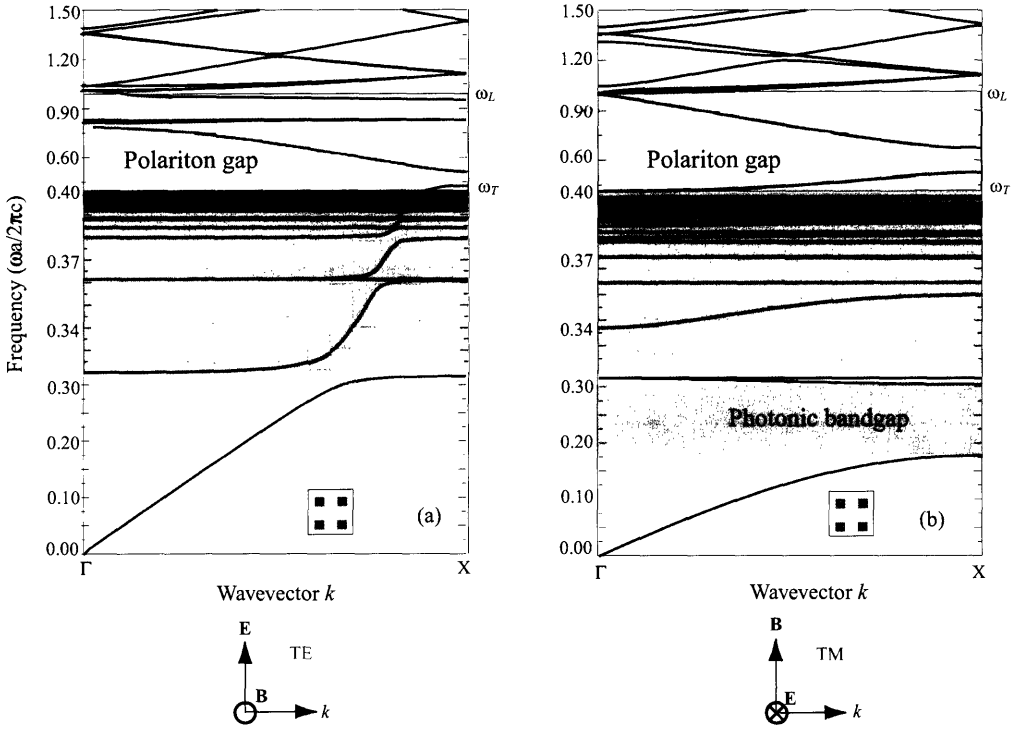

Figure 2-7: Band structure of a 2D PPC of square TlCl rods in air with $2r/a = 0.25$, $\omega_T = 0.4$, $\omega_L = 1.0$, and $\varepsilon_\infty = 5.1$. The TE bands are in red in (a), TM in blue in (b). Note the three different frequency spacings for the intervals $[0, 0.32]$, $[0.32, 0.4]$ (shaded in gray), and $[0.4, 1.5]$. The primary photonic band gap in the TM modes is indicated by purple shading.

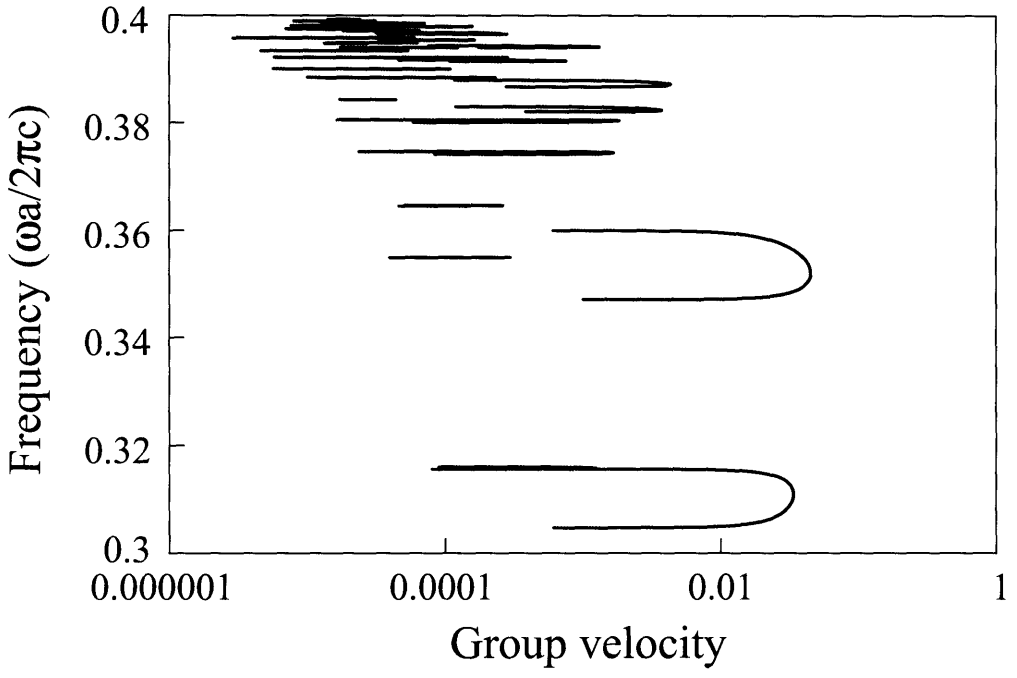

Figure 2-8: Group velocity in units of $2c$ as a function of frequency of the TM bands displayed in Fig. 2-7 in a 2D TlCl PPC.

havior. As expected, the TM bands closely resemble the 1D bands predicted by our simple tight-binding model since the **E** field is continuous everywhere. We demonstrate the low amount of dispersion by plotting the group velocity as a function of ω for all of the TM bands below ω_T in Fig. 2-8.

However, the TE bands are roughly linear, except near particular frequencies (which we identify as resonances of a single rod) where they rapidly flatten. Let us examine this behavior more closely. The frequency-dependent resonances solving $\hat{\omega}_{lm} = \pi c/2r\sqrt{\epsilon(\hat{\omega}_{lm})}$ are

$$\hat{\omega}_{lm}^2 = \frac{1}{2}\left(\omega_L^2 + \Omega_{lm}^2 - \sqrt{\left(\omega_L^2 + \Omega_{lm}^2\right)^2 - 4\Omega_{lm}^2\omega_T^2}\right), \tag{2.10}$$

where $\Omega_{lm} = \pi c(l^2+m^2)^{1/2}/2r\sqrt{\varepsilon_\infty}$. In Fig. 2-9, these frequencies are overlayed upon the TE bands near ω_T, to show the close agreement. The largest gap at the band edges in the TlCl crystal is relatively small (1.6%), occuring at the midgap frequency $\omega_{\text{mid}} = 0.3175$.

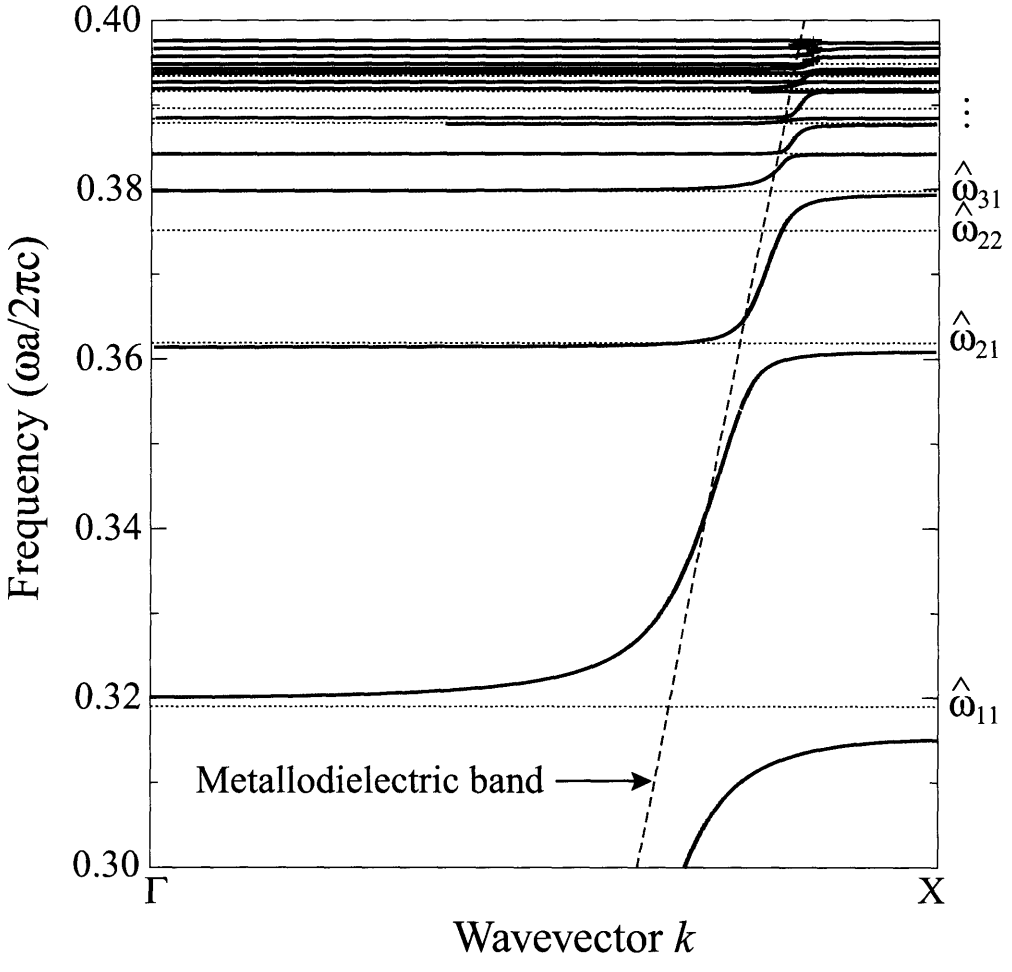

Figure 2-9: Matching of the frequency-dependent metallic waveguide resonance frequencies $\hat{\omega}_{lm}$ from equation 2.10 to the 2D crystal band structure of TlCl rods in air with $2r/a = 0.25$. The resonance frequencies are displayed as horizontal black, dotted lines; the lowest TE band of the metallodielectric crystal is shown as a dashed red line.

Why the difference between TE and TM modes? The answer lies in a comparison to the bands of a metallodielectric crystal with the same geometry of square metal rods, shown in Fig. 2-10. We point out one major difference between polarizations: the lowest TE band goes to zero frequency at Gamma, while the lowest TM band has a frequency $\omega(\Gamma) = 0.409$. In addition, there is a gap at X in the TE bands between 0.458 and 0.517, while the lowest TM band has frequency $\omega(X) = 0.546$.

It is clear from Fig. 2-9 that the lowest TE-polarized metallodielectric band increases in frequency from Γ to X in precisely the same fashion as the linear regions of the TE bands of the PPC. Thus, we interpret this observation as the anticrossing interaction of the highly localized resonance modes of the polaritonic rods with the modes of the metallodielectric crystal with the field completely removed from the rods, which is possible due to the small but finite leakage of the resonance modes out of the rods. In agreement with this simple characterization, the field near the band edges resembles the resonance mode of the rod closest in frequency.

The implications of this phenomenon on the importance of the location of the polariton gap are significant. There is a frequency cutoff $\omega_{\text{metal}} = 0.458$, the maximum frequency of lowest TE band of the metallodielectric crystal between Γ and X. Below ω_{metal}, all of the bands of the PPC are flat near Γ and X as a result of anticrossing between the metallodielectric TE mode and a particular rod resonance. Along a single band, the nodal surface of the field in the rod changes to match the two different resonance modes at Γ and X.

However, a drastic change in the band characterization occurs when $\omega_T > \omega_{\text{metal}}$. In Fig. 2-11, we plot the TE bands for an SiC crystal with $\omega_T = 1.49 \times 10^{14}/s$, $\omega_L = 1.79 \times 10^{14}/s$, and $\varepsilon_\infty = 6.7$ [46] (in normalized frequency units, for $a = 1.0\mu$m, $\omega_T = 0.5$ and $\omega_L = 0.60067$). For this set of parameters, $\hat{\omega}_{11} = 0.474$, and consequently we observe dramatically different behavior from all of the TE bands in the TlCl crystal with $\omega_T = 0.4$. Now all of the bands below ω_T, aside from the lowest, are very flat, much like the TM bands, representing a single resonance mode with slight dispersion resulting from interrod coupling of the weak fields outside the rods. In this case, the gaps are larger, reaching as high as 3.5% around $\omega_0 = 0.452$ in

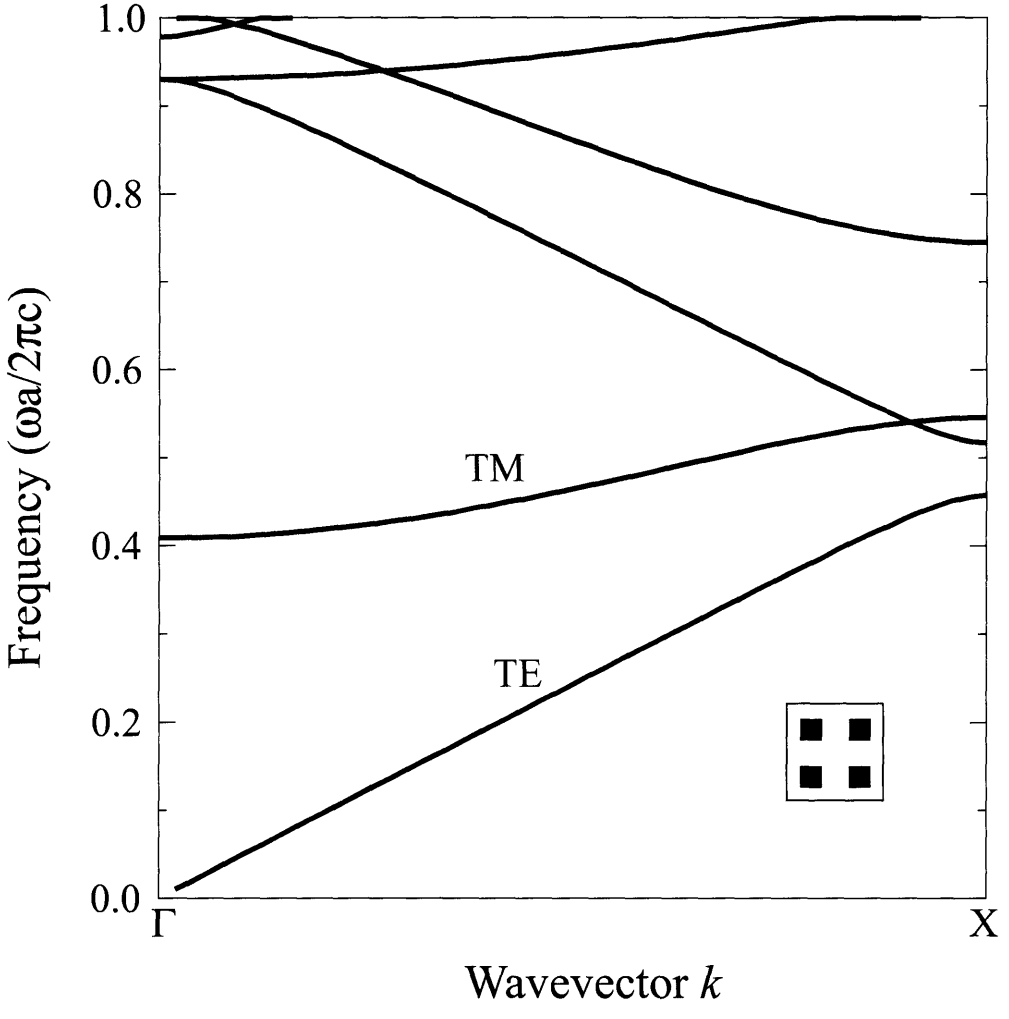

Figure 2-10: Band structure of a 2D crystal of square, metallic rods (in black) in air with $2r/a = 0.25$. TE bands are in red, TM in blue. Note the frequencies at the band edges of the first TE and TM bands.

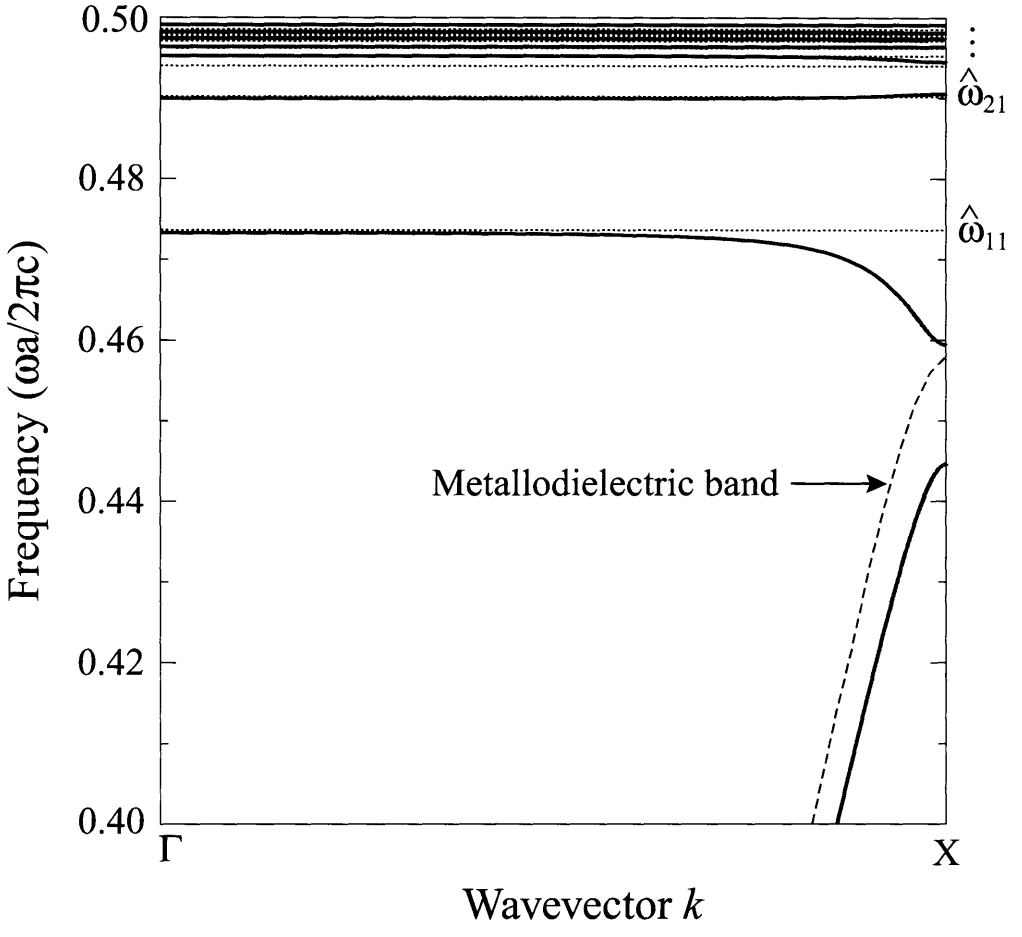

Figure 2-11: Matching of the cavity modes $\hat{\omega}_{lm}$ from equation 2.10 to the 2D crystal band structure of SiC rods in air with $2r/a = 0.25$. Note the distinctions from Fig. 2-9, due to the placement of ω_T above ω_{metal}.

Fig. 2-11.

Returning to Fig. 2-9, we observe that there seems to be no interaction with the $(2, 2)$ resonance mode near $\hat{\omega}_{22}$. The fact that no anticrossing occurs for this and any of the modes $(2l, 2m)$ with even indices is a direct result of the common symmetry of these modes. From Fig. 2-12, it is clear that the H_z component of the lowest metallodielectric crystal TE mode has even symmetry in the plane with respect to reflection about the line parallel to the x axis crossing through the center of the cell. For any mode with even indices, H_z is odd, so the overlap integral is zero. This symmetry argument explains why none of the bands formed through anticrossing will

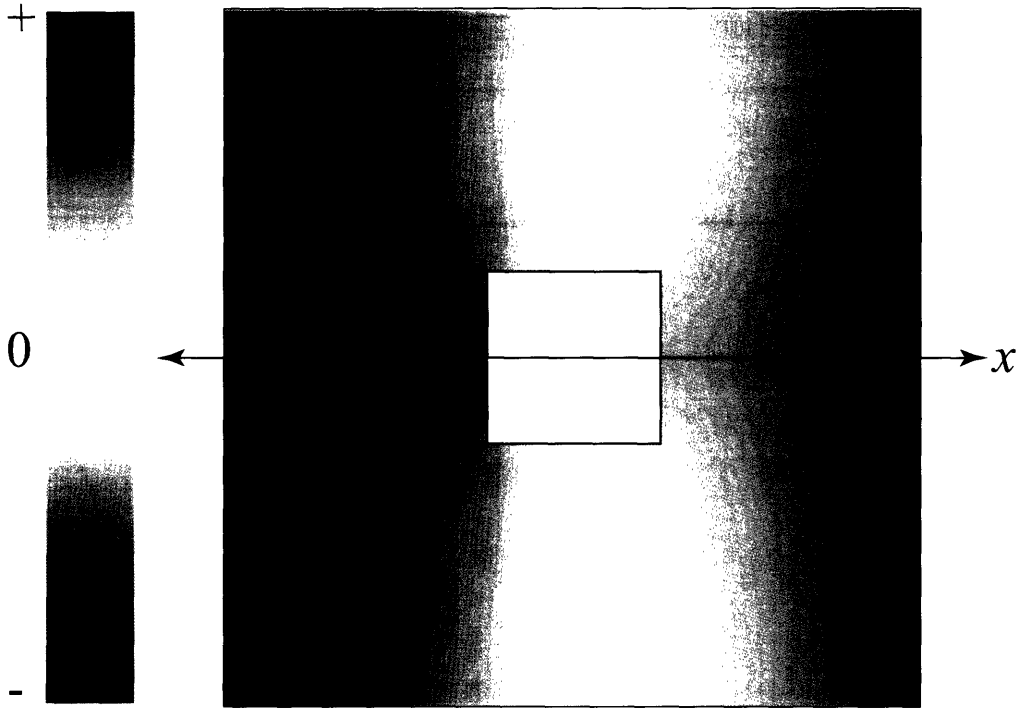

Figure 2-12: The Re$[H_z]$ field pattern for the metallodielectric crystal TE mode at frequency 0.3 $(2\pi c/a)$. Note the even symmetry in the plane with respect to reflection about the x axis. In this and all future field plots, blue indicates negative and red positive, with zero in white.

have field patterns resembling the $(2l, 2m)$ modes inside the rod, or resembling the one out of the two degenerate modes with frequency $\hat{\omega}_{2l,2m+1}$ with odd symmetry.

However, the question remains as to what happens to the modes of a single rod with odd symmetry in H_z once periodic boundary conditions are imposed. We expect that the same description that was used for the TM bands will apply: a flat band should be formed near the frequency $\hat{\omega}_{lm}$ whose dispersion is a result only of weak interrod coupling between nearby cells. Due to the greater localization of the modes with TE polarization, the dispersion is extremely small. The fact that there is no band near $\hat{\omega}_{22}$ in Fig. 2-9 is simply a result of the frequency grid spacing being chosen too large. In Fig. 2-13, we observe that the band is in fact present and has a width on the order of 6×10^{-7}.

For the case of degenerate modes of frequency $\hat{\omega}_{2l,2m+1}$, we show in Fig. 2-14, using

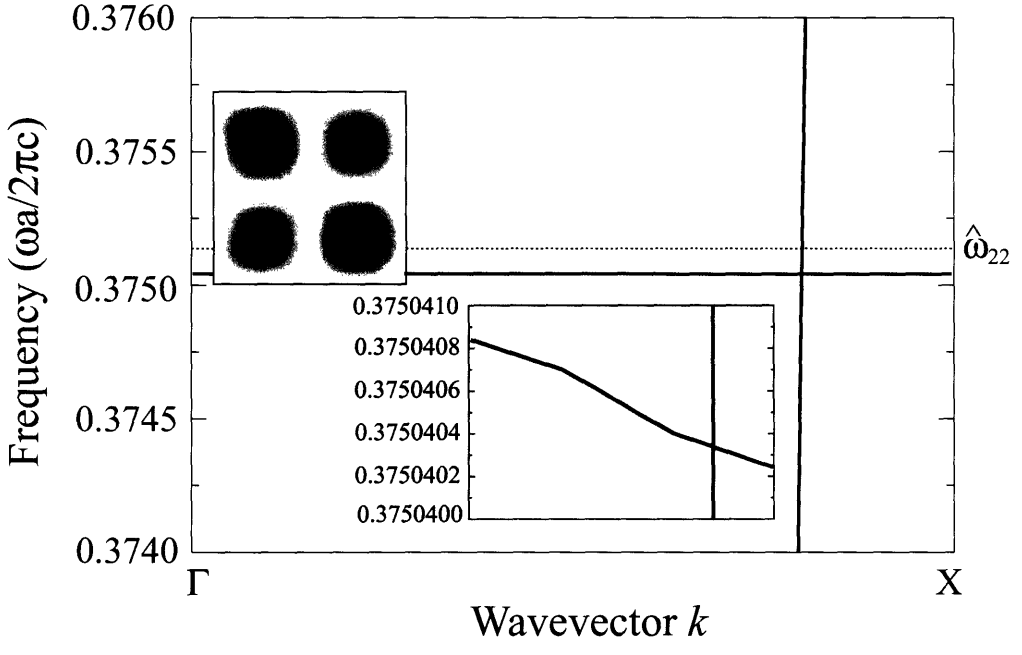

Figure 2-13: The $(2,2)$ localized resonance mode of the polariton rod, showing no anticrossing interaction. The H_z field pattern inside the rod is overlayed to show the odd symmetry with respect reflection about the x axis. Note the frequency interval in the inset, demonstrating the extremely small band width of 6×10^{-7}.

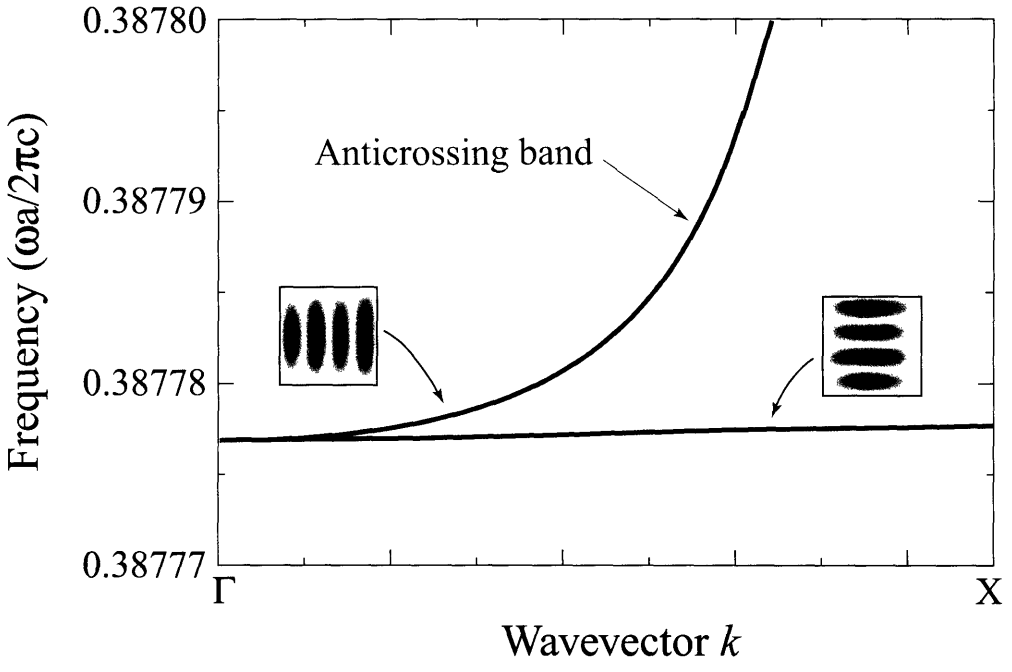

Figure 2-14: The contrast between the interactions of the $(4,1)$ and $(1,4)$ modes with the lowest metallodielectric TE mode. The Re$[H_z]$ field patterns inside the polariton rod are overlayed. Note the anticrossing with the mode of even symmetry across the x-axis, and the dispersionless band with band width 8×10^{-7} for the mode of odd symmetry.

the $(4,1)$ and $(1,4)$ modes as an example, that the even symmetry mode exhibits the anticrossing phenomenon, while there is a flat band corresponding to the mode of odd symmetry. Again, the band width in this case is extremely small, on the order of 10^{-6}.

2.3.3 Node Switching

There are several interesting metallic waveguide mode pairs connected by a single TE-polarized PPC band, such as $(l,m) = (4,1)$ and $(3,3)$, where the separation between the two frequencies $\hat{\omega}_{lm}$ in the PPC is extremely small ($0.0007(2\pi c/a)$ for the TlCl crystal parameters in section 2.3.2). Along this band, the nodal structure inside the rod is forced to continuously change from one pattern to another, as shown in Fig. 2-15. This phenomenon provides an unprecedented capability for a state localized in

the rod to change its coupling behavior over a very small frequency range. In terms of the practical impact of this phenomenon on potential applications, the fact that some of these mode pairs, e.g. (4,1)-(3,3) and (3,4)-(5,1), can be found at frequencies reasonably far away from the region near ω_T, where losses can become very large, bodes well for future research.

2.3.4 The metallic regime

We now switch gears, to the other side of the discontinuity of $\varepsilon(\omega)$ at ω_T. Above ω_T, $\varepsilon(\omega)$ is very negative, so we expect the polaritonic rods to behave as metals and expel nearly all of the field. Therefore, the possibility of finding bands in the region close to ω_T is governed by the existence of bands in the metallodielectric crystal in Fig. 2-10 at these frequencies. The positions of the gaps in both the TE and TM-polarized bands will mark exactly where polariton excitations are prohibited in the photonic crystal.

In Fig. 2-16(a), we plot the magnetic field component H_z of the TE band at the frequency $\omega = 0.44$, where $\varepsilon(\omega) = -65.2$, for the same TlCl PPC in section 2.3.2 with $\omega_T = 0.4$, $\omega_L = 1.0$. We observe in Fig. 2-16(b) that there is no TM band at ω_T, as we would expect since the lowest frequency metallodielectric TM mode is at $\omega(\Gamma) = 0.409$ (see Fig. 2-10).

In Fig. 2-17, we plot the electric field component E_z at the frequency $\omega = 0.523$ in a 2D square PPC of SiC rods. There is now no TE band at ω_T, since the phonon frequency is now within the TM gap $[0.458, 0.517]$. Deviations from metallic behavior are slight for the entire band, even at $\omega = 0.523$ near the band edge. Previous metallodielectric crystal band structure calculations by Kuzmiak, Maradudin and Pincemin [52] using the frequency-dependent dielectric function

$$\varepsilon_{\text{metal}} = 1 - \frac{\omega_p^2}{\omega^2},$$

where ω_p is the plasmon frequency of the metal, have displayed similar behavior to that in Fig. 2-10 for frequencies below ω_p where $|\varepsilon|$ is less than around 10, thus we are

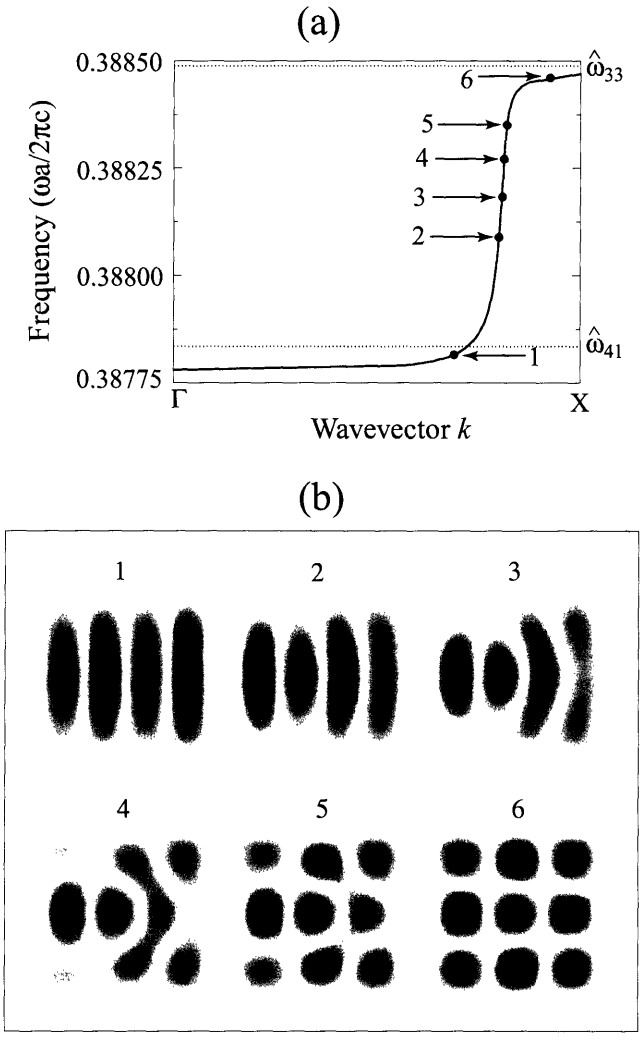

Figure 2-15: Node switching: (a) The 6th TE band connecting the (4,1) cavity mode to the (3,3) cavity mode of a 2D PPC with square rods of TlCl, $2r/a = 0.25$, with selected frequencies indicated by the numbered arrows. (b) The real part of H_z inside the rod at the frequencies indicated in (a) between 0.38779 and 0.38845.

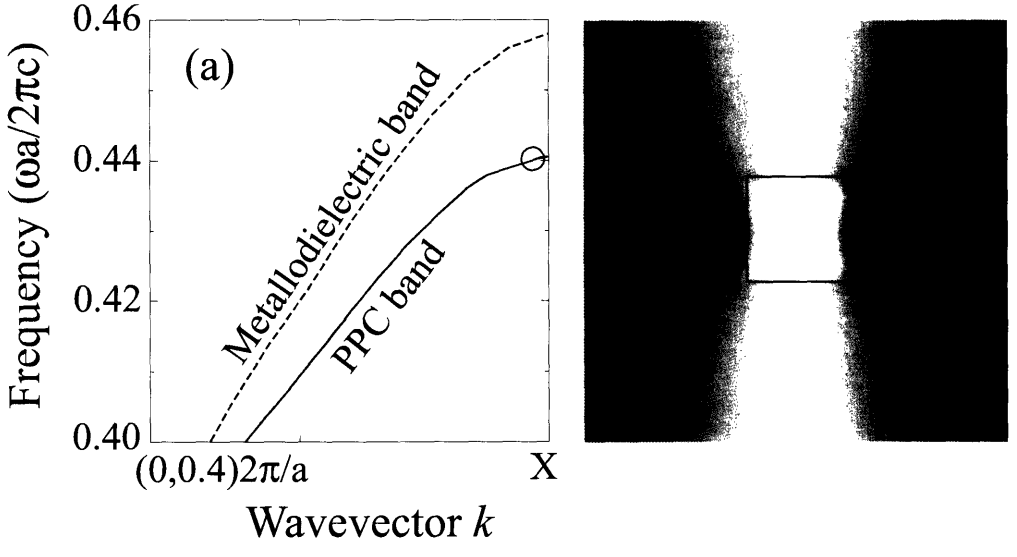

Figure 2-16: Metallic behavior in the TE bands: (a) The first TE band above ω_T in a 2D TlCl PPC in solid red, with the corresponding portion of the lowest TE band in a metallodielectric crystal in dashed red. The open circle contains the portion of the PPC band at frequency $\omega = 0.44$, for which the real part of the magnetic field component H_z is plotted in a single supercell in (b), with the rod outline in black. The wavevector axis begins not at Γ but at $0.8\pi/a$.

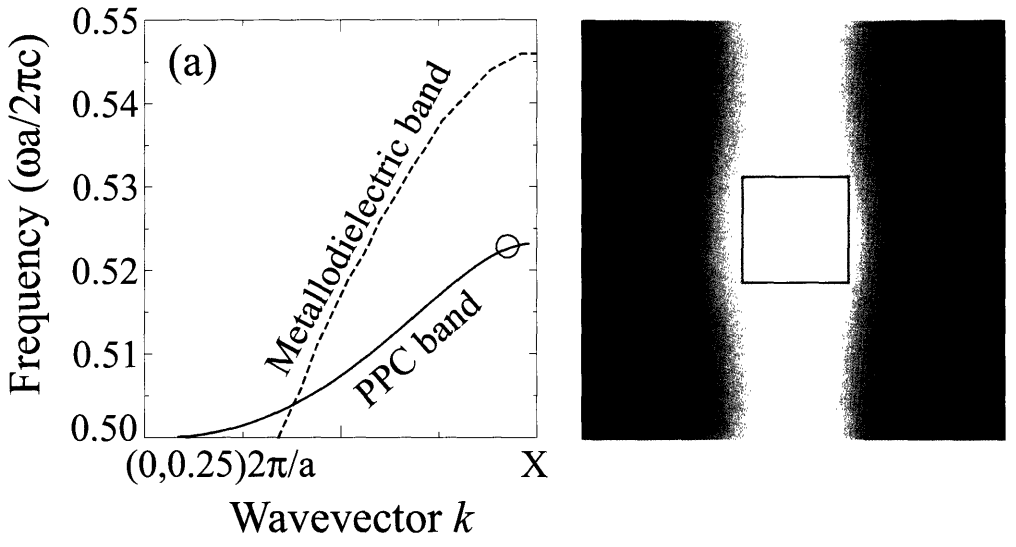

Figure 2-17: (a) The first TM band above ω_T in a 2D SiC PPC in solid blue, with the corresponding portion of the lowest TM band in a metallodielectric crystal in dashed blue. The open circle contains the portion of the PPC band at frequency $\omega = 0.523$, for which the real part of the electric field component E_z is plotted in a single supercell in (b), with the rod outline in black. The wavevector axis begins not at Γ but at $\pi/2a$.

clearly well within the regime regularly considered as a metallic at $\omega = 0.523$ since $\varepsilon(\omega) = -24$.

These observations lead us to the introduction of the phenomenon of *flux expulsion* in PPCs, where small changes in ω near the interface between the metallic and dielectric photonic bandgap regimes can induce enormous variations in the topology of the field pattern. We demonstrate this phenomenon in Fig. 2-18. Using other geometries and/or other materials to surround the polaritonic medium (in particular, nonlinear materials), this tool should be extremely useful as a switch to shift light in and out of different physical regions of the crystal. In the following section, we will examine more closely the effect of losses, and we will find that for some polaritonic media, losses are restricted to a sufficiently small area around ω_T that practical utilization of flux expulsion should be possible.

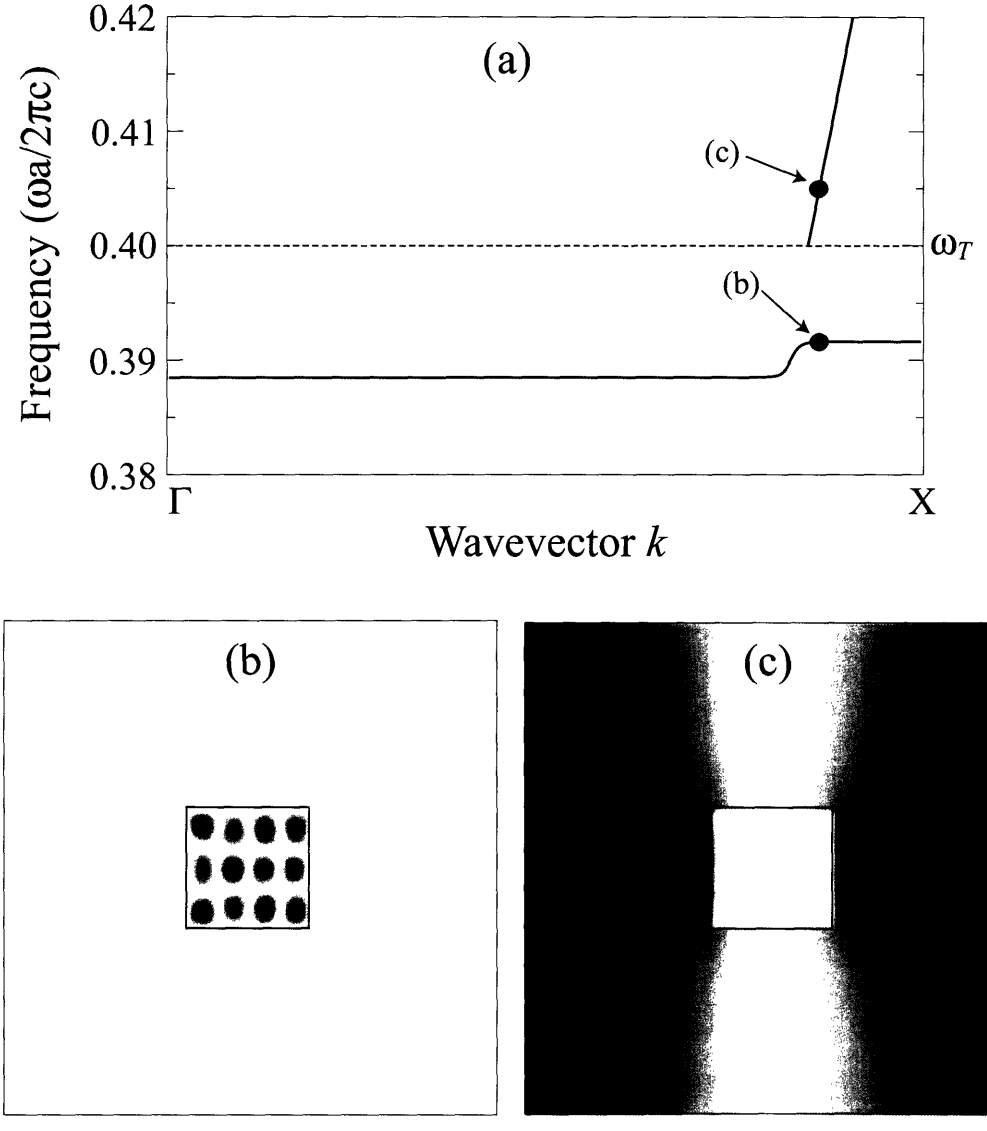

Figure 2-18: Flux expulsion: (a) The band directly above ω_T and a flat band just below ω_T in a 2D PPC of TlCl rods with $2r/a = 0.25$. The Bloch states with $k = 0.43(2\pi/a)$ at the frequencies $\omega = 0.3916$ and $\omega = 0.403$ are marked by arrows. (b) The field pattern of the real part of H_z at $\omega = 0.3916$, where $\varepsilon = 649$. (c) The field pattern of the real part of H_z at $\omega = 0.403$, where $\varepsilon = -1773$. Note the extreme contrast between the localization of the field inside the rod in (b) and the complete flux expulsion in (c).

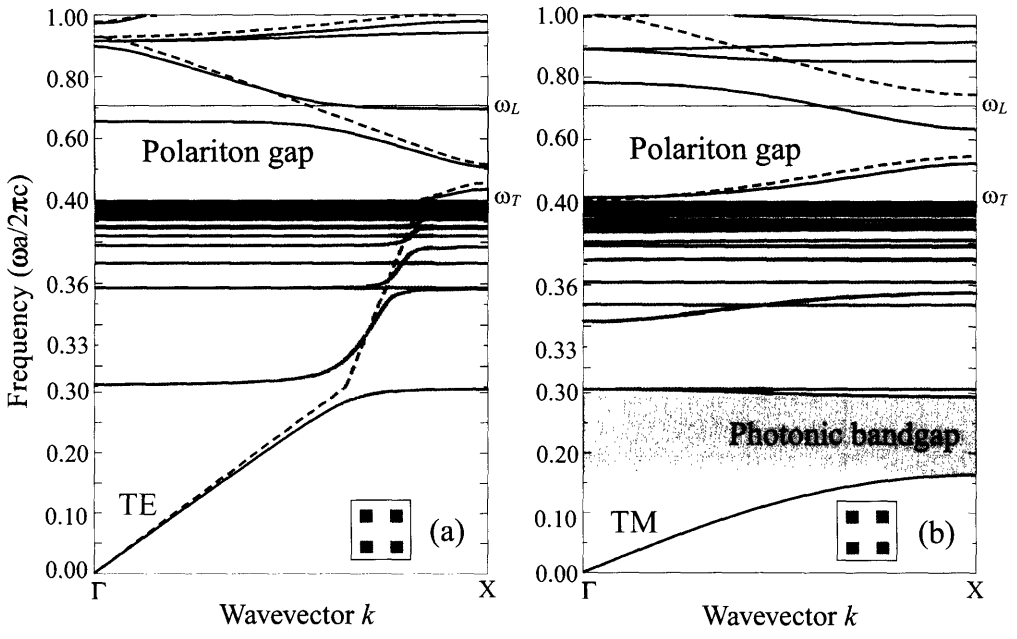

Figure 2-19: Band structure of a 2D polaritonic photonic crystal with square symmetry of square $LiTaO_3$ rods in air with $s/a = 0.25$, $\omega_T = 0.4(2\pi c/a)$, $\omega_L = 0.703(2\pi c/a)$, and $\varepsilon_\infty = 13.4$. The TE (**H** out of plane) bands are in red in (a), TM (**E** out of plane) in blue in (b). Note the three different frequency spacings for the intervals $[0, 0.31](2\pi c/a)$, $[0.31, 0.4](2\pi c/a)$ (shaded in gray), and $[0.4, 1.0](2\pi c/a)$. The primary photonic band gap in the TM modes is indicated by purple shading. The TE(TM) bands of a metallodielectric crystal obtained by replacing $LiTaO_3$ by a perfect metal are given by the red(blue) dashed lines.

2.3.5 2D $LiTaO_3$ PPC

In Fig. 2-19, we plot the band structure from Γ to X of a 2D photonic crystal of square rods with side s ($s/a = 0.25$) in a square lattice. The rods are taken to be $LiTaO_3$, a typical polaritonic material with a large polariton gap from $\omega_T =$ 26.7 THz to $\omega_L = 46.9$ THz, and $\varepsilon_\infty = 13.4$. We set $a = 4.5\mu$m so that $\omega_T = 0.4(2\pi c/a)$ and $\omega_L = 0.703(2\pi c/a)$. We overlay with dashed lines the band structure for the metallodielectric crystal obtained by replacing $LiTaO_3$ with a perfect metal. In addition, we highlight the most important sections: directly above and below ω_T.

Note the existence of flat bands in both polarizations in the high index region below ω_T, as observed in earlier work [100, 51]. As before, we find that these bands correspond extremely closely to localized resonance modes [54] in isolated rods with

slight dispersion about a frequency given (to within less than 1% error in most cases) by the following analytic expression:

$$\hat{\omega}_{lm}^2 = \frac{1}{2}\left(\omega_L^2 + \Omega_{lm}^2 - \sqrt{\left(\omega_L^2 + \Omega_{lm}^2\right)^2 - 4\Omega_{lm}^2\omega_T^2}\right), \tag{2.11}$$

where $\Omega_{lm} = \pi c(l^2 + m^2)^{1/2}/s\sqrt{\varepsilon_\infty}$.

Consider one of the several resonance pairs (l, m), (l', m') with a very small frequency separation that are connected by a TE band through this interaction, such as $\hat{\omega}_{33} - \hat{\omega}_{41} = 0.0007(2\pi c/a)$. Along this band, the nodal structure of the field inside the rod, perpendicular to the plane, is forced to continuously mutate from one pattern to another, as shown in Fig. 2-20. This node switching phenomenon provides an unprecedented capability to drastically alter the coupling behavior of a localized state over a very small frequency range.

In our calculation with $\omega_T = 0.4(2\pi c/a)$, ω_T is outside the TE metallodielectric bandgap from $[0.458, 0.517](2\pi c/a)$ and inside the TM bandgap $[0, 0.409](2\pi c/a)$. Correspondingly, we see in Fig. 2-19 that there is a TE PPC band that intersects ω_T, at $k = 0.432\pi/a$, but no TM PPC band directly above ω_T; the lowest frequency TM-polarized state above ω_T is at $k = \Gamma$, $\omega = 0.415(2\pi c/a)$.

It is clear from our discussion of how flux can be isolated to either of the two opposite physical regions of the crystal that small changes in ω can induce enormous variations in the field profiles due to the rapid change in ε. In Fig. 2-21(a), we explore an interband transition at fixed wavevector from below ω_T to a frequency inside the polariton gap. The light is transferred almost completely from inside the rod at $\omega = 0.3916(2\pi c/a)$ (Fig. 2-21(b)) to the ambient region at $\omega = 0.403(2\pi c/a)$ (Fig. 2-21(c)). With a wide range of options in terms of crystal geometries and ambient materials, the utility of this flux expulsion is manifest. For example, using a nonlinear material as the surrounding medium, this phenomenon could be utilized as a switch to shift light in and out of different physical regions of the crystal.

In order to incorporate losses in the polaritonic material, we use the well-known

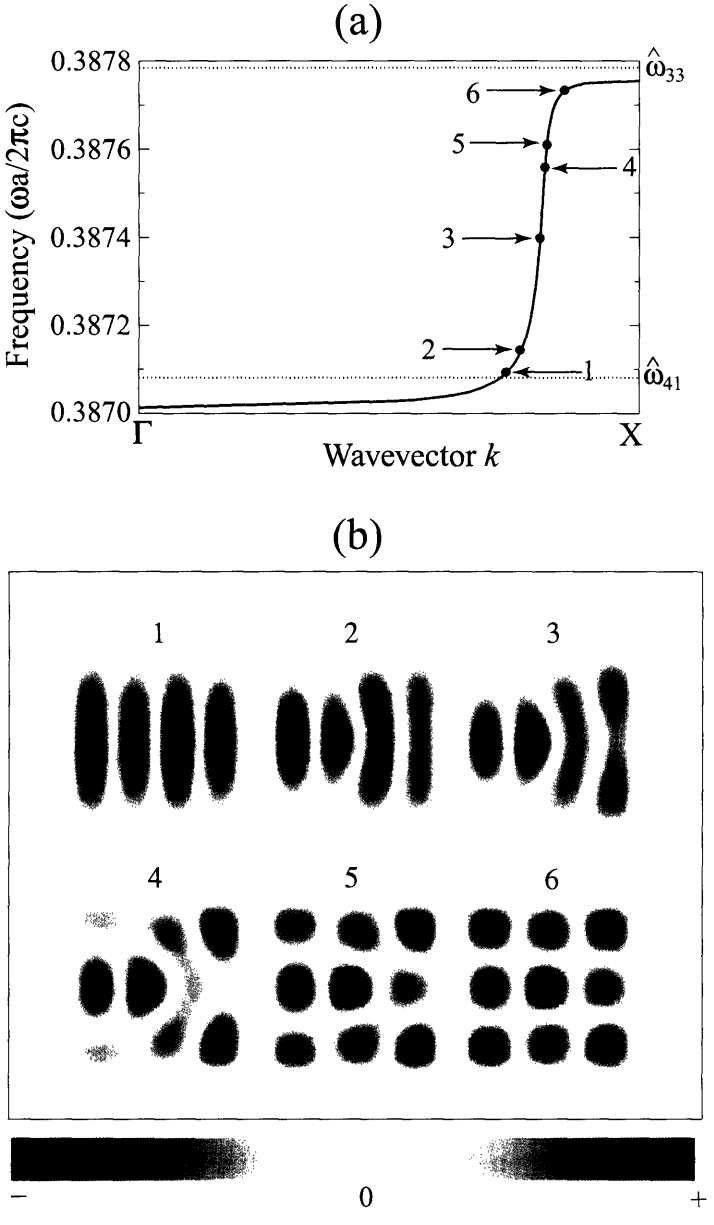

Figure 2-20: Node switching: (a) The TE band connecting the (4,1) cavity mode to the (3,3) cavity mode of a 2D PPC with square rods of $LiTaO_3$, $s/a = 0.25$, with selected frequencies indicated by the numbered arrows. (b) The real part of H_z inside the rods at the frequencies indicated in (a) between $0.3871(2\pi c/a)$ and $0.38775(2\pi c/a)$.

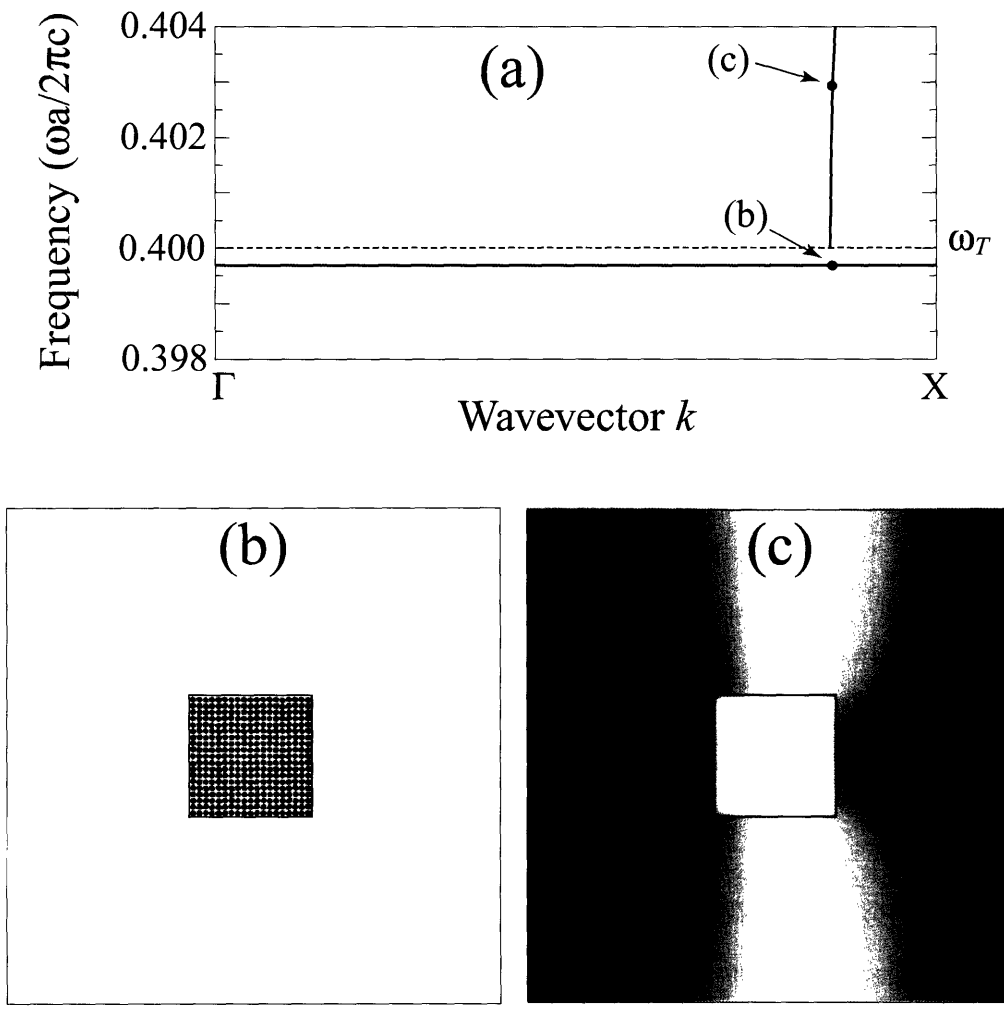

Figure 2-21: Flux expulsion: (a) The band directly above ω_T and a flat band just below ω_T in a 2D PPC of $LiTaO_3$ rods with $s/a = 0.25$ with the frequencies $\omega = 0.3916(2\pi c/a)$ and $\omega = 0.403(2\pi c/a)$ marked by black dots. The wavevector at both of these frequencies is $0.43(2\pi/a)$. (b) The field pattern of the real part of H_z at $\omega = 0.3916(2\pi c/a)$, where $\varepsilon = 649$. (c) The field pattern of the real part of H_z at $\omega = 0.403(2\pi c/a)$, where $\varepsilon = -1773$. Note the extreme contrast between the localization of the field inside the rod in (b) and the complete flux expulsion in (c).

model for the dielectric function [46]

$$\epsilon(\omega) = \varepsilon_\infty \left(1 + \frac{\omega_L^2 - \omega_T^2}{\omega_T^2 - \omega^2 - i\omega\Gamma}\right), \tag{2.12}$$

where Γ represents the width of the absorption peak in $\mathrm{Im}[\varepsilon(\omega)]$. Sigalas *et al.* implemented equation 2.12 in transmission calculations to determine the photonic bandgaps in a PPC [84]. Along the ordinary axis of the $LiTaO_3$ crystal, $\Gamma = 0.94$ THz $= 0.013(2\pi c/a)$. Although we have focused on instances of optical phenomena very close to ω_T, these effects will also occur well away from ω_T. The second TE band in the PPC exhibits a transition from the $\hat{\omega}_{11}$ to the $\hat{\omega}_{21}$ localized rod state, ending at the frequency $0.36(2\pi c/a)$. Moreover, the TE band ending at ω_T inside the polariton gap extends to above $0.44(2\pi c/a)$. Therefore, the node switching and flux expulsion phenomena can be realized with states removed from ω_T by at least 3Γ. Hence, the perturbations to these states due to losses are negligible, allowing for their experimental observation in a physical crystal. Key to this argument are the large value of $\varepsilon_0 = 41.4$ and the small ratio $\Gamma/\omega_T = 0.032$.

2.3.6 Other phenomena

We have chosen to focus on the large n and metallic limits, because the new physics in 2D versus 1D occurs in these frequency ranges. However, the other two phenomena mentioned in section 2.2 are still relevant: the transparency condition is unchanged, and there are bands either close to or intersecting ω_L. In particular, although no analytic solution is known to exist for the wavevector at ω_L, we find that $k(\omega_L)$ is independent of ω_T, as was the case in 1D.

2.4 Losses

In sections 2.2 and 2.3, we provided a comprehensive analysis of the band structures of photonic crystals in 1D and 2D composed of lossless polariton materials with a wide range of phonon frequencies and dielectric limits. As in Sec. 2.3.5, the model to

correct for losses is the dielectric function

$$\epsilon(\omega) = \varepsilon_\infty \left(1 + \frac{\omega_L^2 - \omega_T^2}{\omega_T^2 - \omega^2 - i\omega\Gamma}\right), \tag{2.13}$$

where the magnitude of the losses is represented by Γ. Shown in Fig. 2-22 are the real and imaginary parts of the dielectric function for $LiTaO_3$, using the parameters given by Schall *et al.* [78]: $\omega_T = 26.7 \times 10^{12}\text{rad}/s$, $\omega_L = 46.9 \times 10^{12}\text{rad}/s$, $\Gamma = 0.94 \times 10^{12}\text{rad}/s$ and $\varepsilon_\infty = 13.4$ along the ordinary axis of the atomic crystal.

Although losses will clearly become important near ω_T, at frequencies separated from ω_T by more than Γ the dielectric function is mostly unchanged and the effects of losses should be minimal. For the $LiTaO_3$ parameters given above, with a lattice constant of $a = 4.5\mu\text{m}$, the second TE band of the lossless crystal will exhibit a transition from the $\hat{\omega}_{11} = 0.293(2\pi c/a)$ to the $\omega_{12} = 0.331(2\pi c/a)$ localized rod state. In this range, the real part of the dielectric function is qualitatively equivalent to the lossless case, and deviations never exceed 3.2%. Moreover, the TE band ending at ω_T inside the polariton gap closely follows the lowest TE band of the metallodieletric crystal, as in Fig. 2-16, which terminates at $0.458(2\pi c/a)$. The PPC states can thus be chosen to lie well within the region of large negative dielectric and yet be sufficiently removed from ω_T to minimize the effects of losses.

Therefore, the node switching and flux expulsion phenomena can be realized with states subject to little perturbation due to their removal from ω_T by at least 2.5Γ. Key to this analysis involving $LiTaO_3$ are the large value of $\varepsilon_0 = 13.4$ and the small ratio $\Gamma/\omega_T = 0.032$, and other materials with similar properties should also result in practical experimental utility. Indeed, we have verified these conclusions in Chapter 3 with more extensive calculations including losses in our model PPC system with $LiTaO_3$ rods.

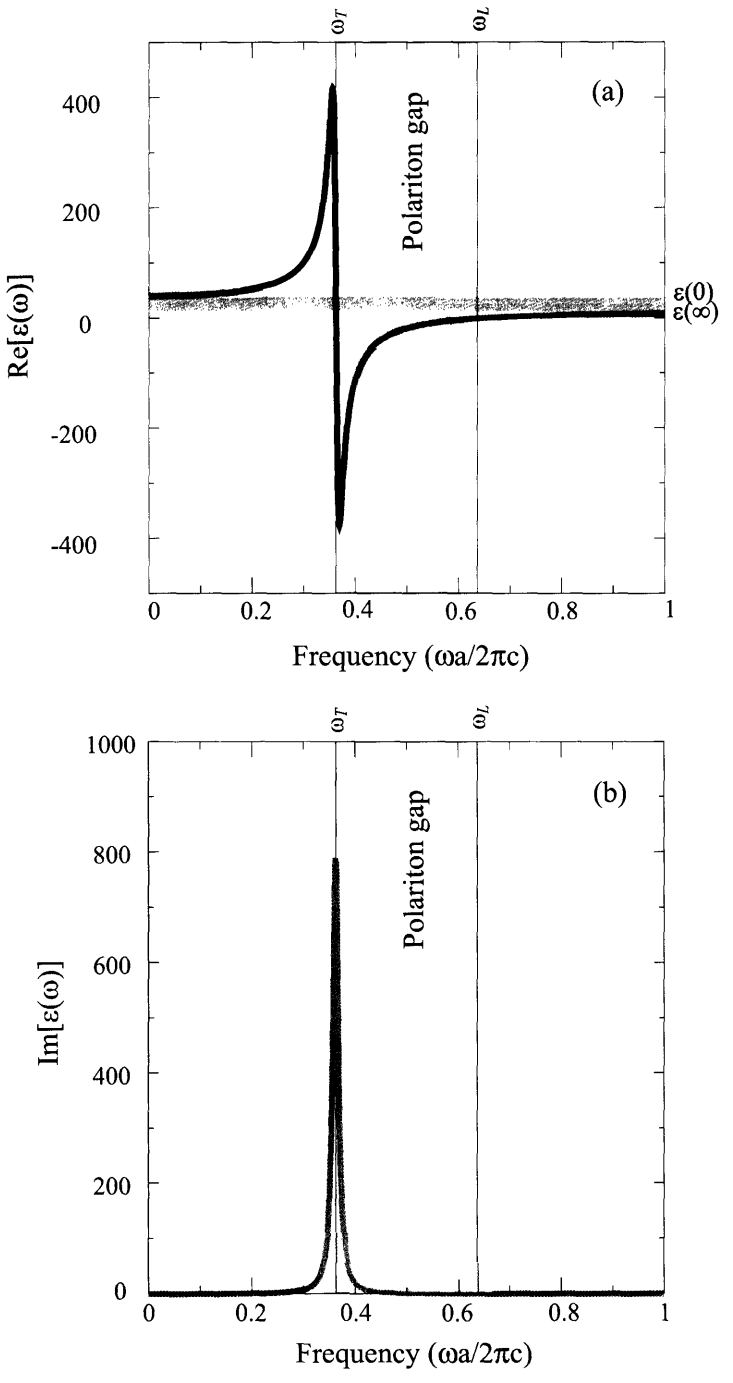

Figure 2-22: The real and imaginary part of the polariton dielectric function for $LiTaO_3$ with $\varepsilon_\infty = 13.4$ and $a = 4.5\mu$m, leading to normalized frequencies $\omega_T = 0.3628$, $\omega_L = 0.6372$, and $\Gamma = 0.0128$.

2.5 Conclusion

The ability to study many different optical response regimes using the same physical PPC structure is an extremely powerful tool. We have presented models for all of the relevant frequency domains of a polaritonic material: the high-index region below ω_T, the metallic region above ω_T, and the low-index region near ω_L. In previous works [100, 51], the authors have noted the presence of flat, dispersionless bands near ω_T. We verify these conclusions and provide a quantitative description for the origin of these bands related to the localized resonance modes of a high-index slab (1D) or rod (2D). The success of this model is shown to be excellent for a 1D slab PPC of CsI in air.

In a 2D square lattice of TlCl rods, a distinction between TE and TM polarizations is immediately apparent. Anticrossing behavior in the TE modes, contrasted against the flat TM bands reminiscent of the 1D PPC band structure, is explained by the interaction of the lowest metallodielectric TE band with the localized resonances of a single rod. We demonstrate that this conclusion is correct using a crystal of SiC rods with a larger value of ω_T inside the metallodielectric TE bandgap to eliminate the anticrossing interactions. This property provides the unique opportunity to continuously vary the coupling behavior of a TE band over a very small frequency range, since the nodal structure of the field inside the polariton rod matches different resonances of the isolated rod at Γ and at X.

A further use of the 2D metallodielectric band structure is for predicting the presence of PPC bands directly above ω_T in the metallic regime. The locations of the TE and TM metallodielectric bandgaps play the deciding role in determining if and where the PPC bands occur. By exploiting the adjacency of the large index and metallic regimes, it is possible to realize flux expulsion, effecting enormous changes in the location of the electromagnetic energy over a small frequency range.

In the region near ω_L, important points to note are the penetration of the phonon-like band of the bulk polaritonic material near Γ into the polariton gap due to the air acting as a defect layer, inducing a nonzero wavevector at ω_L that we have determined

analytically in 1D. In addition, there is a characteristic frequency where the crystal becomes transparent. We have calculated conditions under which this point is above or below the polariton gap.

For practical applications, the effects of losses in the polaritonic medium are at a maximum near ω_T. However, using $LiTaO_3$ as an example material, we found that the high index and metallic regimes overlap with frequency ranges where the imaginary part of ε is relatively small. Therefore, all of these phenomena should be readily accessible experimentally.

We note that it is remarkable that we have been able to observe all of the above phenomena using a single geometric structure. For wavevectors between Γ and K, the continuous variation of the dielectric profile as a function of distance along the propagation direction introduces the need for a discretization approximation to the physical structure as well as a significant increase in computational resources. We have performed preliminary calculations to verify that our conclusions regarding the shape and position of the bands that leads to the node switching and flux expulsion phenomena apply conceptually without any major modifications. The ability to vary the size of the rods and the translational symmetry group of the crystal should provide a further level of tuneability to make it easier to isolate many of the effects described in this work.

In addition, our research has provided compelling support for the inclusion of the vectorial eigenmode expansion method in the set of techniques such as layer KKR [60] and the multiple multipole method [61], suitable for not only polaritonic systems but any material with a frequency-dependent optical response. We have determined the eigenmode basis to be well converged at 40 for all frequency regimes of the PPC. In both accuracy and efficiency, this technique surpasses the traditional time-domain and plane-wave method techniques. It provides the means to tackle further problems involving polaritonic photonic crystals, including dissipative systems and more complicated crystal structures. Indeed, the complex wavevector solutions for the eigenmode problem in the case of lossy materials are readily available, and only numerical problems related to the stability of the modefinder when losses are

introduced have prevented a full band structure calculation of a lossy PPC at this time. With further research, the nascent field of phonon-polariton excitations in photonic crystals promises to bring more exciting new phenomena and developments.

Chapter 3

The Nature of Lossy Bloch States in Polaritonic Photonic Crystals

Segments of this chapter have previously appeared in: Huang, Lidorikis, Jiang, Joannopoulos, Nelson, Bienstman, and Fan, Phys. Rev. B ***69*** *195111 (2004).*

Recent advances [35, 36] in the study of photonic crystals composed of materials which exhibit phonon-polariton excitations have revealed a variety of optical phenomena that are intimately related to the interplay between the strongly dispersive nature of these polar media and the structural dispersion of the crystal. These features involve (i) small frequency variations in bands with large regions of low group velocity that produce a polarization-dependent restructuring of the nodes in the field pattern (*node switching*) and (ii) transitions across the polariton gap boundary at the frequency ω_T that induce *flux expulsion* to and from the polariton material and the surrounding ambient dielectric. Previous polaritonic photonic crystal (PPC) band structure simulations [100, 51, 85, 20, 35, 36] have incorporated the polariton material as a lossless frequency-dependent dielectric. However, the node switching and flux expulsion phenomena are tied directly to the strong frequency-dependence of the dielectric function near ω_T, where losses are expected to be greatest.

A simple model for the dielectric function of a polaritonic material with losses is

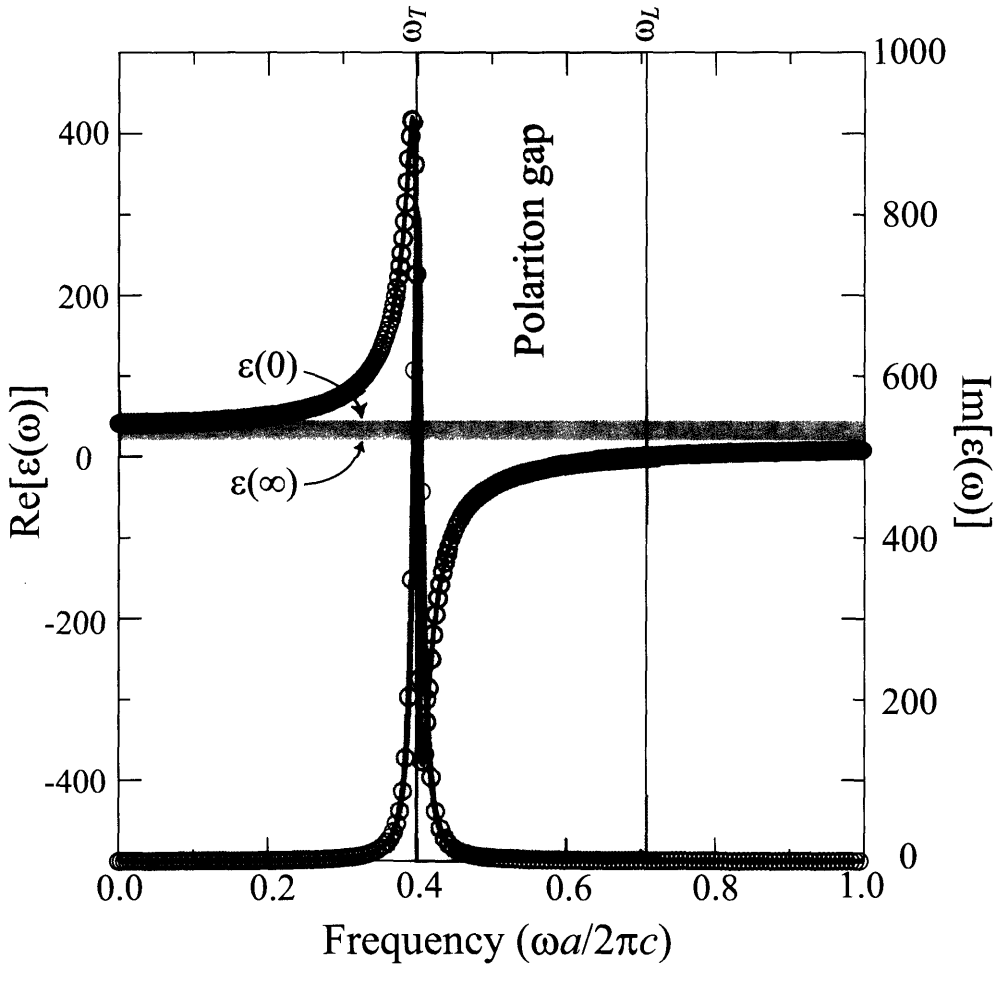

Figure 3-1: The polariton dielectric function for $LiTaO_3$ with $\varepsilon_\infty = 13.4$ and $a = 4.5\mu$m, leading to normalized frequencies $\omega_T = 0.4$, $\omega_L = 0.703$ and $\gamma = 0.014$. The real part, ε_1, is in black and the imaginary part, ε_2, is in red. Note the excellent agreement between the exact value from Eq. 3.1 used in frequency-domain simulations (solid line) and approximate value derived from time-domain simulations with $a = 160$ grid points using Eq. 3.5 (circular symbols).

[46]

$$\epsilon(\omega) = \varepsilon_\infty \left(1 + \frac{\omega_L^2 - \omega_T^2}{\omega_T^2 - \omega^2 - i\omega\gamma}\right), \tag{3.1}$$

where the magnitude of the losses is characterized by the width γ of the absorption peak in the imaginary part of ε. Previous considerations of the effects of losses in a PPC have been limited. Sigalas *et al.* implemented Eq. 3.1 in transmission calculations to determine the photonic bandgaps in a PPC [84]. However, these simulations relied on a stepwise approximation to the dielectric function that disrupts the location of the flat bands near ω_T, which we have previously shown are sensitive to the rapid changes in dielectric function [35, 36]. Several authors have also investigated the relationship between spatial and temporal decay in dissipative systems [48, 64].

The states of a periodic system where $\varepsilon(\mathbf{r})$ is complex are in general Bloch states with complex k and ω. Two subspaces of the total set of solutions are $\Phi_\omega = \{(k, \omega) : \omega \in \Re\}$ and $\Phi_k = \{(k, \omega) : k \in \Re\}$. The states with real frequency (Φ_ω) are accessible computationally using frequency-domain methods, such as the vectorial eigenmode expansion technique described in Sec. 3.1, while the states with real wave vector (Φ_k) can be obtained using a frequency-dependent time-domain method, which we introduce in Sec. 3.2. These two methods solve fundamentally different problems. If the frequency is assumed to be real, the resulting wave decays in space, while the time-domain approach studies a real-wave vector excitation that decays away in time. The solutions are identical only when ε is real. Throughout the remainder of this work, we will refer to the results of frequency-domain simulations as real-ω states/band structures and the results of time-domain simulations as real-k states/band structures. However, it is important to note that frequency-domain methods can compute states with complex ω as well.

In Sec. 3.3, we show that under certain conditions, the imaginary component of the wave vector of a real-ω state is related to the imaginary frequency component of a real-k state through a factor of the group velocity. In Sec. 3.4, we analytically solve for real-ω and real-k states of a one-dimensional polaritonic photonic crystal. We compare the band structure diagrams generated by the two methods, whose axes

are Re[k] and Re[ω]. The real-k states sufficiently removed from ω_T have frequencies whose real parts are relatively unperturbed from the corresponding states of a lossless crystal, and the real-ω states that have wave vectors whose real parts are not close to the edge of the Brillouin zone closely agree with the position of the real-k states on the band structure diagram. We find that these subsets of Φ_ω and Φ_k provide an ideal example of the aforementioned correspondence between the imaginary components of frequency and wave vector. However, the real-ω and real-k states with Re[k] near the edge of the Brillouin zone reveal few similarities, which can be attributed to the small group velocity at the band edges of the lossless crystal.

In Sec. 3.5, we find that the difference between the real ω and real k states in the band structure of a two-dimensional PPC is much more striking. As in the 1D crystal, the real-k band structure is qualitatively similar to the lossless crystal, which we have previously discovered exhibits the node switching and flux expulsion phenomena in the TE polarized bands for the given geometry [35]. As the width of the absorption loss peak increases, the real-ω bands begin to resemble the lowest band of the metallodielectric crystal that is obtained by replacing the polariton rod with a perfect metal. This is manifested by a folding back of the bands before they reach the Brillouin zone edge. This feature again occurs in frequency regimes associated with low group velocity in the lossless crystal.

Finally, in section 3.6, we analyze the reflection and transmission of a plane-wave off of a slab consisting of 5 periods of the 2D PPC structure studied in Sec. 3.5. We find that such a source will excite real-ω states which exhibit the node switching and flux expulsion phenomena at relevant levels of loss, but the localization of the field is lower than for the corresponding real-k states. The reflection/transmission measurements in a computational experiment using the time-domain method agree with those using the frequency-domain method, as expected since the source excitation is the same in each. The reflectivity spectrum reveals the presence of *pseudogaps*: frequency ranges where the transmission drops but the reflectivity remains much less than 1. We attribute these features to the high loss states in the real-ω band structure that exist in the intervals representing the band gaps of the real-k band structure.

3.1 Frequency-domain method

Our previous studies of PPC band structures utilized a computational technique based on the vectorial eigenmode expansion [36, 6, 35]. This generic frequency-domain photonic simulation tool CAMFR (Refs. [6] and [44]) can efficiently and accurately compute the Bloch states of a system with frequency-dependent dielectrics by dividing the unit cell into layers where the index profile does not change in the propagation direction. In each of these layers, we expand the field in the local eigenmodes of that particular layer. The only approximation is the size of the eigenmode basis, which we have determined to be well converged at 40.

Using mode matching, we derive frequency-dependent reflection and transmission matrices that completely describe the scattering behavior of the unit cell:

$$\mathbf{F}_2 = \mathbf{T}_{12} \cdot \mathbf{F}_1 + \mathbf{R}_{21} \cdot \mathbf{B}_2 \tag{3.2}$$

$$\mathbf{B}_1 = \mathbf{R}_{12} \cdot \mathbf{F}_1 + \mathbf{T}_{21} \cdot \mathbf{B}_2 \tag{3.3}$$

Here, $\mathbf{F}$ and $\mathbf{B}$ are column vectors containing the expansion coefficients of the forward and backward propagating fields, respectively. We then impose Bloch boundary conditions, and recast Eqs. 3.2 and 3.3 as a generalized eigenvalue problem, which can be solved for each frequency:

$$\begin{bmatrix} \mathbf{T}_{12} & \mathbf{R}_{21} \\ 0 & \mathbf{I} \end{bmatrix} \begin{bmatrix} \mathbf{F}_1 \\ q\mathbf{B}_1 \end{bmatrix} = q \begin{bmatrix} \mathbf{I} & 0 \\ \mathbf{R}_{12} & \mathbf{T}_{21} \end{bmatrix} \begin{bmatrix} \mathbf{F}_1 \\ q\mathbf{B}_1 \end{bmatrix},$$

where $\mathbf{I}$ is the unit matrix and $q = e^{-ika}$. Since the independent variable in these simulations is frequency, it is trivial to account for any frequency-dependent dielectric response.

3.2 Time-domain method

In a periodic time-domain approach, we solve the time-dependent Maxwell equations:

$$\nabla \times \mathbf{E} = -\mu \frac{\partial \mathbf{H}}{\partial t}, \; \nabla \times \mathbf{H} = \varepsilon_\infty \frac{\partial \mathbf{E}}{\partial t} + \frac{\partial \mathbf{P}}{\partial t}$$

where the electric polarization density $\mathbf{P}$ describes a forced oscillation at the phonon frequency ω_T with damping γ: [40, 50]

$$\frac{d^2\mathbf{P}}{dt^2} + \gamma \frac{d\mathbf{P}}{dt} + \omega_T^2 \mathbf{P} = \varepsilon_\infty \left(\omega_L^2 - \omega_T^2\right) \mathbf{E}. \tag{3.4}$$

Assuming a harmonic time dependence $\sim e^{-i\omega t}$ for both $\mathbf{E}$ and $\mathbf{P}$, Eq. 3.4 results in an effective dielectric function $\varepsilon = \varepsilon_1 + i\varepsilon_2$ that matches precisely with Eq. 3.1:

$$\begin{aligned} \varepsilon_1 &= \varepsilon_\infty \left[1 + \frac{\left(\omega_L^2 - \omega_T^2\right)\left(\omega_T^2 - \omega^2\right)}{\left(\omega_T^2 - \omega^2\right)^2 + \omega^2\gamma^2}\right], \\ \varepsilon_2 &= \varepsilon_\infty \frac{\left(\omega_L^2 - \omega_T^2\right)\omega\gamma}{\left(\omega_T^2 - \omega^2\right)^2 + \omega^2\gamma^2}. \end{aligned}$$

A Bloch state is generated with real wave vector using a periodic source that produces a propagating wave which decays in time. We note that due to losses, it is necessary to perform several simulations, each with sources based around different center frequencies spread throughout the frequency range of interest in the band structure.

Given finite grid spacing, $\varepsilon(\omega) = n(\omega)^2$ can be derived from the electric fields at two points separated by a distance x_{12} using the relation

$$n(\omega) = \frac{i}{2\pi\omega x_{12}} \log \frac{E_2(\omega)}{E_1(\omega)}. \tag{3.5}$$

A comparison between the approximate results of Eq. 3.5 applied to a bulk real-k simulation with $a = 160$ grid points and the exact value from Eq. 3.1 used in real-ω simulations is given in Fig. 3-1.

3.3 Relationship between real ω and real k states

We now consider the general problem of comparing real-frequency and real-wave vector states in lossy systems. A general Bloch state is a solution to the master equation $f(k,\omega) = 0$ of the form $(k_1 + ik_2, \omega_1 + i\omega_2)$. Consider a point (k_0, ω_0) with $k_0, \omega_0 \in \Re$. Then,

$$f(k,\omega) = f(k_0,\omega_0) + (k-k_0)\left.\frac{\partial f}{\partial k}\right|_{k_0,\omega_0} + (\omega-\omega_0)\left.\frac{\partial f}{\partial \omega}\right|_{k_0,\omega_0} + \mathcal{O}_2\left[(k-k_0),(\omega-\omega_0)\right], \tag{3.6}$$

where $\mathcal{O}_2(x,y)$ refers to terms of second-order in x and/or y. Assuming they exist, we consider two solutions of the master equation, $(k_0, \omega_0 + \Delta\omega_1 + i\Delta\omega_2)$ and $(k_0 + \Delta k_1 + i\Delta k_2, \omega_0)$, with $\Delta\omega_{1,2}, \Delta k_{1,2} \in \Re$. Ignoring second order terms in Eq. 3.6,

$$\begin{aligned} -f(k_0,\omega_0) &= (\Delta k_1 + i\Delta k_2)\left.\frac{\partial f}{\partial k}\right|_{k_0,\omega_0}, \\ -f(k_0,\omega_0) &= (\Delta\omega_1 + i\Delta\omega_2)\left.\frac{\partial f}{\partial \omega}\right|_{k_0,\omega_0}. \end{aligned}$$

Therefore,

$$\left.\frac{\partial\omega}{\partial k}\right|_{k_0,\omega_0} \equiv \left.\frac{\partial f}{\partial k}\middle/\frac{\partial f}{\partial\omega}\right|_{k_0,\omega_0} = \frac{\Delta\omega_1 + i\Delta\omega_2}{\Delta k_1 + i\Delta k_2}. \tag{3.7}$$

Eq. 3.7 states that if the real-ω and real-k band structures coincide at a particular $(k_0,\omega_0) \in \Re$ $(\Delta\omega_1, \Delta k_1 \approx 0)$, then the imaginary components Δk_2 and $\Delta\omega_2$ are related by a factor of the group velocity:

$$\Delta\omega_2 = \Delta k_2 \left.\frac{\partial\omega}{\partial k}\right|_{k_0,\omega_0} \equiv \Delta k_2 v_g. \tag{3.8}$$

This also demonstrates that the group velocity as defined by Eq. 3.7 is purely real at (k_0,ω_0) in this system. We note that this argument implicitly assumes that losses are small $(n_2 \ll n_1)$ so that the perturbations to k and ω are small compared with (k_0,ω_0). These results are independent of the dimensionality of the photonic crystal; however, the validity of Eq. 3.8 ultimately rests on the applicability of the assumption $\Delta\omega_1 = \Delta k_1 = 0$. The factor of v_g can be understood by comparing the nature of

the real-k and real-ω states. A real-k state has fields with no spatial decay and is unaffected by the group velocity, unlike real-ω states with complex k that decay spatially and hence will be affected more strongly by the lossy polariton material when v_g is small.

Previous work [64, 48] has argued that the relationship in Eq. 3.8 holds for small losses. In particular, Krohkin and Halevi (KH) follow a similar analysis using Taylor expansion of the master equation, but with less generality. In order to arrive at Eq. 3.8, KH implicitly assume that a pair of Bloch states exists with $\Delta\omega_1 = \Delta k_1 = 0$. In the following section, we will demonstrate that in a 1D PPC, this condition holds for the lowest few bands, except very close to the band edges.

However, in a bulk system where $k = n\omega/c$, it is easy to show that Eq. 3.8 *does not* hold, even for small losses. A solution of the form $(k_0 + i\Delta k_2, \omega_0)$ satisfies $k_0 = n_1\omega_0/c$ and $\Delta k_2 = n_2\omega_0/c$. Therefore,

$$\Delta k_2 = k_0 \frac{n_2(\omega_0)}{n_1(\omega_0)}. \tag{3.9}$$

The only solution of the form $(k_0, \omega_0 + \Delta\omega_1 + i\Delta\omega_2)$ is

$$\Delta\omega_1 = -\left.\frac{ck_0}{n_1}\right|_{\omega_0} + ck_0 \left.\frac{n_1}{n_1^2 + n_2^2}\right|_{\omega_0+\Delta\omega_1+i\Delta\omega_2} \tag{3.10}$$

$$\Delta\omega_2 = -ck_0 \left.\frac{n_2}{n_1^2 + n_2^2}\right|_{\omega_0+\Delta\omega_1+i\Delta\omega_2}. \tag{3.11}$$

If we can assume that $n(\omega_0) \approx n(\omega_0 + \Delta\omega_1 + i\Delta\omega_2)$ (as would be the case, e.g. in a frequency-independent dielectric material) we can combine Eqs. 3.9 and 3.11:

$$\Delta\omega_2 = -c\Delta k_2 \frac{n_1}{n_1^2 + n_2^2} = \Delta k_2 \mathrm{Re}\left[\frac{\partial\omega}{\partial k}\right], \tag{3.12}$$

since $\partial\omega/\partial k = c/n$. This result holds even for large Δk_2 and $\Delta\omega_2$. We see that because $\Delta\omega_1$ in Eq. 3.10 is no longer zero, it is only the real part of the group velocity which transforms between Δk_2 and $\Delta\omega_2$. We note that this conclusion comes from the natural pairing of states with the same real wave vector component and comparing

the shift in frequency. A similar analysis assuming $\Delta\omega_1 = 0$ produces

$$\Delta\omega_2 = c\Delta k_2/n_1. \tag{3.13}$$

The difference between Eqs. 3.12 and 3.13 stems from the fact that when it is impossible to simultaneously choose $\Delta k_1 = 0$ and $\Delta\omega_1 = 0$, there is no logical pairing of real-k and real-ω states for which to apply Eq. 3.8. We will present a more striking example of this situation in a 2D PPC in Sec. 3.5.

3.4 1D crystals

The one-dimensional PPC problem is useful because it is analytically solvable. We consider a system of air and $LiTaO_3$, a material with a large polariton gap from $\omega_T = 26.7$ THz to $\omega_L = 46.9$ THz, $\varepsilon_\infty = 13.4$, and $\gamma = 0.94$ THz. We set $a = 4.5\mu$m so that $\omega_T = 0.4(2\pi c/a)$, $\omega_L = 0.703(2\pi c/a)$, and $\gamma = 0.014(2\pi c/a)$. The slabs have width $d_1 = d_2 = a/2$. The Bloch states are given by solutions of

$$\cos(ka) = \cos\left(\frac{\omega d_1}{c}\right)\cos\left(\frac{n(\omega)\omega d_2}{c}\right) - \frac{1+n(\omega)^2}{2n(\omega)}\sin\left(\frac{\omega d_1}{c}\right)\sin\left(\frac{n(\omega)\omega d_2}{c}\right), \tag{3.14}$$

which is solvable through inversion for k if ω is given and through Newton's method for ω if k is given. We note that although Eq. 3.14 is generally referred to in the context of a frequency-domain problem, it is in fact a general solution to the arbitrary 1D Bloch boundary value problem for a plane wave with complex k and/or ω. We plot the real component of the solutions assuming either real frequency or real wave vector in Fig. 3-2(a). To stress the low "group velocity" of the higher bands, the inverse $1/\tilde{v}_g = (d\omega/d\mathrm{Re}[k])^{-1}$ obtained from the real-ω solutions is shown in Fig. 3-2(b). Near the band edges, the two methods produce differing results. When k is real, there are gaps where no Bloch solution exists whose frequency has a real component within these frequency ranges. However, the band structure for real ω is a continuous line, with a solution lying somewhere within the Brillouin zone for all ω.

Nevertheless, the real-k and real-ω bands show excellent agreement in the middle

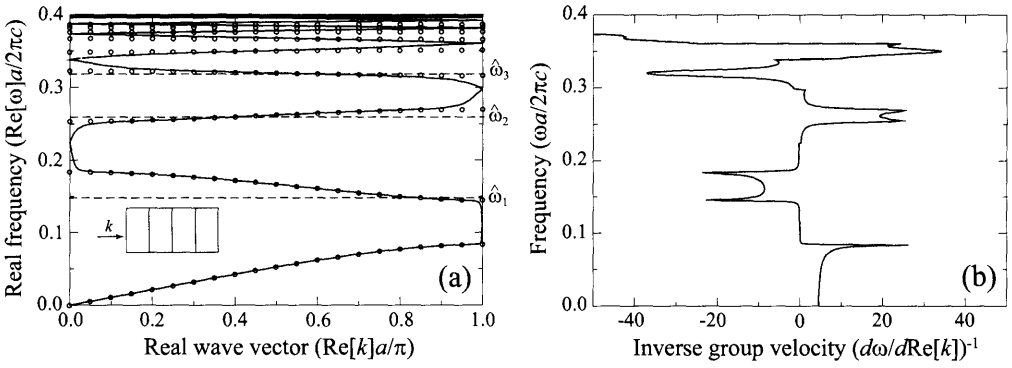

Figure 3-2: Lossy one-dimensional PPC structures: (a) Comparison of band structure calculations for the 1D lossy $LiTaO_3$ PPC shown in the inset using frequency-domain and time-domain approaches. The solid pink line is the real part of the wave vector solution assuming real frequency in equation 3.14, while the purple circular symbols are the real part of the frequency solution assuming real wave vector. Note the presence of frequency gaps only when k is purely real, and coincidence of the two methods in the middle of the Brillouin zone. (b) The inverse of the "group velocity" defined by $\tilde{v}_g^{-1} = (d\omega/d\mathrm{Re}[k])^{-1}$ as calculated from the real-ω simulation.

of the Brillouin zone. Therefore, we can choose states such that $\Delta\omega_1 \approx 0$ and $\Delta k_1 \approx 0$ simultaneously, and the coinciding states $(k_0 + i\Delta k_2, \omega_0)$ and $(k_0, \omega_0 + i\Delta\omega_2)$ should be related by a factor of the group velocity. In Fig. 3-3, we compare the values of $\mathrm{Im}[\omega]$ and $\mathrm{Im}[k]v_g$ as functions of $\mathrm{Re}[\omega]$. Equation 3.8 holds extremely well through the first few bands, showing disagreement only close to ω_T when the terms of second order in Δk_2 in Eq. 3.6 can no longer be ignored and the two band structures cease to coincide. As ω increases, the group velocity becomes much smaller than c, [36] and so the imaginary wave vector component from real-ω calculations is several orders of magnitude larger than the imaginary frequency component from real-k calculations.

As is the case for lossless crystals [36], the frequencies of the bands of the 1D PPC at the midpoint of the Brillouin zone show excellent agreement with the resonance frequencies given by solutions to

$$\hat{\omega}_j = j\pi c/dn_1(\hat{\omega}_j), \tag{3.15}$$

where d is the width of the polariton slab(rod). Note that unlike the lossless crystal,

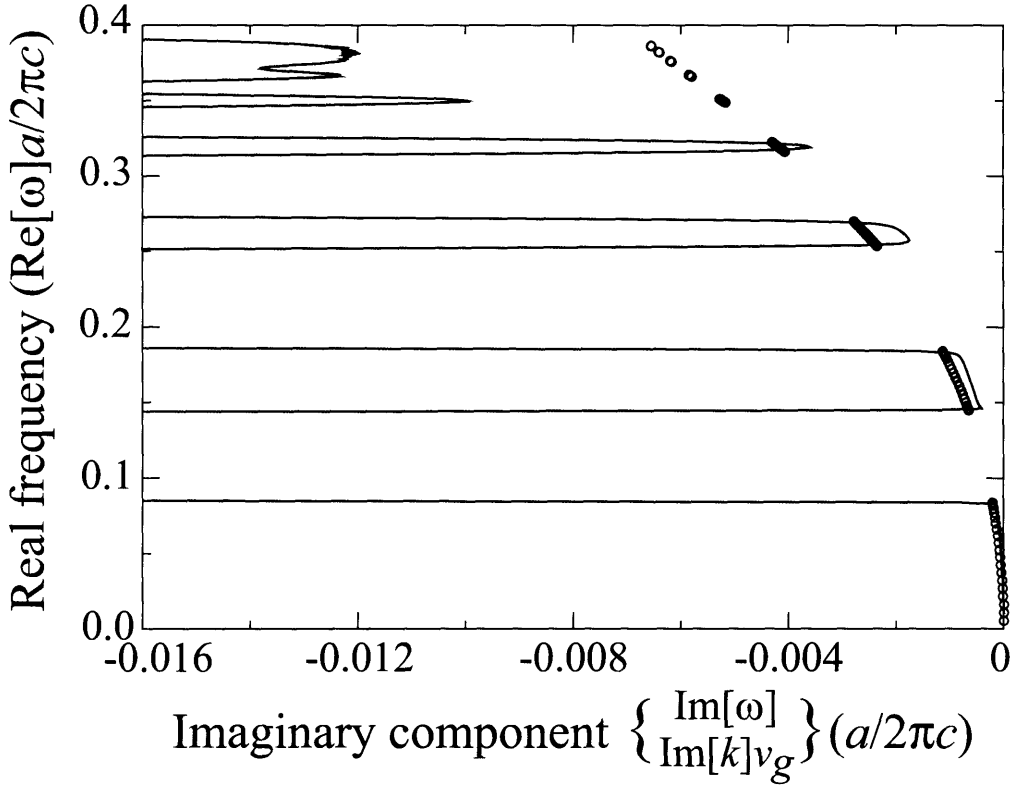

Figure 3-3: Comparison of the imaginary components of the band structure calculations in Fig. 3-2. In purple circular symbols is the imaginary part of the frequency when the wave vector is assumed to be real, while the pink line is the imaginary part of the wave vector when the frequency is assumed to be real, rescaled by the quantity $\tilde{v}_g$. Note the agreement in the first three bands, simultaneous with the coincidence of the band structure diagrams as described in Sec. 3.3.

m	$\omega(\pi/2a)$	$\hat{\omega}_j$	$\varepsilon(\hat{\omega}_j)$
1	0.1667	0.1478	45.81+0.4882i
2	0.2622	0.2564	60.84+1.817i
3	0.3194	0.3179	88.95+5.737i
4	0.3498	0.3498	130.4+15.31i
5	0.3664	0.3671	183.7+34.88i
6	0.3761	0.3775	247.8+71.21i
7	0.3822	0.3843	318.2+134.0i
8	0.3863	0.3893	386.5+242.2i
9	N/A	0.3943	408.5+484.5i

Table 3.1: Comparison of the band frequencies at $k = \pi/2a$ to $\hat{\omega}_j$ from equation 3.15 for a 1D PPC of $LiTaO_3$ slabs in air with $d_1 = d_2 = a/2$. In the last column is the value of ε at $\omega = \hat{\omega}_j$. The resonance at $\hat{\omega}_9$ does not have a corresponding band in the PPC.

there are only a finite number of solutions to Eq. 3.15 with real ω since $\varepsilon(\omega)$ no longer blows up at ω_T. We list these frequencies, as well as the value of the dielectric function at $\hat{\omega}_j$, in Table 3.1.

3.5 2D crystals

We can apply the insights from Secs. 3.3 and 3.4 to the band structures of a two-dimensional polaritonic photonic crystal, computed using either the frequency-domain or time-domain method. We consider a 2D photonic crystal of square rods in air with sides of length s ($s/a = 0.25$) in a square lattice. The rods are taken to be $LiTaO_3$, with $a = 4.5\mu$m so that $\omega_T = 0.4(2\pi c/a)$, $\omega_L = 0.703(2\pi c/a)$ and $\gamma = 0.014(2\pi c/a)$.

In Fig. 3-4, we plot the band structure from Γ-X-M-Γ computed using the time-domain method from Sec. 3.2. We overlay with dashed lines the band structure for the metallodielectric crystal obtained by replacing $LiTaO_3$ with a perfect metal. Similar to a lossless crystal [35, 36], both the TE and TM bands are relatively flat in most frequency regions below ω_T, where they resemble rod-localized resonance modes. We again note the finite number of bands, related to the finite maximum in ε introduced by the absorption peak. The TE bands also display an anticrossing interaction related to the existence of Bloch states of the geometrically equivalent

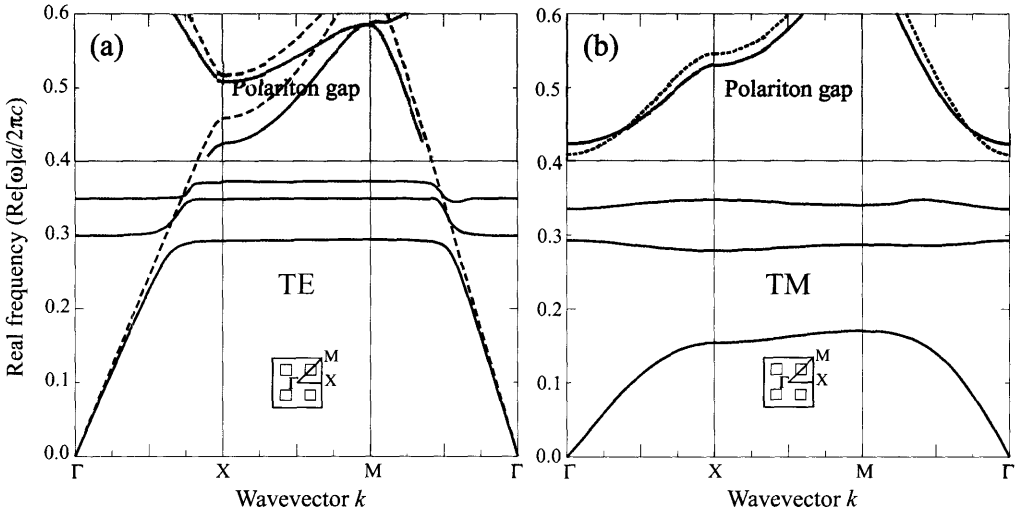

Figure 3-4: Band structure of a square 2D PPC of square $LiTaO_3$ rods in air with sides of length $s/a = 0.25$, $\omega_T = 0.4(2\pi c/a)$, $\omega_L = 0.703(2\pi c/a)$, $\varepsilon_\infty = 13.4$ and $\gamma = 0.014(2\pi c/a)$ along the edge of the irreducible Brillouin zone from Γ to X to M to Γ, calculated using frequency-dependent time-domain simulations. The TE (**H** out-of-plane) bands are in red in (a), TM (**E** out-of-plane) in blue in (b). At distances greater than γ away from ω_T, this band structure shows little difference qualitatively from that of the crystal of lossless polaritonic material ($\gamma = 0$) [35]. The TE(TM) bands of a metallodielectric crystal obtained by replacing $LiTaO_3$ by a perfect metal are given by the red(blue) dashed lines.

metallodielectric crystal. There is very little perturbation from the band structure of the lossless crystal for the bands shown. This is because the frequency is always many factors of γ away from ω_T, where $\varepsilon_2 \ll \varepsilon_1$. In this regime, the shape of $\varepsilon_1(\omega)$, and hence the spatial modulation of the Bloch state, are virtually unchanged.

Like the lossless crystal, PPC states of TE polarization exist with real component of frequency both below and above ω_T, even at frequencies very close to ω_T. This allows for the realization of the node switching phenomenon through a variety of field profiles and the flux expulsion phenomenon over a frequency range down to a few γ. We note that as the dielectric function makes a rapid transition from high-index to metallic around ω_T, the TE band inside the polariton gap appears discontinuously as in the lossless crystal [36]. In addition, for frequencies within $\sim \gamma$ of ω_T, the polariton material is too lossy to observe any states on the same time scales that were used to

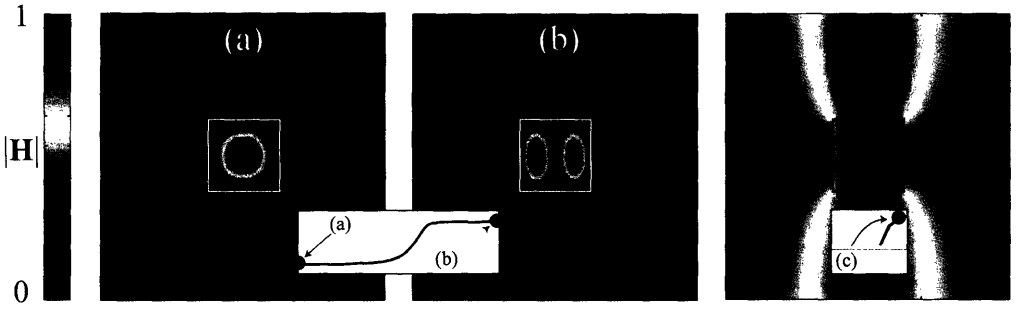

Figure 3-5: Magnetic field profiles ($|\mathbf{H}|$) of the TE-polarized states at three representative points on the band structure diagram in Fig. 3-4. (a) ($\omega = 0.3(2\pi c/a)$, $k = \Gamma$) and (b) ($\omega = 0.355(2\pi c/a)$, $k = \mathrm{X}$) show the field localization at the band edges of the second band. (c) ($\omega = 0.44(2\pi c/a)$, $k = 0.475(2\pi/a)$) shows the metallic profile above ω_T.

generate the rest of the band structure diagram. The two experimental phenomena that were previously introduced in a lossless crystal [35] can easily be realized in the lossy crystal. In Fig. 3-5(a-b), we demonstrate node switching through the high localization of the fields at the edges of the second TE-polarized band, which connects the $\mathrm{TE}_{1,1}$ rod-localized state to the $\mathrm{TE}_{1,2}$ state. In Fig. 3-5(c), we verify the existence of states above ω_T by showing a state with fields that are essentially expelled from the polaritonic region.

We found in Sec. 3.4 that the real-ω band structure of the 1D PPC differed from the real-k band structure near the band edges, where the group velocity is smallest. An additional feature is introduced in two-dimensional PPCs that further distinguishes the real-ω and real-k states in the regions of low group velocity. The existence of a lossless band ($\mathrm{Im}[k] = 0$) in the metallodielectric crystal in the frequency range below ω_T introduces the possibility that light can choose to circumvent the lossy polariton rods and concentrate flux in the ambient region. The PPC reveals precisely this tendency in the real-ω band structure in Fig. 3-6, where we plot the TE-polarized state at each real frequency with the lowest imaginary wave vector component for the same crystal structure used in Fig. 3-4. We vary the absorption peak width γ between $0.0001(2\pi c/a)$ and $0.01(2\pi c/a)$ and concentrate on the locations of the first three photonic band gaps in the real-k band structure. The bands are obtained by

selecting the Bloch wave vector at each frequency with the smallest absolute value of $\mathrm{Im}[k]$.

As γ increases to $\sim 0.01(2\pi c/a)$, the band structure takes on a strikingly different character. In particular, the anticrossing interaction with the localized rod states that produced the flat band regions in the lossless crystal becomes greatly reduced, and the bands fold back and connect within the regions marked in purple shading that correspond to the bandgaps of the real-k simulations. This surprising band back-bending, with two superluminal points of infinite group velocity in each band gap, has also been observed in constant dielectric simulations with complex ϵ [63] and at surface plasmon resonances [2]. The superluminal behavior can be attributed to the remnants of the photonic band gaps [89], and is found only in frequency ranges where the imaginary component of the wave vector is prohibitively large. In the context of Sec. 3.3, it is clear that in a 2D crystal the assumption of the existence of states with $\Delta k_1, \Delta\omega_1 \approx 0$ and $\Delta k_2, \Delta\omega_2$ small breaks down entirely, and Eq. 3.8 is no longer relevant. We expect that if corresponding states around $k = \Gamma$ and $k = \mathrm{X}$ with real frequency were to exist in the real-ω band structure, they would exhibit prohibitively high losses, due to the low group velocity of the corresponding bands of the lossless crystal near the resonance frequencies.

We have also marked the locations of the rod resonance frequencies $\hat{\omega}_{11} = 0.311(2\pi c/a)$, $\hat{\omega}_{21} = 0.359(2\pi c/a)$, and $\hat{\omega}_{31} = 0.380(2\pi c/a)$ solving $\hat{\omega}_{ij} = \sqrt{i^2 + j^2}\pi c/sn_1$, which all lie within the band gap regions ($\hat{\omega}_{22} = 0.374(2\pi c/a)$ does not interact with the metallodielectric band due to symmetry considerations [36]). The only other resonance mode of this system with real frequency is $\hat{\omega}_{32} = 0.386(2\pi c/a)$.

We associate the features of the $\gamma \sim 0.01(2\pi c/a)$ real-ω band structure with the tendency of the light to prefer the metallodielectric configuration with the flux predominantly expelled from the polariton region. We find a different situation entirely when studying the TM-polarized bands of the $LiTaO_3$ crystal. Because ω_T is below the lower edge of the fundamental TM band gap of the metallodielectric crystal, the bands plotted in Fig. 3-7 with $\gamma = 0.014(2\pi c/a)$ appear similar qualitatively to those of the 1D crystal since the metallodielectric bands play no role.

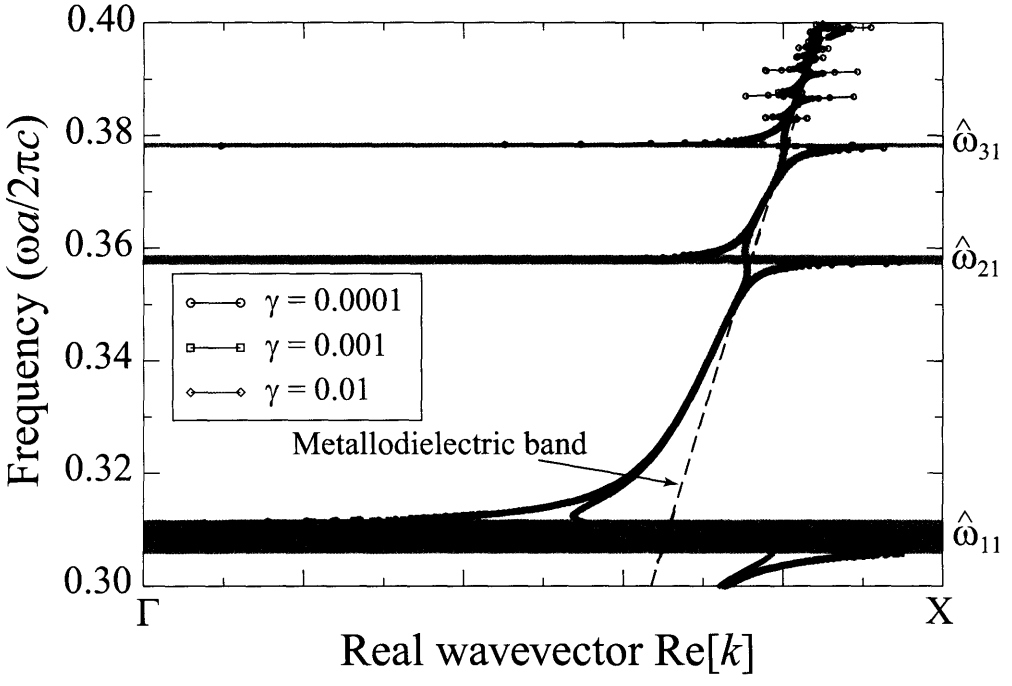

Figure 3-6: Band structure from Γ to X of the same crystal as in Fig. 3-4 calculated using real-ω simulations, with the loss parameter γ varied from $0.0001(2\pi c/a)$ to $0.01(2\pi c/a)$. As γ increases to $0.01(2\pi c/a)$, the first bands clearly fail to extend to the edges of the Brillouin zone. Instead, the band structure begins to mimic the lowest TE-polarized metallodielectric band, shown as a dashed solid line. The imaginary component of wave vector (not shown) increases sharply in the gaplike regions marked in purple.

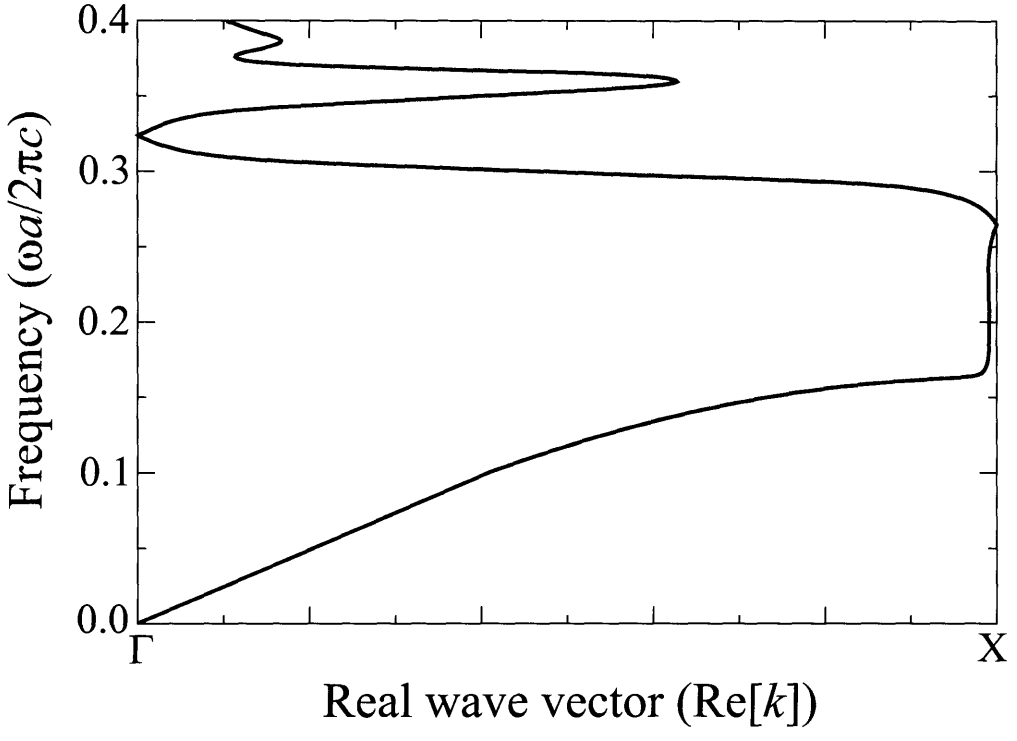

Figure 3-7: TM bands of the 2D $LiTaO_3$ crystal with $\gamma = 0.014(2\pi c/a)$ from a real-ω simulation. Note the similarities in appearance of the first few bands to the bands of the 1D PPC in Fig. 3-2(a). The bands are flat, except near the band edges. Moreover, despite the fact that the bands extend from $k = \Gamma$ to $k = \mathrm{X}$, there are no band gaps.

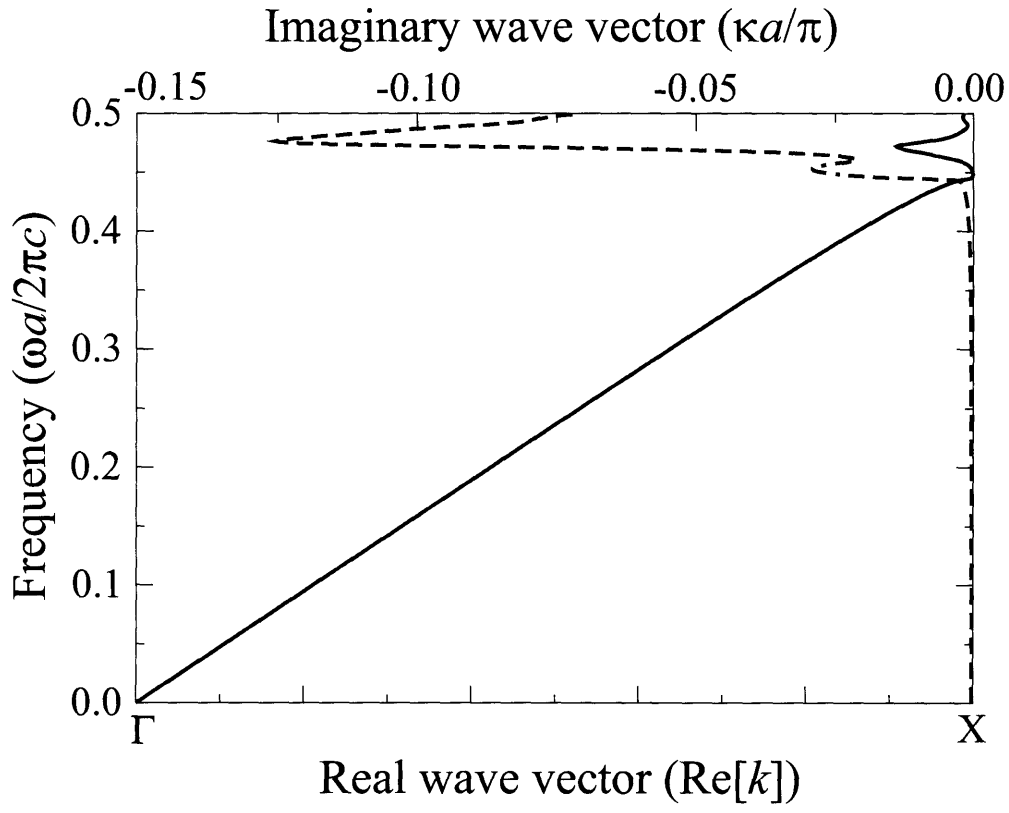

Figure 3-8: Real (solid) and imaginary (dashed) wave vector components from a real-ω simulation of the TE bands of a crystal of square SiC rods with $s/a = 0.25$, $\varepsilon_\infty = 6.7$, $\omega_T = 0.5(2\pi c/a)$, $\omega_L = 0.6(2\pi c/a)$ and $\gamma = 0.01(2\pi c/a)$. Note that the modes remain close to the edge of the Brillouin zone at frequencies near ω_T, unlike the lossless crystal which has flat bands extending from Γ to X.

As further evidence of the influence of the metallodielectric crystal states, we can shift the resonance frequencies into the TE band gap of the metallodielectric crystal by shifting ω_T through a change in a. In Fig. 3-8, we plot the TE bands of a 2D PPC of SiC rods with $s/a = 0.25$, $\varepsilon = 6.7$, $\omega_T = 0.5(2\pi c/a)$, $\omega_L = 0.6(2\pi c/a)$ and $\gamma = 0.01(2\pi c/a)$ (a purely speculative amount of loss for this material). The lowest resonance frequency $\hat{\omega}_{11}$ is now inside the band gap of the metallodielectric crystal (cf. Fig. 3-4(a)). Due to the lack of an anticrossing interaction, the bands of the lossless crystal are very flat in the middle of the Brillouin zone. It is now modes with real component of k away from the edges of the Brillouin zone that would have prohibitively large imaginary component due to the low group velocity in the lossless crystal near these frequencies. The result is that instead of the flat band near $\omega = 0.473(2\pi c/a)$ that extends from Γ to X in the lossless crystal, the states with lowest loss occur only near the wave vector $k = \mathrm{X}$. This effect can also be observed in the behavior of the TM states near ω_T in Fig. 3-7, which are clustered around $k = \Gamma$.

3.6 Relevance to experimental measurements

The question of experimental accessibility arises for the two classes of states discussed above. A previous experiment using the coherent microwave transient spectroscopy (COMITS) technique excited particular Bloch states of a 2D crystal using a plane wave source [75]. Since the frequency is conserved in the transmission of a plane wave through a slab structure, we expect that only the real-ω states will be excited in this type of experiment if it involves a system with losses.

To simulate the results of a COMITS experiment which probes the node switching and field expulsion phenomena, we use CAMFR to examine the field profile of the real-ω mode excited in a slab of five periods of the $LiTaO_3$ crystal structure from Sec. 3.5 by a plane wave at frequencies similar to those studied in Fig. 3-5. At frequencies below ω_T, we expect that relatively few periods are necessary to generate the highly localized states of the system near the resonance frequencies. In Fig. 3-9(a-b), we demonstrate node switching at frequencies near the $\mathrm{TE}_{1,1}$ and $\mathrm{TE}_{1,2}$ resonances using

two different values of γ: $\gamma_1 = 0.001(2\pi c/a)$ and $\gamma_2 = 0.014(2\pi c/a)$. We compare the actual level of loss (γ_2) to a smaller value γ_1 in order to study the intermediate changes in the fields between a physical $LiTaO_3$ crystal with losses and the lossless crystals previously examined [35]. As γ increases, the rod localization of the field clearly decreases as the frequency approaches ω_T and the field configuration becomes more metallic. In Fig. 3-9(c), we demonstrate flux expulsion from the polariton rod using an incident wave with $\omega > \omega_T$. The states of the infinite crystal at the frequencies of interest are identified on a band structure in Fig. 3-9(d). Above ω_T, the band structure is virtually unaffected by the amount of loss, since most of the field is removed from the polariton region.

In order to observe the propagating states with real wave vector that are generated in a real-k band structure calculation, it may be necessary to mimic the periodic source conditions of our simulations. This could be possible by coupling to a state in Φ_k through a grating on the surface of the photonic crystal. These states decay relatively slowly, even near the band edges where the full-width at half maximum is at most 50% greater than the states in the middle of the Brillouin zone. If these modes can be excited, the node switching and flux expulsion phenomena can be observed at higher levels of loss with more field localization than is possible using real-ω states.

We mention that the frequency regimes without states in the real-k band structure are not true band gaps, because they lack the high reflectivity characteristic of a lossless photonic band gap [84]. In fact, any crystal with absorptive materials cannot produce the perfect interference of reflected waves through Bragg scattering that is considered to produce a normal gap in a lossless crystal. In Fig. 3-10, we compare the reflection and transmission of a plane wave off of the same 5-layer slab structure studied in Fig. 3-9 at frequencies near the gap-like regions (*pseudogaps*) using both the time-domain and frequency-domain methods. As expected, they show good agreement since the simulations are reproducing the same computational experiment. From the perspective of the real-ω band structure, this drop in transmission without a correspondingly high reflectivity can be attributed to coupling to the high-loss real-ω states that exist within the pseudogap regions. Figure 3-10 demonstrates that the

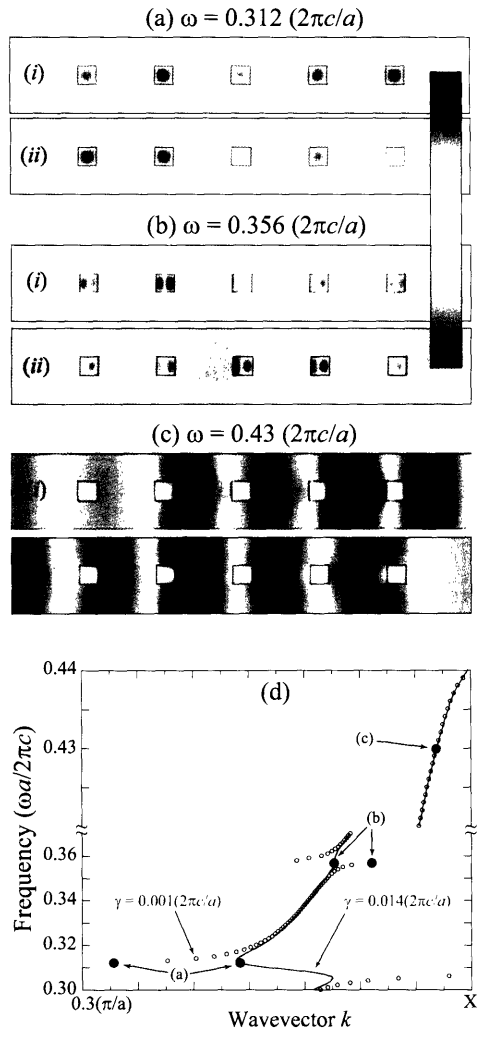

Figure 3-9: Magnetic field profiles ($|\mathbf{H}|$) of TE-polarized modes excited in a slab of 5 periods of a 2D $LiTaO_3$ crystal by a plane-wave for two different absorption peak widths: (i) $\gamma = 0.001(2\pi c/a)$ and (ii) $0.014(2\pi c/a)$. (a) $\omega = 0.312(2\pi c/a)$ and (b) $\omega = 0.356(2\pi c/a)$ show the field localized inside the rod at wave vectors near the edges of the Brillouin zone and represent the node switching phenomenon. Note that the rod localization of the fields for becomes steadily worse as γ increases due to the increasing preference for a metalliclike configuration. In (a)-(ii), the reduction in rod localization is very slight since ω is far away from ω_T; the change in field profile is due to the fact that the wave vector is shifted by $0.225\pi/a$. (c) The field profile at $\omega = 0.44(2\pi c/a)$ is highly metallic, and in combination with the states in (b) verifies the existence of the flux expulsion phenomenon. (d) The states of the infinite crystal corresponding to the modes in (a-c) identified on a real-ω band structure diagram by black dots.

maximum value of the reflectivity in the pseudogap regions clearly decreases as the frequency approaches the absorption peak at $\omega_T = 0.4$ and the magnitude of Im[k] within the pseudogaps increases.

3.7 Conclusion

In conclusion, we have extended our investigations of the novel optical phenomena in PPCs to lossy crystals, and presented a formalism for understanding the two classes of states, Φ_ω (real frequency) and Φ_k (real wave vector). In a 1D PPC, we have found that due to the coincidence of the real-ω and real-k band structures, the time decay represented by the imaginary frequency component of the real-k states is related to the spatial decay represented by the imaginary wave vector component of the real-ω state with the same real wave vector and frequency components through a factor of the group velocity.

However, as the width of the absorption peak increases, the real-ω band structure of a 2D PPC consisting of square $LiTaO_3$ rods diverges from the real-k band structure, which is relatively unperturbed from previous simulations for a lossless crystal [35], as the absorption peak width γ increases. Any states near the edges of the Brillouin zone could only exist with extremely high spatial decay rates, which we associate with the low group velocity. Instead, the states with lowest loss are are metalliclike with high localization in the surrounding ambient dielectric region, exhibited in the band structure by a folding of the bands before they reach Γ or X. As γ reaches the experimentally measured value for $LiTaO_3$, the entire real-ω band structure below ω_T closely resembles that of a metallodielectric crystal with the polariton rods replaced by a perfect metal.

Our analysis applies equally well to the broader class of periodic structures containing any lossy materials, not only polaritonic media. Ultimately, we conclude that both computational techniques used in this work provide accurate and efficient means to solve for two distinct classes of states. The variables which effect the similarities between these two sets extends beyond simply the absorption peak width γ,

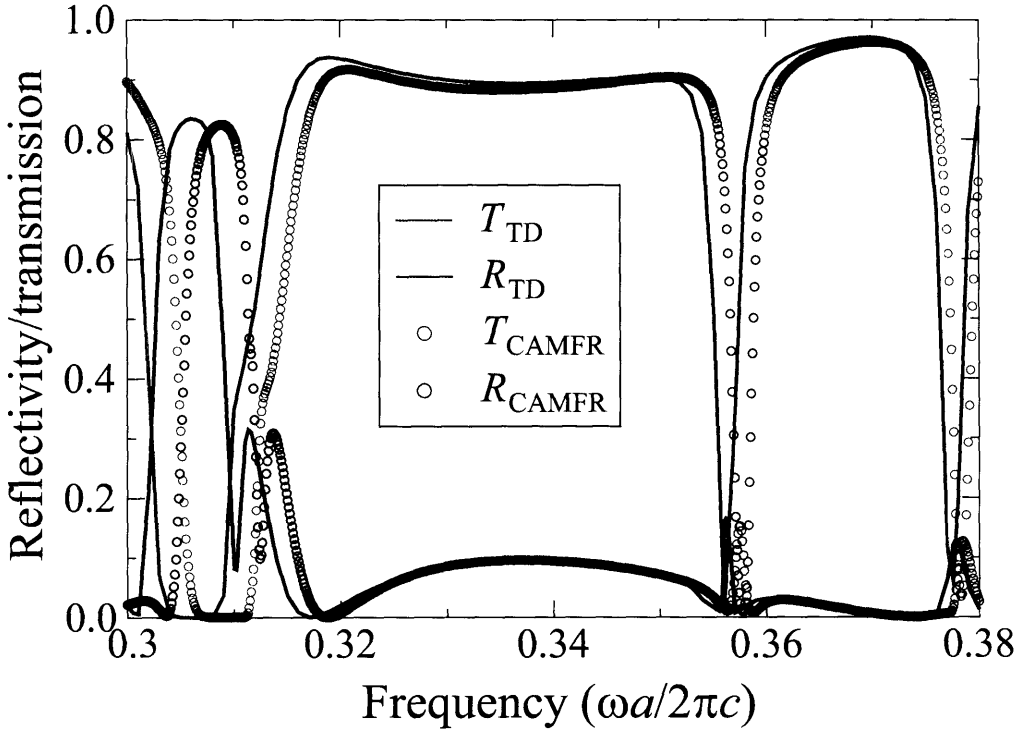

Figure 3-10: Reflectivity and transmission off five layers of a 2D square PPC of square $LiTaO_3$ rods with $\gamma = 0.001(2\pi c/a)$. The reflectivity is shown in red, the transmission in green. Real-ω simulations with 40 eigenmodes are shown with circular symbols, real-k simulations with $a = 160$ grid points are shown with solid lines. Note the pseudogap regions near the center frequencies of $0.309(2\pi c/a)$ and $0.357(2\pi c/a)$, where the transmission shows a marked decrease. The reflectivity in these frequency ranges is much lower than 1, and in fact displays no noticeable features near the second pseudogap for $\gamma = 0.014$ (not shown). The small shift ($\sim 0.5\%$) between the two data sets is due to the fact that the results of time-domain simulations converge from below as a function of the grid resolution, while the resuls of frequency-domain simulations converge from above as a function of the number of eigenmodes.

but rather also depends strongly on the geometry of the structure. In this light, the distinction between real-k and real-ω states must also be considered in experiments when attempting to reproduce theoretical predictions in lossy systems.

Chapter 4

Negative Effective Permeability in Polaritonic Photonic Crystals

Segments of this chapter will appear in the July 26, 2004 issue of Applied Physics Letters.

4.1 Introduction

Recent interest in metamaterials, periodic structures of conducting elements with bulk effective electromagnetic scattering properties, has been fueled by the demonstration of a split-ring resonator (SRR) composite with negative effective magnetic permeability (μ) [66]. In combination with an array of metallic wires with negative effective permittivity ε_{eff} [67], a system with negative μ_{eff} behaves as a left-handed material with negative refractive index [86, 88], resulting in several reversed electromagnetic-wave properties [95] including negative refraction [79].

An alternate approach to constructing metamaterials is to use dielectric elements: O'Brien and Pendry [63] have shown that a 2D square photonic crystal of circular ferroelectric rods have a resonance in μ_{eff} in the millimeter wavelength range where ε is extremely large ($\sim 200 + 5i$). It is of interest to identify other materials with high linear response characteristics that could produce the same magnetic resonance effect in other wavelength ranges. We will demonstrate that a negative effective

permeability can be obtained in a large wavelength range of 2μm to $\sim$ 100μm in a simple 2D photonic crystal system using a variety of common phonon-polariton materials.

4.2 Effective indices in metamaterials

The system we will consider is shown in Fig. 4-1. We approximate a semi-infinite slab with 2^{10} periods of a photonic crystal structure with square polariton rods of side length s and a lattice constant a, terminated on either side by air. We have chosen square rather than circular rods to simplify fabrication. Using the frequency-domain vectorial eigenmode expansion code CAMFR [6], we calculate the reflected field $\mathbf{E}_r$ in the air region for a given incident field $\mathbf{E}_i$ at the boundary defined by the plane at a distance $a/2$ from the center of the first column of rods. The ratio of $\mathbf{E}_r$ to $\mathbf{E}_i$ at the boundary may be thought of as the reflectivity from a bulk effective medium with permittivity ε_{eff} and permeability μ_{eff}. The effective indices of this medium can be determined from the complex reflectivity r using [63]

$$Z_{\text{eff}} = \frac{1+r}{1-r},\ \varepsilon_{\text{eff}} = \frac{n_{\text{eff}}}{Z_{\text{eff}}},\ \mu_{\text{eff}} = n_{\text{eff}} Z_{\text{eff}}, \tag{4.1}$$

where $n_{\text{eff}} = ck/\omega(k)$ is determined from the complex band structure.

A simple model for the dielectric function of a polaritonic material with losses is [46]

$$\varepsilon(\omega) = \varepsilon_1 + i\varepsilon_2 = \varepsilon_\infty \left(1 + \frac{\omega_L^2 - \omega_T^2}{\omega_T^2 - \omega^2 - i\omega\gamma}\right), \tag{4.2}$$

where the magnitude of dissipation is characterized by the width γ of the absorption peak in the imaginary part of ε. The real part of the index of refraction $n = \sqrt{\varepsilon(\omega)}$ can become large below ω_T, the location of the phonon resonance, leading to Mie resonances for sufficiently small γ [54, 35, 36, 37]. For $\gamma = 0$, the Mie resonances of a square polaritonic rod occur at [35, 36]

$$\hat{\omega}_{lm}^2 = \frac{1}{2}\left(\omega_L^2 + \Omega_{lm}^2 - \sqrt{(\omega_L^2 + \Omega_{lm}^2)^2 - 4\Omega_{lm}^2\omega_T^2}\right) \tag{4.3}$$

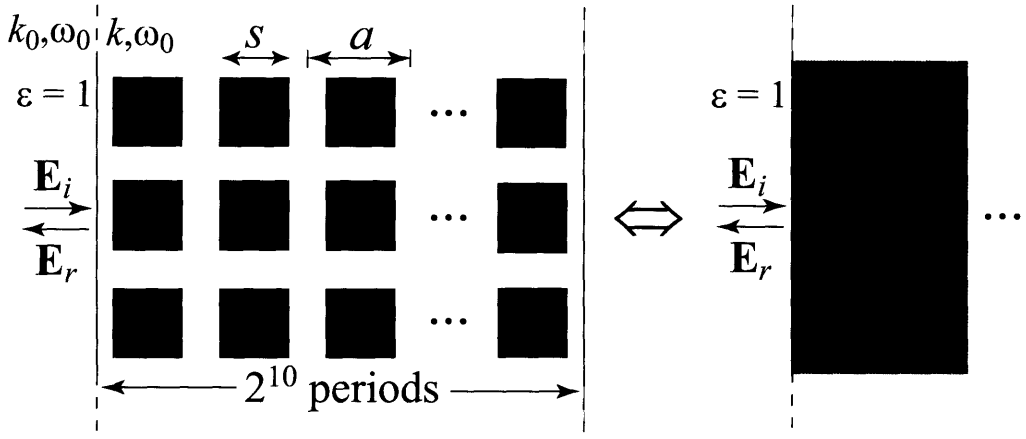

Figure 4-1: The reflected waves generated by a slab structure composed of 2^{10} layers of a two-dimensional square photonic crystal structure with square rods of a given polariton material may be thought of as coming from the interface with a bulk effective medium. The effective magnetic properties have $\mu_{\text{eff}} < 0$ in certain frequency regimes.

where $\Omega_{lm} = \pi c(l^2+m^2)^{1/2}/s\sqrt{\varepsilon_\infty}$. These localized modes couple to the bands derived from the metallodielectric (MD) crystal created by replacing the polariton material with a perfect metal. Whenever the Mie resonances lie outside the bandgaps of the MD crystal, a band shape that exhibits backbending [2] (see Fig. 4-2(a)) in low-transmission pseudogap regions is produced, similar to the band shape of for constant dielectric structure proposed by O'Brien and Pendry [63].

4.3 Results

For $LiTaO_3$, a polaritonic material which is extensively used experimentally [78, 14], $\omega_T = 26.7$ THz, $\omega_L = 46.9$ THz, and $\varepsilon_\infty = 13.4$. The low-frequency dielectric limit has a relatively high value of $\varepsilon_0 = \varepsilon_\infty \omega_L^2/\omega_T^2 = 41.4$, a key factor in observing Mie resonance behavior in the presence of dissipation. To our knowledge, it is the only material for which the loss parameter γ has been accurately measured: $\gamma = 0.94$ THz [78]. In order for the effective medium approximation to be valid, the operating wavelength must be much larger than the lattice constant [87]. This condition is easily satisfied by choosing a much smaller than $2\pi c/\omega_T$, since all of the Mie resonances lie

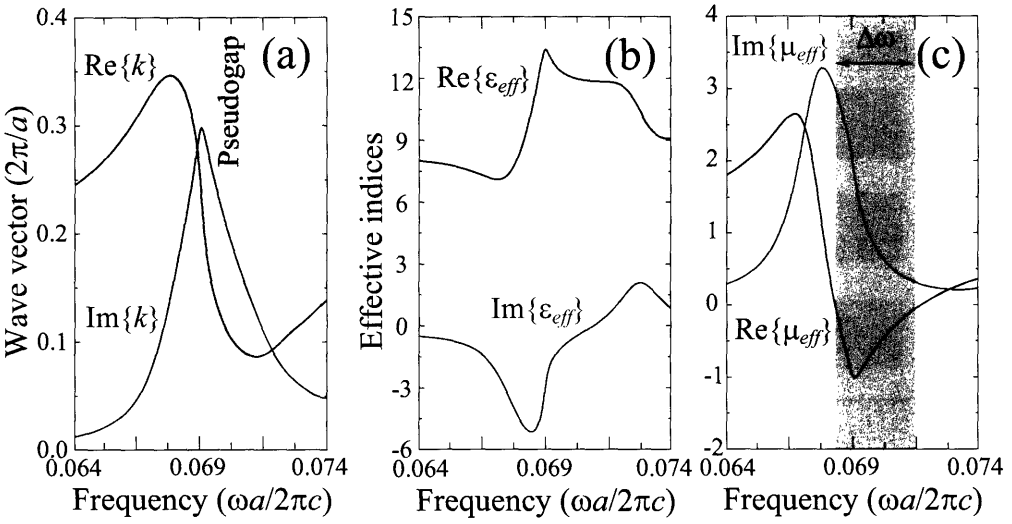

Figure 4-2: Band structure and effective indices in the $LiTaO_3$ polaritonic photonic crystal shown in Fig. 4-1 with $a = 0.87\mu$m and $s = 0.89a$. Note the backbending shape of the band in (a) and the resonant shape in (b) ε_{eff} and (c) μ_{eff}. The yellow shaded region in (a) indicates the approximate position of the pseudogap in the infinite photonic crystal. The gray shaded region in (c) indicates the frequency interval where $\mu_{\text{eff}} < 0$.

below ω_T. For the TE polarization, it will therefore always be the case that the resonances $\hat{\omega}_{lm}$ overlap with the lowest band of the MD crystal [36].

In Fig. 4-2, we compute the band structure and effective permittivity and permeability for a 1024-layer slab with $a = 0.87\mu$m and $s = 0.89a$ at frequencies inside the pseudogap region near $\hat{\omega}_{11} = 0.071(2\pi c/a)$. We find that there is a resonant shape in ε_{eff} and μ_{eff}, with $\mu_{\text{eff}} < 0$ over a frequency range I_ω of width $\Delta\omega = 1.18$ THz. This corresponds to a wavelength range $\Delta\lambda = 0.6\mu$m around the wavelength $\lambda_0 = 12.5\mu$m, where μ_{eff} is minimized.

We have chosen s and a to minimize λ_0, while maintaining at least a single frequency where $\mu_{\text{eff}} = -1$. The Mie resonances are localized, thus their frequencies scale only with s, not a. As $s \to 0$, $\hat{\omega}_{11} \to \omega_T$, which would result in the ultimate minimization of λ_0 were it not for the large losses in this frequency regime. Therefore, we choose a rod size s large enough that $\hat{\omega}_{11}$ is reasonably far away from the phonon absorption peak. Changing a has a small effect on the band structure: as a decreases,

the mode wave vector k becomes more lossy. Thus, we reduce a until losses are too large to permit $\mu_{\text{eff}} = -1$ anywhere within the first pseudogap. We then tune s to achieve the smallest possible λ_0.

The operating wavelength λ_0 of this polaritonic photonic crystal medium lies in a completely different part of the electromagnetic spectrum from the microwave-frequency ferroelectric system studied by O'Brien and Pendry [63]. In addition, other polaritonic media can be used in place of $LiTaO_3$ to create an effective medium with negative μ_{eff} in other wavelength ranges of interest. All that is required for resonant μ_{eff} is a combination of a large value of ε_1 and a small lossy component ε_2 at $\hat{\omega}_{11}$. The maximum in ε_1 occurs at the frequency $\omega_m = \sqrt{\omega_T^2 - \omega_T\gamma}$, where

$$\varepsilon_1^{\max} = \varepsilon_\infty \left[1 + \frac{\omega_L^2 - \omega_T^2}{\gamma(2\omega_T - \gamma)}\right]. \tag{4.4}$$

For the $LitaO_3$ crystal in Fig. 4-2, $\varepsilon_1^{\max} = 416$. However, at that point the material is far too lossy to exhibit much field penetration. At the first Mie resonance, the real component $\varepsilon_1 = 109$ is large, while the imaginary component $\varepsilon_2 = 9.3$ is not yet high enough to prohibit localized modes in the polariton rod. In Fig. 4-3, we plot the maximal value of ε_1 for 27 different polaritonic materials. Because experimental values of the loss factor are not available for most of these materials, we show results for $\gamma = \omega_T/30$ and $\gamma = \omega_T/300$. Clearly, TlBr, TlCl, and $LiTaO_3$ are (the only) ideal candidates if $\gamma = \omega_T/30$. However, since $\varepsilon_1^{\max}$ changes roughly linearly with $1/\gamma$, a reduction in γ by an order of magnitude transforms the other materials into viable options to realize negative μ_{eff}. Of these, the most interesting is SiC, which has the largest $\omega_T = 149$ THz.

In Table 4.1, we list the (s, a) combinations which minimizes λ_0 for several polaritonic media (TlBr, TlCl, $LiTaO_3$ and SiC) with phonon frequencies ranging from 8.1 THz to 149 THz [46]. Since absorption peak width estimates are not available, we have assumed that $\gamma = \omega_T/30$ for TlCl and TlBr, as in $LiTaO_3$. Due to their high dielectric response characteristics at low frequency, the effective permeability exhibits a resonance at the respective $\hat{\omega}_{11}$ with similar characteristics to the $LiTaO_3$ structure.

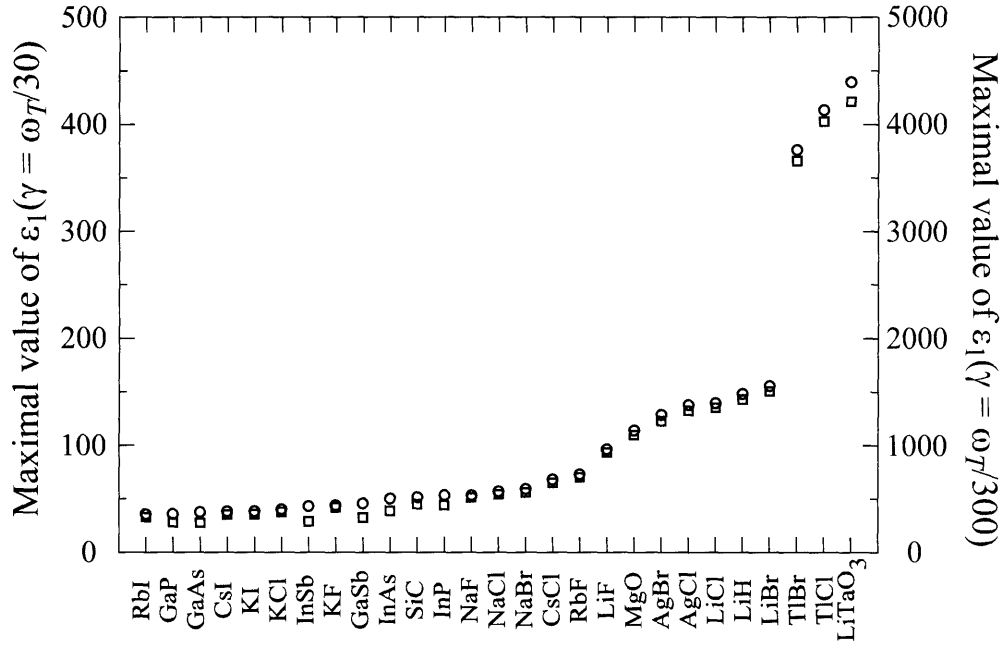

Figure 4-3: Maximal value of ε_1 from Eq. 4.4 for 27 different polaritonic materials. With an assumed loss of $\gamma = \omega_T/30$ (blue circles, left axis), the only viable media to realize negative effective permeability are TlBr, TlCl, and $LiTaO_3$. However, with $\gamma = \omega_T/300$ (red squares, right axis), every material is a reasonable option.

material	ω_T	ε_0	ε_∞	a	s/a	$\boldsymbol{\lambda_0}$	$\boldsymbol{\Delta\lambda}$
TlBr	8.1	29.8	5.4	3.22	0.88	**41.4**	**1.9**
TlCl	12	31.9	5.1	2.05	0.90	**27.9**	**1.3**
$LiTaO_3$	26.7	41.4	13.4	0.87	0.89	**12.5**	**0.6**
SiC	149	9.6	6.7	0.15	0.88	**2.04**	**0.01**

Table 4.1: A comparison of minimal operating wavelengths for negative effective permeability in 2D square photonic crystals composed of square rods of various polaritonic materials. The phonon frequency ω_T is given in terahertz, while the lattice constant a and wavelengths λ_0 and $\Delta\lambda$ are given in microns. The loss factor γ is assumed to be $\omega_T/30$ for TlBr and TlCl and $\omega_T/300$ for SiC. λ_0 ranges from 2 to 41 microns, and in each case λ_0 is much larger than the lattice constant a.

We demonstrate that for a material like SiC, which has a much smaller ε_0, a μ_{eff} resonance with $\mu_{\text{eff}} < -1$ results if γ is as small as $\omega_T/300$.

4.4 Discussion

Since the polaritonic Mie resonance is localized, the resonant μ_{eff} is not dependent on the symmetry of the lattice. Indeed, we have found $\mu_{\text{eff}} < 0$ near $\hat{\omega}_{11}$ for a triangular lattice of square rods with the same size as those used in Fig. 4-2. In addition, the frequency dispersion of $\varepsilon(\omega)$ has little effect on the μ_{eff} resonance; similar results are obtained using constant $\tilde{\varepsilon} = \varepsilon(\hat{\omega}_{11})$. The important quantities are the size and shape of the polariton rod, which determine the frequency of the Mie resonances. We note that by changing s and a, we can easily vary λ_0 by a factor of $\sim 2-3$. Therefore, operating wavelengths in the range 2 to ~ 100 microns are attainable with different structures using only the four polaritonic materials in Table 4.1. However, it is important to note that some ambiguity in the effective indices arises from the freedom of choice in the placement of the air/effective medium interface [87]. Any inconsistencies can be minimized by using a lattice constant only slightly larger than the rod size.

The characteristic back-bending band shape near $\hat{\omega}_{11}$ also occurs at higher-order Mie resonances, but the strength of the μ_{eff} resonance is greatly reduced. This is a property not solely due to the decrease in the ratio $\varepsilon_1/\varepsilon_2$ as ω approaches ω_T; a similar

reduction occurs in constant dielectric structures. If we consider a system like the one in Fig. 4-1, with $s = 0.8a$ and a fixed $\tilde{\varepsilon} = \tilde{\varepsilon}_1 + 5i$, a resonance with negative μ_{eff} near the frequency $\hat{\omega}_{31}$ does not occur unless $\tilde{\varepsilon}_1 > 116$. In contrast, negative permeability is found near $\hat{\omega}_{11}$ for $\tilde{\varepsilon}_1 > 60$ and the minimum value of $\text{Re}[\mu_{\text{eff}}]$ for $\tilde{\varepsilon}_1 = 116$ is -2.9.

In summary, we have shown that two-dimensional polaritonic photonic crystals can act as metamaterials with negative effective permeability due to their high-index behavior below the phonon resonance. In addition, we have demonstrated that the frequency range of resonant μ_{eff} behavior can be predicted by studying the locations of the Mie resonances and the corresponding magnitude of ε. Furthermore, we have shown that a variety of polaritonic media may be useful to achieve negative permeability over a wide range of operating wavelengths from 2 to $\sim$100 microns. Since the operating wavelength is primarily a function only of the shape and size of the polariton rod, it is likely that similar resonant μ_{eff} behavior can be obtained in three-dimensional polaritonic photonic crystals. Finally, the metallic behavior ($\varepsilon_1 < 0$) of polariton materials above ω_T suggests it may be possible to construct left-handed materials with $\varepsilon_{\text{eff}} < 0$ and $\mu_{\text{eff}} < 0$ simultaneously using a hybrid structures of multiple polariton elements [82].

Chapter 5

Microscopic Properties of Melting at the Surface of Semiconductors

Segments of this chapter have been submitted for publication in Phys. Rev. Lett.

5.1 Introduction

Melting is the phase transition from a solid phase to a liquid phase. An all too familiar example is the melting of ice to water. However, a complete understanding of this complicated phenomenon has not yet been achieved [94, 7, 13, 12, 8, 9]. Nevertheless, among all the complexities, there are several unifying principles governing all melting behaviors. It has long been understood that melting usually initiates from defects within the otherwise perfectly periodic crystal [8]. They can be defects inside the bulk such as point defects, line defects and grain boundaries [12, 7, 69, 68]. They can also be free surfaces [9], where the crystal abruptly stops. The role of free surfaces in initiating melting has been studied both from an experimental point of view [1, 11, 15] and from theoretical investigations [68, 92]. Surface melting is the stage where the bulk material still exists in the solid phase, while the surface of the material, due to its lower coordination, has already started the phase transition into liquid.

It was shown experimentally by Daeges and coworkers that thin (macroscopic) coatings of a different material can change the melting behavior of the substrate. In

Ref. [15], they described an experiment where a Ag crystal coated with a $\sim 10-20$ micron-thick layer of Au achieved superheating of 25 K for one minute. By replacing the Ag-air interface with a Ag-Au interface, the core Ag material does not melt. Similar superheating behavior has also been observed in quartz/cristobalite crystals surrounded by fused silica [1] and Ar bubbles in Al [76]. Qualitatively, this can be explained by the following argument. The surface is known to play an important role in initiating melting. If the surface of a lower melting point material is coated with a higher melting point material, then even at a temperature higher than the lower melting point, the core material will not melt since its surface is maintained in a solid phase by the coating.

To investigate the role played by the interface in the melting transition, we ask whether such superheating phenomena are possible when the coating is a minimal perturbation to the underlying surface. We will study the (110) surface of GaAs, which is the natural cleavage plane of GaAs, and the corresponding surface of Ge. With the only significant difference being their covalent or ionic bonding nature, a single monolayer of GaAs on Ge or vice versa can be considered a textbook example of how a coating could alter the melting behavior of a substrate. Although Ge and GaAs have almost identical lattice constants and average masses, the melting temperature of GaAs is higher than that of Ge by over 300 K. So what might happen if Ge and GaAs coexist at a temperature in between their melting points? We approach the problem by looking at the microscopic behavior of melting at the surface. In doing so, we hope to shed light on how one may control or alter the behavior of materials near the melting point, which could have implications for high-temperature materials applications.

The different melting points of the two materials is intriguing. Ge melts at $T_m(\mathrm{Ge}) = 1211$ K, while GaAs remains solid until $T_m(\mathrm{GaAs}) = 1540$ K [45]. The two systems have almost identical lattice constants. Considering that Ga, Ge, and As are three consecutive elements in the periodic table, the ion masses are very similar, and in fact the average mass is nearly identical in Ge and GaAs. Thus, the largest difference between the two bulk materials is the bonding character. The tetrahedral bonds

in Ge are fully covalent, while those in GaAs have some amount of ionic character.

Surprisingly, the formation enthalpy for Ge is 264 kJ/mol, more than 25% larger than that of GaAs at 210 kJ/mol. Thus, it takes less energy to "pull" a GaAs crystal apart than it takes to do the same to a Ge crystal. Yet, Ge melts at a temperature 300 K lower than what is necessary to melt GaAs. That is to say, it is easier to change Ge from solid to liquid than GaAs, but it is easier to change GaAs all the way to gas than it is for Ge.

On the (110) surface, another prominent difference between the two systems exists. The top layer GaAs dimers buckle in such a way that As atom moves away from the surface and its dangling bond is completely filled, while the Ga atom sinks into the surface with an empty dangling bond. The choice of the buckling in this case is determined by the bond energy difference between the dangling bonds of the surface Ga and As atoms. For the Ge surface, however, the two dangling bonds of the Ge dimer atoms are degenerate. The buckling involves a spontaneous symmetry breaking. The energy difference of the resulting bonds are smaller than that of GaAs. Therefore, the Ge surface band gap is smaller and is easier to metallize, which we will suggest could be a prelude to melting.

In Sec. 5.2, we describe the *ab-initio* density functional technique used to study the electronic structure of a surface at finite temperature. In Sec. 5.3, we demonstrate that a coating of GaAs only a single-monolayer in thickness can cause superheating in a Ge crystal. We also demonstrate how the band structure and charge density information provides new information about the timing and mechanisms of the melting transition.

In Sec. 5.4, we demonstrate that a single-monolayer coating of Ge can induce melting in a GaAs crystal at a temperature in between their melting points. In Sec. 5.5, we suggest that melting is induced by the penetration of surface atoms that have broken bonds with the rest of the surface layer into the bulk. Finally, in Sec. 5.6, we discuss potential sources of error and unanswered questions about melting at interfaces.

5.2 Computational details

The simulations in this work utilize a molecular dynamics approach based on pseudopotential density functional theory energy minimization intended to provide an accurate description of the Ga and As atoms.

5.2.1 Density functional molecular dynamics

The time evolution of the system is determined according to the Born-Oppenheimer approximation, separating the ion degrees of freedom from the electron degrees of freedom. At each time step, the ion locations are fed into the electronic calculations, where density functional theory is used to minimize the total electronic free energy. The forces on the ions are then calculated and the ions moved using classical molecular dynamics.

The positions of the ions are updated using the Verlet Algorithm, which uses a standard discretization of Newton's equation:

$$m\frac{\partial^2 \mathbf{x}(t)}{\partial t^2} = \mathbf{F}(t) \Rightarrow \mathbf{x}_{i+1} = 2\mathbf{x}_i - \mathbf{x}_{i-1} + \frac{dt^2}{m}\mathbf{F}_i. \tag{5.1}$$

The temperature is maintained using a Nose thermostat approach, whereby the velocities are rescaled after each step to restore a fixed total kinetic energy. In this, our study follows the same spirit as an earlier work done by Tosatti and coworkers [92], which used the same method to study the melting of the Ge(111) surface.

There have been previous studies of melting with empirical potentials [69]. For example, for Si melting there exist high quality three-body potentials such as those from Stillinger and Weber, which could reproduce a wide variety of physical properties [90]. These studies usually can access a much longer time scale than corresponding quantum mechanical studies, because of the lower computational requirement of empirical potentials. However, for heteropolar materials such as GaAs, a high quality empirical potential which works well around the melting temperature has not yet been produced. In addition, the quantum mechanical treatment of the electrons also

has the added benefit that it allows us to obtain the electronic band structure and the charge density information, in addition to ion trajectories.

5.2.2 Supercells

The computational supercells that we consider are composed of four free 3×3 layers (18 atoms/layer) of either Ge or GaAs, capped by a frozen layer terminated with Hydrogen atoms. The frozen layer is placed at $z = 0$. To eliminate interactions between the top (surface) layer and the Hydrogen layer in the cell above, the supercells are separated by $\sim$ 15a.u. of vacuum [92]. In Sec. 5.3, we will compare the melting dynamics of the bare Ge(110) surface in Fig. 5-1(a) and the GaAs monolayer-coated surface [Ge(110)+GaAs] in Fig. 5-1(b). In Sec. 5.4, we will compare the melting dynamics of the bare GaAs(110) surface in Fig. 5-1(c) and the Ge monolayer-coated surface [GaAs(110)+Ge] in Fig. 5-1(d). Simulations were performed using the freely-available plane-wave density-functional code DFT++ [39]. Unless otherwise noted, we have used a cutoff energy of 5 hartrees and 200 bands in the electronic iterations, and a time step of $dt = 16$fs for the ionic motion. Due to the large size of the supercell, it is only necessary to compute the density at the wavevector $k = \Gamma$. This has allowed us to study time scales of up to $\sim$ 12ps, more than enough to compare melting behaviors in these surface structures.

5.3 Superheating a Germanium surface

We first compare the dynamics of a Ge surface at 1240 K to a similar structure where the top layer of Ge has been replaced by a GaAs monolayer. Due to the difference in melting temperatures, we expect that for $T > 1211$K and $T < 1540$K, a bare Ge surface will go into a liquid phase rather quickly, while atoms on a GaAs surface should have very slight diffusion. Can a microscopic, single-monolayer coating produce a significant change in the state of the surface and/or bulk? Similar to the gold-on-silver experiments of Daeges *et al.* [15], the GaAs-on-Ge arrangement could lead to a better resistance to melting because of the "tough surface character" of the

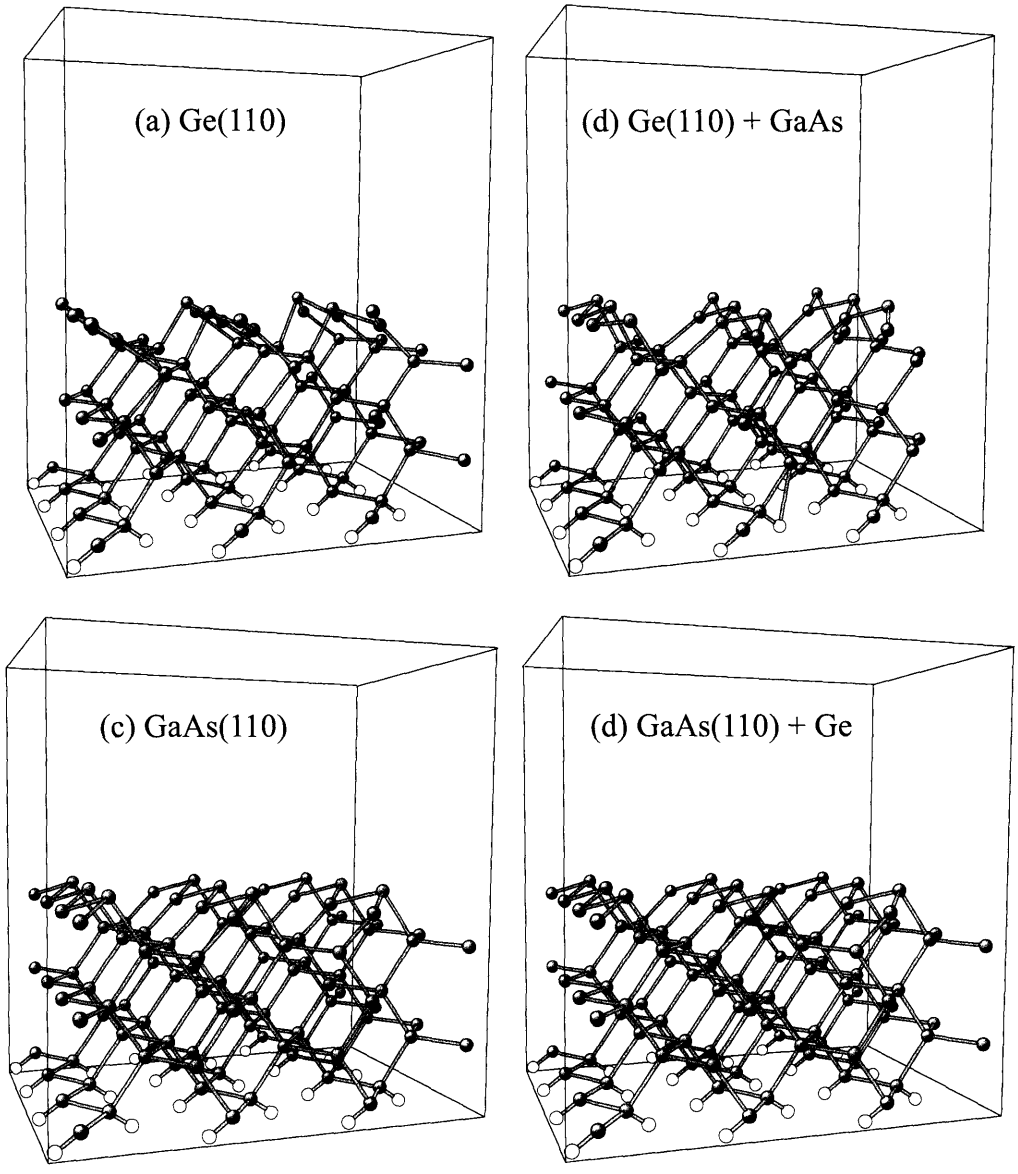

Figure 5-1: Computational supercells: (a) the (110) surface of Ge [Ge(110)]; (b) the Ge(110) surface with a single-monolayer coating of GaAs [Ge(110)+GaAs]; (c) the (110) surface of GaAs [GaAs(110)]; and (d) the GaAs(110) surface with a single-monolayer coating of Ge [GaAs(110)+Ge]. Ge atoms are shown in green, Ga in blue, Ar in red, and H in white.

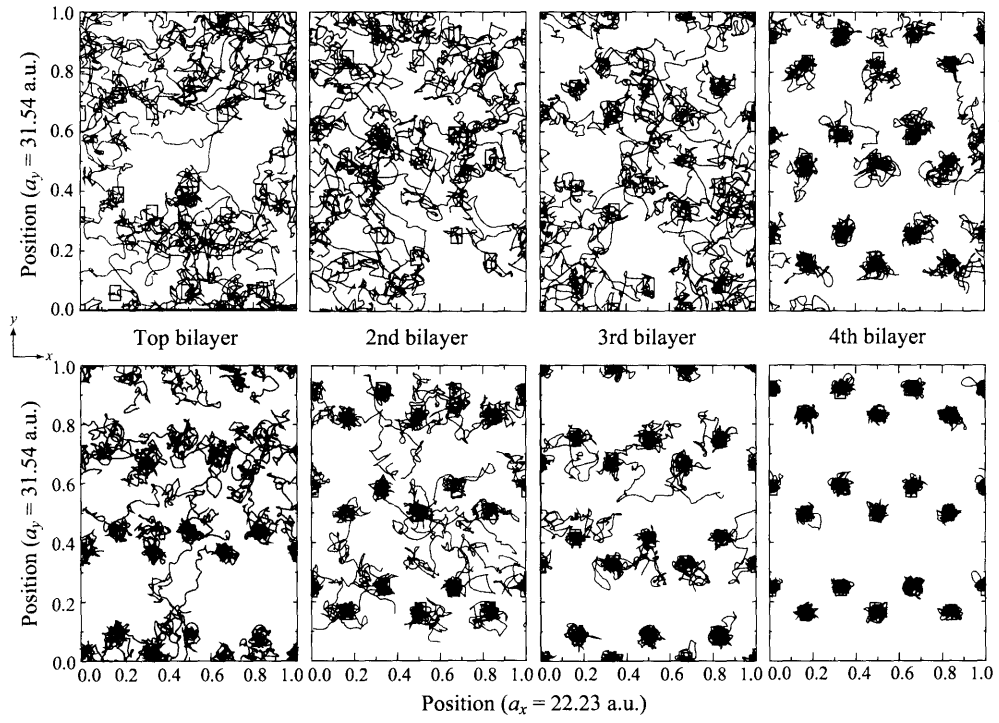

Figure 5-2: Ion trajectories of the atoms on a Ge(110) surface at 1240 K, with (bottom) and without (top) a single-monolayer coating of GaAs, as they appear looking down the (110) direction. Ga trajectories are shown in blue, Ar in red, and Ge in green. The black diamonds (Ga), ovals (Ar), and rectangles (Ge) mark the initial positions of the atoms at $t = 0$. Note the decrease in diffusive motion of the Ge atoms in the presence of a GaAs monolayer coating.

GaAs layer.

5.3.1 Ion trajectories

In Fig. 5-2, we plot the trajectories of the ions in each layer projected onto the (x, y) plane over a 10ps period, starting with an equilibrium $T = 0$ configuration. While there are still bond-breaking events in the GaAs monolayer and the two Ge layers below, it is clear that the motion of the Ge ions in the second, third, and fourth layers is dramatically slowed by the presence of the GaAs coating. Furthermore, the fourth layer appears to be more or less in the ideal crystal positions; that is, completely solid. We will show shortly that this is not an effect of the frozen layer below.

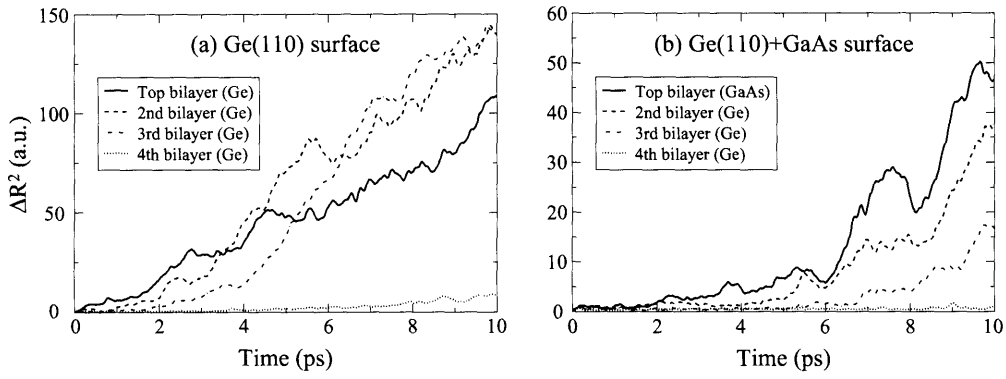

Figure 5-3: Mean-square displacement $\langle R^2 \rangle$ averaged over the atoms within each of the top four layers of a Ge(110) surface at 1240K (a) without and (b) with a monolayer coating of GaAs.

A clear signal that distinguishes a melted liquid from an amophous solid is the existence of normal diffusive motion characterized by a linear increase in the mean-square displacement $\langle \Delta R^2 \rangle$ as time progresses [92]. In the surface systems we have considered, the motion is primarily in planes normal to the surface, so we consider

$$\Delta R^2 = \Delta x^2 + \Delta y^2 \tag{5.2}$$

and ignore the motion in the z-direction. In Fig. 5-3, we plot $\langle R^2 \rangle$ for the atoms in each layer of the Ge(110) surface, with and without a GaAs-monolayer coating. All four free layers of the Ge(110) surface appear liquid. In the GaAs-coated system, the GaAs monolayer and the first two underlying Ge layers have melted, but the mean-square displacement is roughly constant for the still-solid fourth layer whose atoms are essentially vibrating about their initial positions. Thus, we conclude that 29 degrees of superheating in the fourth layer (and the remainder of the bulk) can be achieved with a single-monolayer coating of GaAs. This surface melting state is similar to the state observed on the Ge(111) surface by Tosatti and coworkers [92] and represents a significant change from the rapid melting of the homogeneous Ge surface.

The diffusion constant D_j for the atoms in a liquid layer j can be obtained from

T (K)	Ge(110) surface				Ge(110)+GaAs surface			
	D_1^{Ge}	D_2^{Ge}	D_3^{Ge}	D_4^{Ge}	D_1^{GaAs}	D_2^{Ge}	D_3^{Ge}	D_4^{Ge}
1240	80	120	120	10	70	50	30	N/A
1270	90	80	120	10	130	80	40	2
1540	800	800	400	100	100	100	200	60

Table 5.1: Diffusion constant averaged over layer. Columns 2-5 correspond to the free layers of a Ge(110) surface, while columns 6-9 correspond to the layers of a Ge(110)+GaAs surface. All quantities are given in units of 10^{-6}cm^2/s.

a fit to the equation

$$\langle \Delta R^2 \rangle_j(t) = 4D_j t \tag{5.3}$$

(see Table 5.1). The factor of 4, rather than 6, in Eq. 5.3 is due to the fact that the diffusive motion is primarily two-dimensional, as previuosly discussed. The diffusion constant of the Ge atoms in the second layer, D_2, is reduced by a factor of 2.4 by the GaAs coating, while D_3 is reduced by a factor of 4.

The contrast between the diffusive motion of the top three layers of the Ge(110)+GaAs surface and the near-fixed positions of the atoms in the fourth layer prompts the question of whether this is an artifact due to the finite thickness of the slab and the fact that the bottom layer of Ge atoms is frozen in our simulation. To check if the atoms in the fourth layer are restricted in their motion because of their bonds with the fixed layer, we examine the total kinetic energies of each layer, converted to effective temperatures using the relation

$$KE_j = \sum_i \frac{1}{2} m_i v_i^2 = \frac{3}{2} k_B T_j, \tag{5.4}$$

where v_i is the velocity of atom i in each layer j.

In Fig. 5-4, we observe that the effective temperatures T_j quickly reach equilibrium around the target of 1240 K. Thus, we conclude that although the fourth layer has far less mean-square-deviation, these atoms have significant kinetic energy on par with the other layers. These atoms are moving vigorously despite the frozen layer below, they are simply not diffusing as much as those in the layers above.

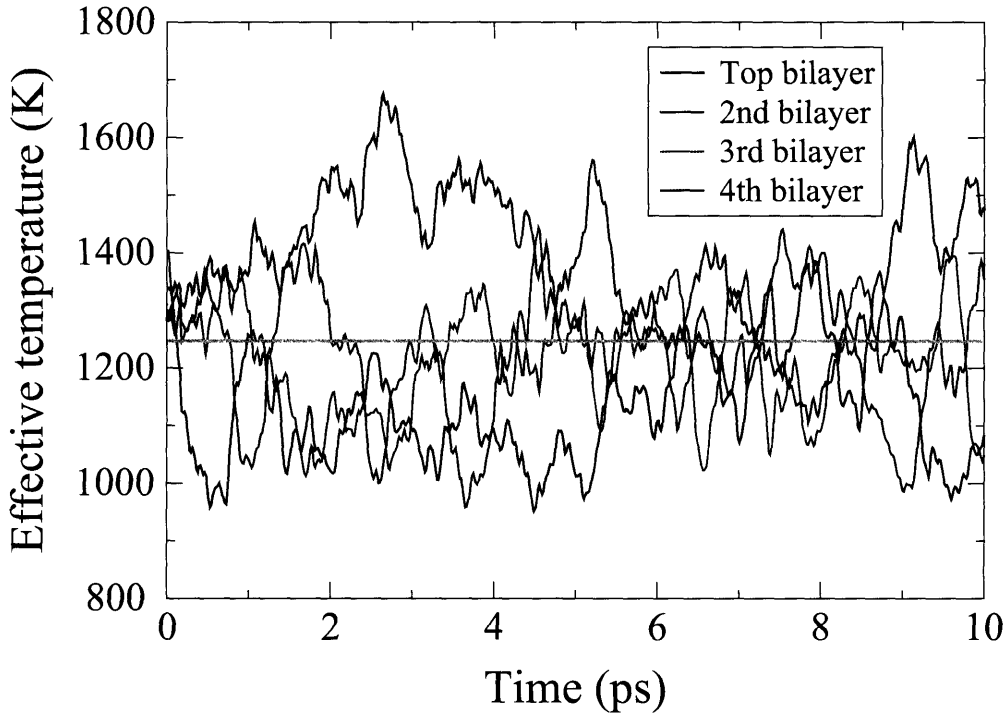

Figure 5-4: The kinetic energy of the Ge(110)+GaAs surface at 1240 K (orange line), averaged over the atoms in each layer and converted to an effective temperature.

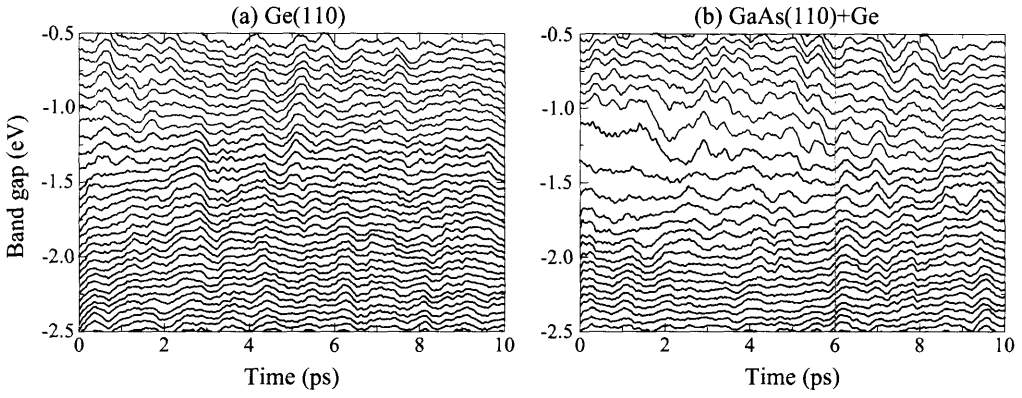

Figure 5-5: The band energies of the (a) Ge(110) and (b) Ge(110)+GaAs surfaces at 1240 K. Valence bands are in red and conduction bands in green.

5.3.2 Electronic signals of melting

Phillpot *et al.* use the magnitude of the structure factor in each layer to pinpoint the progression of melting from a defect in a crystalline system [68]. In addition, our *ab-initio* density functional calculations provide other information that can be used to pinpoint the time that the melting transition occurs. In Fig. 5-5, we plot the band energies at the Γ-point for the Ge(110) and Ge(110)+GaAs surfaces. In Fig. 5-6, we plot the band gap energy difference, $\Delta\omega$, between the highest conduction band and the lowest valence band for the same structures. It is clear that the Ge(110) band gap disappears ($\Delta\omega$[Ge] $<\sim$ 0.1eV) very quickly since the temperature is 29 degrees above the melting point. However, the band gap for the Ge(110)+GaAs surface slowly collapses over the first 6 picoseconds. This correlates with the reduction of diffusive motion of the Ge atoms in the two layers below the GaAs monolayer coating in Fig. 5-3. We note that the calculated band gap is smaller than expected due to the local density approximation and the existence of surface states.

To take a closer look at the electronic mechanism what initiates the collapse of the band gap, we study the charge distribution of the Ge(110)+GaAs system during the time period up to $t = 6$ ps. Shown in Fig. 5-7 is the electron charge density in slices through planes of maximum average density perpendicular to the x and z axes before the run starts and after 4 and 6 ps. The time $t = 4$ ps is chosen because this

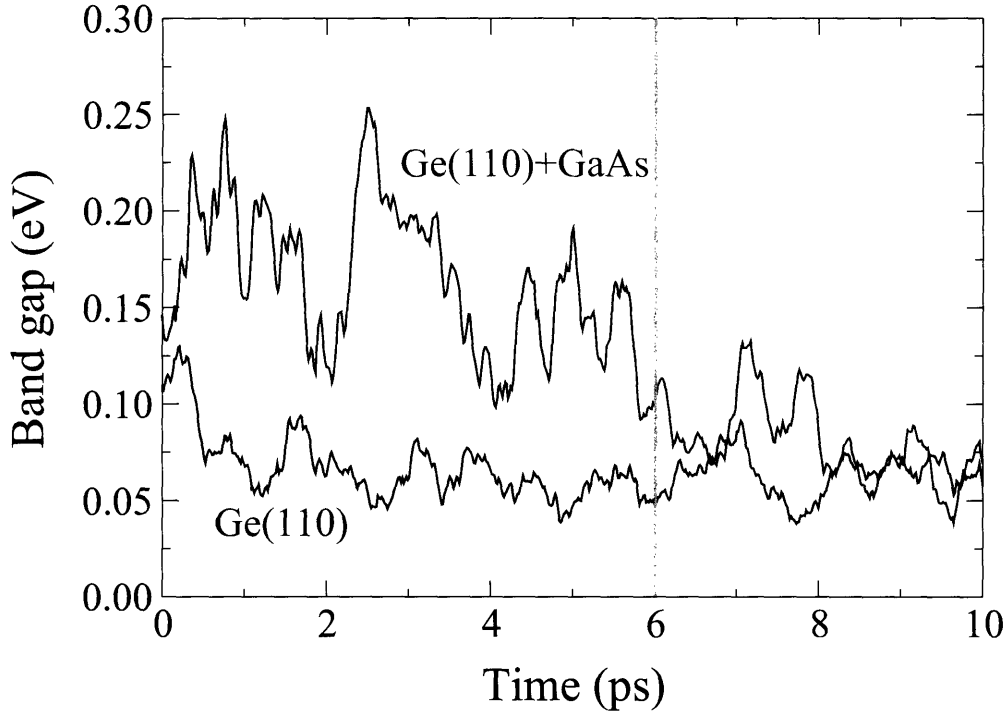

Figure 5-6: The bandgap energy in eV for the Ge(110) and Ge(110)+GaAs surfaces at 1240 K. Notice the collapse of the Ge(110)+GaAs bandgap at $t \approx 6000$fs (orange line), signifying a change in character from semiconducting to metallic.

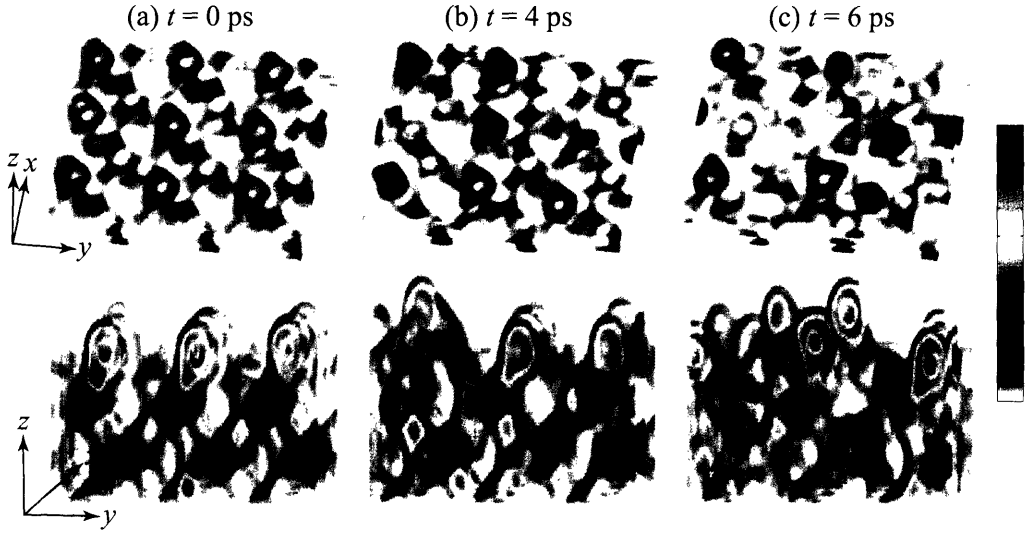

Figure 5-7: Slices of the charge density of the Ge(110)+GaAs surface at (a) $t = 0$ ps, (b) $t = 4$ fs, and (c) $t = 6$ ps. The top row of panels shows the view looking down the surface in planes $z = 1.8, 5.1, 8.4, 11.6, 14.9$ a.u. The bottom row of panels shows the side view looking down the x-axis in planes $x = 0.5, 4.2, 7.9, 11.6, 15.3, 19$ a.u. The planes are chosen by maximum average density. The color scheme is indicated on the right with maximum density in red and zero density in white.

marks the approximate beginning of the linearity of $\langle \Delta R^2 \rangle$ (see Fig. 5-3). There are little changes to the bottom free layer, so we focus on the top three layers. Comparing Figs. 5-7(a) and (b), many of the atoms in the first(second) layers have reduced their coordination number from 3(4) to either 1 or 2. After 6 ps, close to the point of band gap collapse, many bonds are broken throughout the top three layers. In addition, the electrons are more spread out, which would explain the metallic behavior of the system.

Intuitively, the level of superheating that can be achieved will decrease with increasing temperature, until eventually the GaAs monolayer-coating ceases to provide sufficient resistance against the melting of the bulk. Where and how this transition occurs cannot be quantitatively addressed by our simulations due to the finite height of our supercell, but we have studied the Ge(110) and Ge(110)+GaAs surfaces at two other temperatures to get a rough idea of the deterioration of the coating performance. In Table 5.1, we list the diffusion constants for each layer at $T = 1240$, 1270,

and 1540 K, the experimental melting point of GaAs. There are several sources of error (see Discussion in Sec. 5.6) that are increasingly important as T is increased. Nevertheless, our simulations show that when T reaches 1270 K, the third Ge layer beneath the GaAs coating begins to melt, and by the GaAs melting temperature of 1540 K, all Ge layers are thorougly mixed in a liquid form, albeit with a noticeable reduction in diffusion constant compared to the bare Ge(110) surface. Ultimately, to study the superheating phenomenon at higher temperatures will require adding more free-moving layers to the bulk.

5.4 Induced melting in a Gallium Arsenide surface

Given that the behavior of the Ge surface is so strongly regulated by the presence of a GaAs coating, we next ask what effect a single-monolayer coating of Ge will have on a GaAs surface. It is clear from Figs. 5-2 and 5-3 that a Ge surface will melt at 1240 K, but we expect that a GaAs surface would remain solid 300 degrees below its melting point. We might expect the coated surface to behave in one of the following three ways: (*i*) the Ge coating will form a liquid monolayer on top of a solid GaAs bulk, (*ii*) the stable GaAs bulk will stabilize the Ge monolayer, or (*iii*) the Ge monolayer will become disordered and induce melting in the underlying GaAs surface. In Fig. 5-8, we compare the trajectories of the ions in each layer of a GaAs surface to the system where the top layer has been replaced by Ge atoms. We find that the ion dynamics are dominated by the character of the top layer, even more strongly than the Ge(110) surfaces in Sec. 5.3. Unsurprisingly, the bare GaAs surface exhibits very little motion in any layer. This is in stark contrast to the coated GaAs(110)+Ge surface where both the Ge atoms and the underlying layer of GaAs are highly diffusive.

As in Sec. 5.3, we use the mean-square displacement, band structure, and charge density to study the details of the melting process. In Fig. 5-9, we plot the average displacement of the atoms in the top two layers of each system. As expected, we find a constant $\langle R^2 \rangle$ for each layer of the bare GaAs(110) surface, signifying nondiffusive motion and a solid structure. However, $\langle R^2 \rangle$ is linear in time for the top two layers of

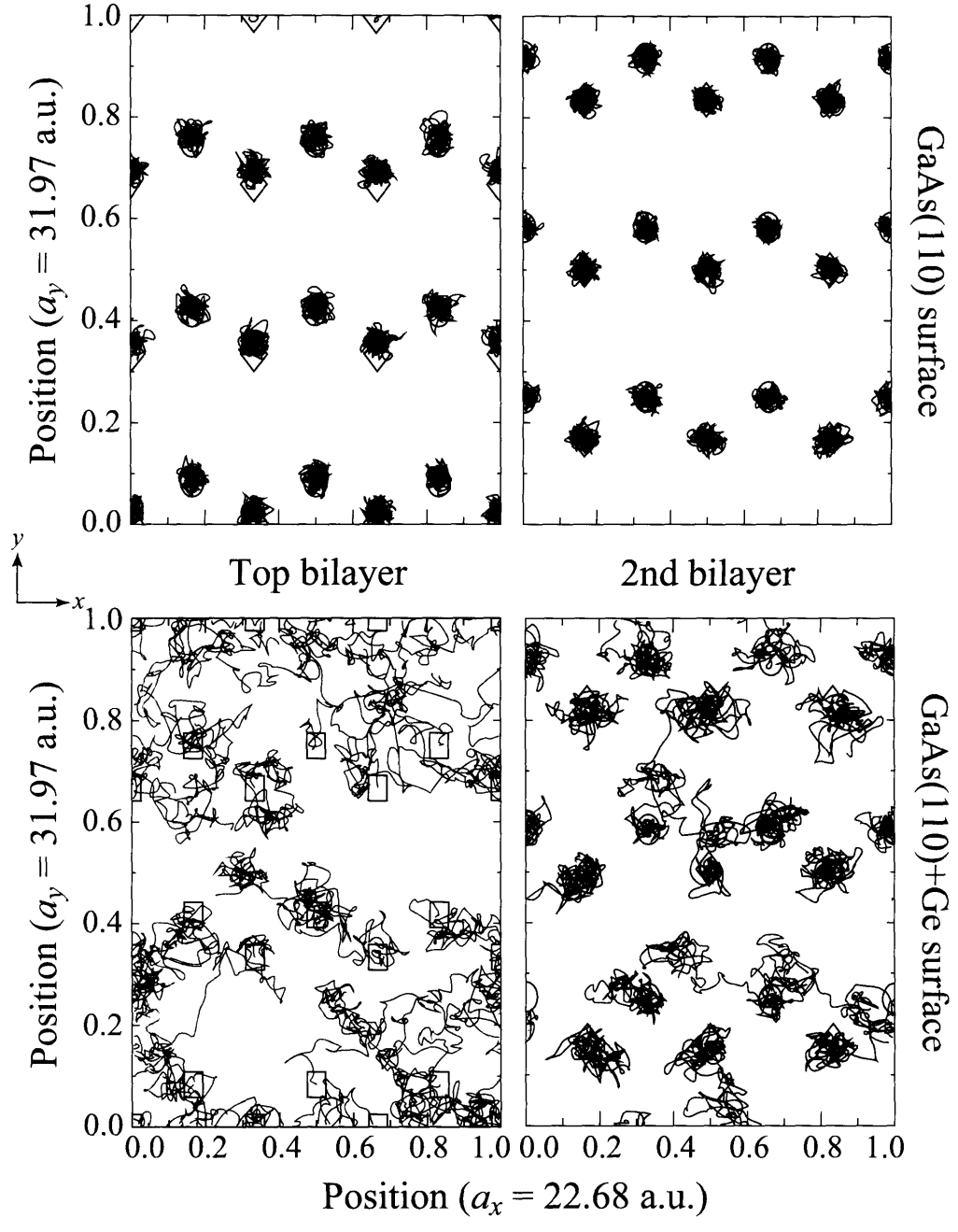

Figure 5-8: Ion trajectories of the top two layers of a GaAs surface at 1240 K, with (bottom) and without (top) a single-monolayer coating of Ge, as they appear looking down the (110) direction. Color scheme is the same as in Fig. 5-2. Note how the Ge monolayer induces melting in the underlying layer of the GaAs crystal.

Layer	$D_{\text{GaAs(110)}}$	$D_{\text{GaAs(110)+Ge}}$
1 (GaAs/Ge)	N/A	40
2 (GaAs)	N/A	10

Table 5.2: Diffusion constant averaged over layer for the top two layers of the GaAs(110) and GaAs(110)+Ge surfaces. All values are given in units of $10^{-6}\text{cm}^2/\text{s}$. The third and fourth layers of the GaAs(110)+Ge surface and all layers of the GaAs(110) surface have a constant, rather than linear, $\langle R^2 \rangle$ vs. t relationship.

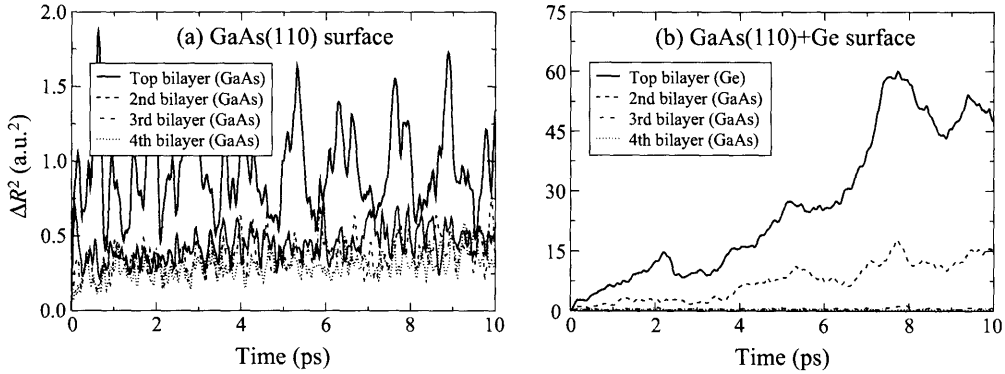

Figure 5-9: Mean-square displacement $\langle R^2 \rangle$ averaged over the atoms within each of the top four layers of a GaAs(110) surface at 1240K (a) without and (b) with a monolayer coating of Ge. Note the large difference in scales between (a) and (b).

the Ge-coated surface, with significant diffusion constants (see Table 5.2). The third and fourth layers in each system remain solid up to $t = 10$ps. This state of induced surface melting 300 degrees below the melting point of GaAs is remarkable.

We plot the Γ-point band energies for the GaAs(110) and GaAs(110)+Ge surfaces in Fig. 5-10 and the band gap energy in Fig. 5-11. The band gap is greatly reduced by the presence of a Ge-monolayer coating and shows signs of a slow collapse, although it does not consistently remain below 0.1 eV as was found for the band gaps of the Ge(110) surfaces after 10ps in Sec. 5.3. This is probably a reflection of the stability of the third and fourth layers.

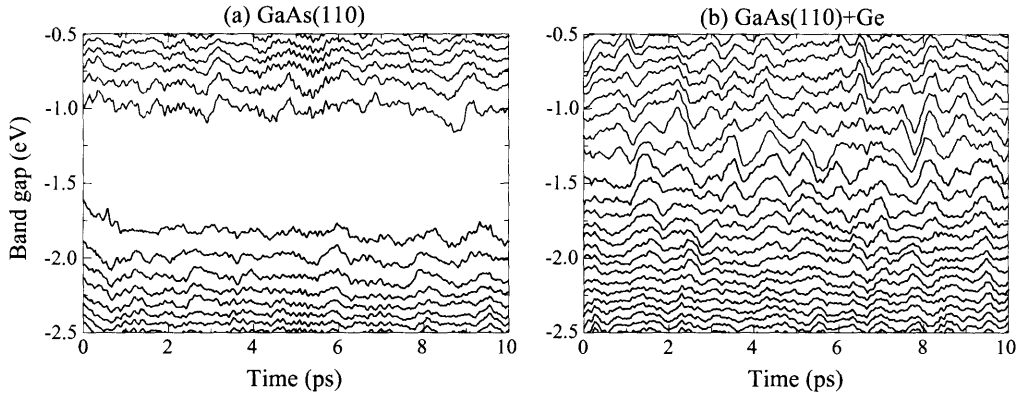

Figure 5-10: The band energies of the (a) GaAs(110) and (b) GaAs(110)+Ge surfaces at 1240 K. Valence bands are in red and conduction bands in green.

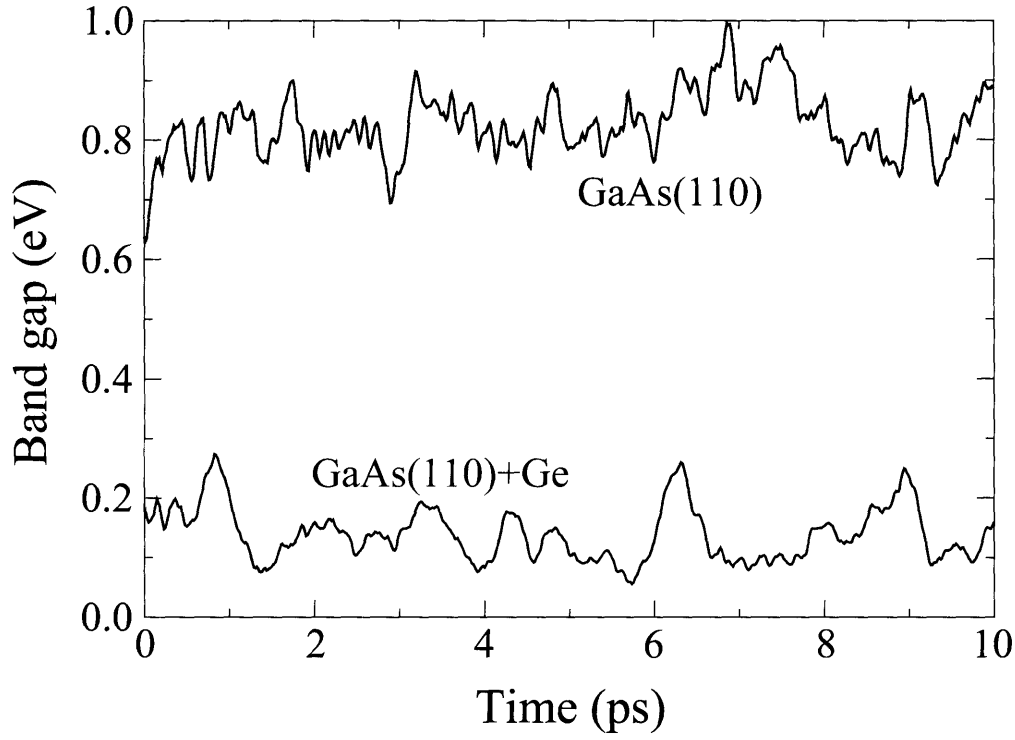

Figure 5-11: The bandgap energy in eV for the GaAs(110) and GaAs(110)+Ge surfaces at 1240 K. Notice that neither bandgap is completely collapsed on the 10ps time scale.

5.5 Penetration mechanism

Given that melting appears to progress from the surface inwards, we investigate the role of bond-breaking and penetration of surface atoms into the bulk in the propagation of the liquid-solid interface. The diffusive motion of the Ga and As atoms in the second layer is precipitated by bond-breaking events on the top Ge monolayer and the subsequent penetration of several Ge atoms into the GaAs surface. In Fig. 5-12, the charge density through planes of maximum average density perpendicular to the x (bottom) and z (top) axes is shown at times $t = 0, 4, 8$ ps. The top view shows the reduction in coordination number as bonds are broken and the electron density is smeared out. The side view indicates that the top two rows are becoming progressively disordered, while the third layer is relatively fixed in both position and density localization. For the purposes of studying the melting process, the Ge monolayer and the first GaAs layer may be considered the only free-moving atoms of any significance. In this system, only two atomic layers thick, we can isolate more easily the possible initiation mechanisms of melting.

In Fig. 5-13, we plot the z-component of the ionic coordinates of the four Ge atoms that penetrate past the initial position of the underlying plane of GaAs at $z = 11.25$a.u. during the 10ps run. By $t = 4$ ps, atoms A and B have broken away from the coating, and by $t = 8$ ps, atoms C and D have also made their way into the bulk. In Fig. 5-14, we plot the positions of these four atoms and the second-layer Ga and As atoms as colored shapes as they appear looking up from inside the bulk, where larger-sized shapes have penetrated farther into the bulk (decreasing z). The GaAs layer becomes more and more disordered as additional Ge atoms penetrate and interfere with the bonding structure.

This is clearly connected with the liquid dynamics of the second layer, and this penetration mechanism is likely also the cause of melting in other structures, though it is easiest to pin down in the coated GaAs structure due to the complete lack of melting in the bare GaAs structure. Furthermore, it explains why the GaAs monolayer-coating slows or stops the melting in the Ge layers of the Ge(110)+GaAs surface.

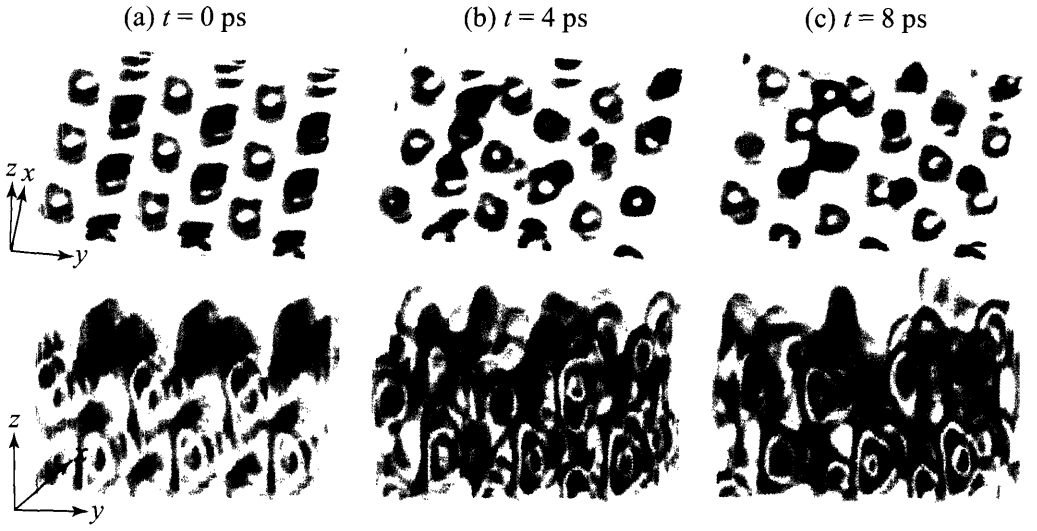

Figure 5-12: Slices of the charge density of the Ge(110)+GaAs surface at (a) $t = 0$ ps, (b) $t = 4$ fs, and (c) $t = 6$ ps. The top row of panels shows the view looking down the surface in planes $z = 1.5, 4.4, 7.3, 10.2.13.1$ a.u. The bottom row of panels shows the side view looking down the x-axis in planes $x = 0.5, 4.3, 8.1, 11.8, 15.6, 19.4$ a.u. The planes are chosen by maximum average density.

The fourth layer of Ge atoms sees little intrusion from foreign surface atoms and consequently remains solid. In fact, none of the atoms in the upper three layers penetrate within 2 a.u. of the initial plane of the fourth layer atoms. The increase in the magnitude of vibrations and resulting melting from penetration of surface atoms can also be understood within the context of the Lindemann Criterion.

5.6 Discussion

Although pseudopotential and finite-size errors cannot be ignored, the conclusions in this work are drawn from *comparisons* between similar structures that display very different molecular dynamics. The results in this work are subject to several possible sources of error that are easily identified but inevitable due to limitations on computational resources. To test whether these sources have any qualitative effect, we chose to examine the system with perhaps the most interesting dynamics, the Ge-monolayer coating on a GaAs surface, for any changes to our conclusion of induced

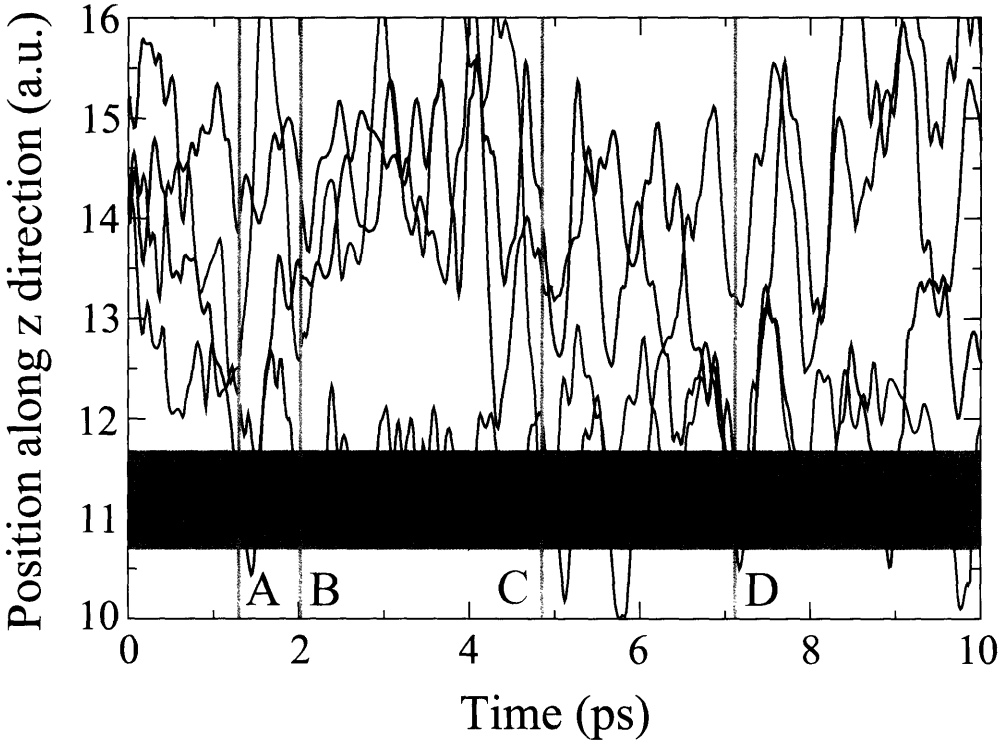

Figure 5-13: z-component of the ionic coordinates of the four Ge atoms in the surface monolayer coating a GaAs(110) crystal that penetrate past the plane marked in purple of the initial locations of the underlying layer of Ga and As atoms. The orange lines mark the times when atoms A, B, C, and D cross the plane $z = 11.25$a.u.

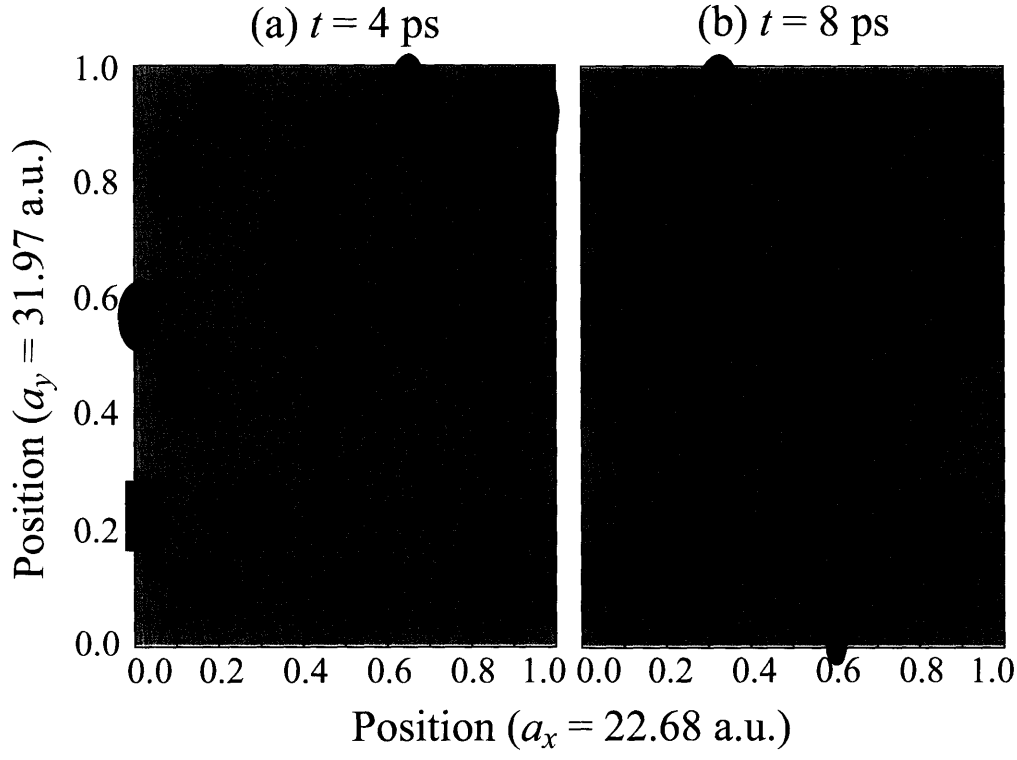

Figure 5-14: (x, y) positions of the Ga (diamonds) and As (ovals) atoms in the layer below the Ge coating of the GaAs(110)+Ge surface, as well as the Ge (rectangles) atoms A, B, C, and D marked in Fig. 5-13. In (a) [$t = 4$ ps], atom B has penetrated into the second layer ($z \approx 11.25$ a.u.) and disrupted the nearby covalent Ga-As in one row. In (b) [$t = 8$ ps], all four atoms have penetrated into the second layer and the distortion is widespread. The size of each atom is proportional to its penetration distance into the crystal (largest object is at $z \approx 10$a.u., smallest is at $z \approx 16$a.u.

surface melting.

An increase in the cutoff energy from 5 hartrees to 8 hartrees has little qualitative effect on the dynamics in Figs. 5-8 and 5-9. The diffusion constant D_2 remains $10 \times 10^{-6}\text{cm}^2/\text{s}$. A reduction in the time step to 8 fs also had little effect on the surface melting ($D_2 \rightarrow 9 \times 10^{-6}\text{cm}^2/\text{s}$). In addition, the finite size of each layer is likely to be most important along the direction with the most diffusion, the y-axis in Figs. 5-2 and 5-8. Doubling the lattice constant a_y from 32 to 64 a.u. did not appreciably affect the dynamics ($D_2 \rightarrow 8 \times 10^{-6}\text{cm}^2/\text{s}$).

The setup of our structures also possesses an intrinsic source of error, namely the frozen layer with terminating H atoms at the bottom surface. When the surface melts, the propagation of the liquid-solid interface quickly hits this artificial immobile bulk. Including additional layers (thereby increasing the supercell size in the z-direction) and replacing the immobility of the atoms with an average diffusivity or a continuum model will certainly have a quantitative effect on the diffusion, and it may be possible to extend our results to more precise predictions about the electronic properties of the melting transition very close to the melting point. However, the qualitative conclusions based on our simulations have been apparent from the dynamics of four free layers. In particular, it is clear from Fig. 5-3(a) that the frozen layer in the Ge(110) structure does not constrain or prevent melting in the atoms of the fourth layer above. Finally, we have assumed vacuum conditions in the volume above the surface, since it is likely that foreign atoms and molecules such as H_2O will desorb at high temperatures. We have performed simulations which predict the rapid desorption of H atoms from the surface at 1240 K. Thus, there is compelling evidence that a simple monolayer is sufficient to dramatically alter the melting behavior of a semiconductor surface.

To study the events which lead to melting in the dynamics of individual layers require a more accurate description of the electron density and a series of runs to test for the effects of thermal fluctuations. The free surface is the simplest defect to study, but larger supercells will also enable an analysis of the role of bulk defects in the melting process. Phillpot *et al.* have investigated the initiation of melting at internal

defects such as grain boundaries and dislocations. With further studies, we hope to answer whether the electronic structure of grain-boundary and dislocation-induced melting undergoes a similar transformation to the free surface. In addition, the enhancement of superheating by increasing the coating thickness and the degradation at higher temperatures require further simulations to improve the accuracy and reduce stochastic noise.

In conclusion, we have provided evidence that the key feature that determines the melting behavior of a crystal is the composition of the surface. Using the electronic structure and ion trajectories, we have described methods to identify the transition to a liquid state, and suggested the mechanism by which the melting occurs. We have demonstrated that it may be possible to achieve superheating in a Ge crystal coated with GaAs, a novel concept in semiconductors. In addition, we have shown that a Ge-monolayer coating can induce melting in an otherwise stable GaAs solid. There is every reason to think that these phenomena can also be observed at other interfaces between materials with different melting points. The ability to ultimately control the melting point of semiconductor heterostructures promises to be of great assistance in the design of high-temperature materials.

Chapter 6

Dynamic Structures in *Escherichia coli*: Spontaneous Formation of MinE Rings and MinD Polar Zones

Segments of this chapter previously appeared in: Huang, Meir, and Wingreen, Proc. Nat. Acad. Sci. USA ***100*** *12724-12728 (2003).*

In *E. coli*, two systems are known to regulate the placement of the division site, nucleoid occlusion [96, 99] and the Min proteins [16]. Both systems interfere with the formation of a ring of FtsZ protein that is believed to define the division site. The three Min proteins, MinC, D, and E, are required to prevent minicelling [16] -- asymmetric cell divisions which produce one small daughter cell, lacking a chromosome and hence nonviable. In contrast, overexpression of MinC results in filamentous growth [17], by inhibiting polymerization of FtsZ on the cell membrane [4], a necessary first step in cell division [5]. MinC is recruited to the membrane by MinD [34], which is only membrane-associated in its ATP bound form (MinD:ATP) [31]. Like MinC, MinE is naturally cytoplasmic and is recruited to the membrane by MinD:ATP [31].

In vivo observations of GFP fusions in living cells reveal spatial oscillations of the three Min proteins [74, 32, 24]. In each oscillation period, the cell's entire complement of MinD accumulates in the cell membrane in a "polar zone" at one end of the cell. This polar zone then shrinks toward the end of the cell, as a new accumulation forms

at the opposite pole. MinC follows the same pattern as MinD, and the two proteins form complexes on the membrane. In contrast, MinE forms a ring at the boundary of the MinD polar zone with some MinE dispersed throughout the polar zone. The MinE ring moves toward the end of the cell as the MinD polar zone shrinks. The oscillation period is approximately proportional to the amount of MinD and inversely proportional to the amount of MinE in the cell, with a minimum period of roughly 30 seconds [74]. Both MinD and MinE, but not MinC, are required for oscillations [74].

The average spatial distribution of the Min proteins naturally prevents minicelling without blocking normal cell division. The polar zones of MinD and MinC are believed to block FtsZ ring formation at the ends of the cell. At the same time, the concentrations of MinD and MinC remain low near the center of the cell, so an FtsZ ring can form there to establish the site of cell division.

Several models have been put forward to account for Min protein oscillations. All of these models successfully generate oscillations, but none can be meaningfully compared to *in vivo* observations. The model of Meinhardt and de Boer (MdB) [58] requires newly synthesized protein to form both the MinD polar zones and MinE ring, since the proteins disappear (degraded?) from the simulation upon dissociation from the membrane. However, Min oscillations have been observed to persist for at least 45 minutes after protein synthesis was blocked, demonstrating Min-protein stability. Furthermore, in order to obtain a MinE ring, the MdB model assumes *ad hoc* that MinE attaches preferentially to an intermediate concentration of MinD.

The model of Howard, Rutenberg, and de Vet (HRdV) [30] only produces oscillations if MinE is driven onto the membrane by cytoplasmic MinD, despite evidence that MinE is recruited to the membrane by membrane-associated MinD [31]. Moreover, the oscillations in the HRdV model have the opposite dependence of frequency on MinD concentration than is observed, and MinD forms a medial band which moves toward the end of the cell, contrary to the experimental observation that MinD forms directly as a polar zone. The model of Kruse [49] avoids *ad hoc* assumptions and produces a MinD polar zone by a MinD-concentration dependent slowing of MinD

diffusion on the membrane – a natural assumption in light of recent experimental evidence for MinD polymer formation [31]. However, the Kruse model requires unrealistically rapid membrane diffusion of MinD and fails to produce a MinE ring without *ad hoc* modification.

6.1 A model using only reported *in vitro* molecular interactions leads to oscillations

Here we show that a model including only the reported *in vitro* interactions of MinD and MinE can fully account for the Min oscillations, including formation of compact MinD polar zones and a MinE ring. The specific interactions are shown schematically in Fig. 1.The oscillations are driven by a cycle in which MinD:ATP first associates with the membrane, preferentially where other MinD:ATP is located. MinE then attaches to the MinD:ATP, activates ATP hydrolysis, and MinE and MinD:ADP re-enter the cytoplasm in a 1:1 ratio. Evidence for this cycle comes from *in vitro* experiments by Lutkenhaus and colleagues [31]. In particular, MinD bound to ATP reshapes spherical phospholipid vesicles into tubes by forming helical polymers, demonstrating self-association of membrane-bound MinD:ATP. Moreover, MinE co-sediments with MinD in the membrane, and activates hydrolysis and disassembly of MinD polymers [31]. Recent *in vivo* experiments by Rothfield and colleagues [81] also indicate formation of MinD polymers on the membrane.

6.2 Reaction-diffusion equations

The equations describing the time evolution of MinD and MinE concentrations in a cylindrical cell (see schematic of reaction cycle in Fig. 1) are:

$$\begin{aligned} \frac{\partial \rho_{D:\mathrm{ADP}}}{\partial t} &= \mathcal{D}_D \nabla^2 \rho_{D:\mathrm{ADP}} - \sigma_D^{\mathrm{ADP}\to\mathrm{ATP}} \rho_{D:\mathrm{ADP}} + \delta(r-R)\sigma_{de}\rho_{de} \qquad (6.1) \\ \frac{\partial \rho_{D:\mathrm{ATP}}}{\partial t} &= \mathcal{D}_D \nabla^2 \rho_{D:\mathrm{ATP}} + \sigma_D^{\mathrm{ADP}\to\mathrm{ATP}} \rho_{D:\mathrm{ADP}} \end{aligned}$$

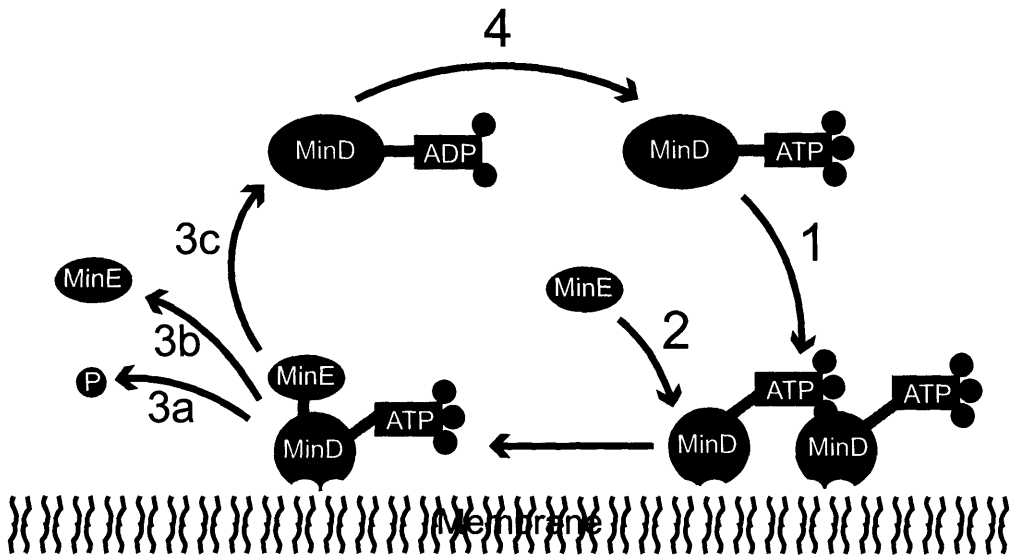

Figure 6-1: Model MinD1,E cycle driven by ATP hydrolysis. (**1**) Cytoplasmic MinD:ATP complex attaches to the membrane, preferentially where other MinD:ATP is bound. (**2**) MinE in the cytoplasm attaches to a membrane-associated MinD:ATP complex. (**3**) MinE activates ATP hydrolysis by MinD, breaking apart the complex, and releasing (a) phosphate, (b) MinE, and (c) MinD:ADP, into the cytoplasm. (**4**) MinD:ADP is converted back into MinD:ATP by nucleotide exchange. In wild-type cells, MinE is likely active as a homodimer [70].

$$-\delta(r-R)\left[\sigma_D+\sigma_{dD}(\rho_d+\rho_{de})\right]\rho_{D:\mathrm{ATP}} \tag{6.2}$$

$$\frac{\partial\rho_E}{\partial t} = \mathcal{D}_E\nabla^2\rho_E+\delta(r-R)\sigma_{de}\rho_{de}-\delta(r-R)\sigma_E\rho_d\rho_E \tag{6.3}$$

$$\frac{\partial\rho_d}{\partial t} = -\sigma_E\rho_d\rho_E(R)+\left[\sigma_D+\sigma_{dD}(\rho_d+\rho_{de})\right]\rho_{D:\mathrm{ATP}}(R) \tag{6.4}$$

$$\frac{\partial\rho_{de}}{\partial t} = -\sigma_{de}\rho_{de}+\sigma_E\rho_d\rho_E(R) \tag{6.5}$$

where $\rho_{D:\mathrm{ADP}}$, $\rho_{D:\mathrm{ATP}}$, ρ_E are the concentrations in the cytoplasm of MinD:ADP complexes, MinD:ATP complexes, and MinE, and ρ_d, ρ_{de} are the concentrations on the membrane of MinD:ATP complexes and MinE:MinD:ATP complexes. We have verified that introducing an intermediate free cytoplasmic MinD species, thereby converting the single rate constant $\sigma_D^{\mathrm{ADP}\to\mathrm{ATP}}$ into two sequential decay rates, does not introduce any significant changes.

The cell radius is $R=0.5\mu$m, and results are given for cells of length $L=4\mu$m and 10μm. The delta functions, $\delta(r-R)$, represent local exchange of proteins between membrane and cytoplasm; additional delta functions, $\delta(z)$ and $\delta(z-L)$, are implemented for the end caps of the cylinder. The total concentrations of MinD and MinE are $1000/\mu$m and $350/\mu$m, respectively (assuming MinE is active as a homodimer, this implies 700 monomers/μm) [80]. The diffusion constants are

$$\mathcal{D}_D=\mathcal{D}_E=2.5\mu\mathrm{m}^2/\mathrm{s},$$

as measured for the cytoplasmic diffusion of a maltose binding protein in the *E. coli* cytoplasm [19], and the reaction rates are

$$\sigma_D^{\mathrm{ADP}\to\ \mathrm{ATP}}=1/\mathrm{s},\ \sigma_D=0.025\mu\mathrm{m/s},\ \sigma_{dD}=0.0015\mu\mathrm{m}^3/\mathrm{s},\ \sigma_{de}=0.7/\mathrm{s},\ \sigma_E=0.093\mu\mathrm{m}^3/\mathrm{s},$$

unless otherwise indicated. We discretize and solve Eqs. 6.1-6.5 on a three-dimensional lattice in cylindrical coordinates, with grid spacing $dr=dz=0.05\mu$m.

6.3 Periodic oscillations with MinD polar zones and a MinE ring

The results of numerical integration in time of our model equations (cf. Fig. 1) for a 4 μm cylindrical cell are shown in Fig. 2. Periodic oscillations which are independent of initial conditions occur for a wide range of parameters. The oscillations have the same spatial character as those observed in experiment, including the formation and shrinkage of the MinD polar zones and the appearance of a MinE ring. These structures form spontaneously without special targets for MinD at the cell ends, without MinE-MinE interactions, and with no new protein synthesis. MinD:ATP and MinE dwell in one half of the cell membrane during a period of polar zone compaction, before a brief cytoplasmic burst results in rapid reformation of a new MinD polar zone and MinE ring at the opposite end of the cell. The bottom row of panels in Fig. 2 shows the time-averaged concentrations of MinD and MinE. The minimum for membrane-bound MinD:ATP occurs at the center of the cell.

The basic mechanism of the oscillations is that a typical MinD, once released from the membrane, diffuses farther in the cytoplasm than does a typical MinE before reattaching to the membrane. The delay before MinD becomes competent to reattach to the membrane stems from its need to release ADP and rebind ATP. This allows the formation of a new polar zone of MinD:ATP, while MinE progressively hydrolyzes the old polar zone.

But why does MinD:ATP accumulate at the far pole rather than reattaching uniformly throughout the cell? The reason is that MinD:ATP in the cytoplasm sticks rapidly to the old polar zone from which it was released. Indeed, a MinD protein typically recycles $\sim$ 4 times through the old polar zone in each half cycle, before finally lodging in the new polar zone. Each such recycling of MinD requires the hydrolysis of one molecule of ATP. The "stickiness" of the old polar zone creates a distribution of MinD:ATP in the cytoplasm that is peaked at the *opposite* end of the cell (Fig. 3). Thus MinD:ATP accumulates in a new polar zone, with a profile sharpened by the tendency of MinD:ATP in the membrane to self-associate [31].

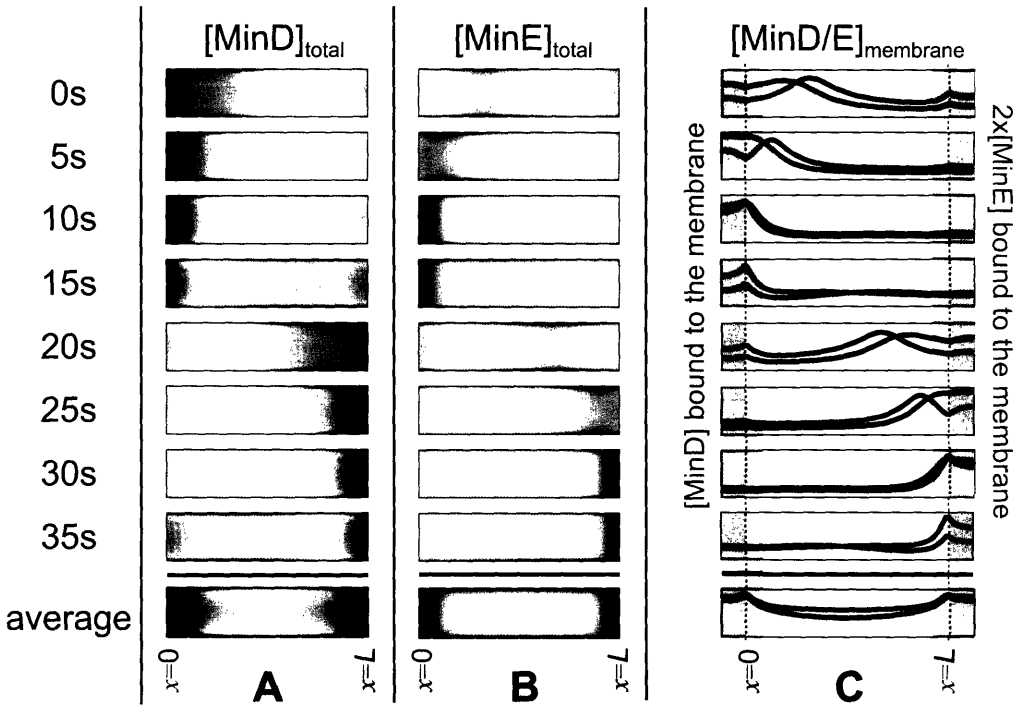

Figure 6-2: Time slices in 5s increments of one complete MinD,E oscillation in a 4 μm cell. To mimic experimental observations of GFP fluorescence, we show two-dimensional projections of the concentrations of MinD (**A**) and MinE (**B**) inside a three-dimensional cylindrical cell, with the concentrations assumed rotationally symmetric about the axis of the cylinder. In (**A**), the MinD polar zone shrinks toward the end of the cell, and reforms at the opposite pole. In (**B**), MinE forms a ring near the boundary of the MinD polar zone. Except during brief cytoplasmic-burst phases (15s, 35s) both MinD and MinE are primarily membrane-bound. (**C**) shows the membrane-associated concentrations, MinD:ATP in blue and MinE in red. The vertical dashed lines and gray shading indicate the caps of the cylindrical cell membrane. The final row shows the time average of each quantity over a complete cycle.

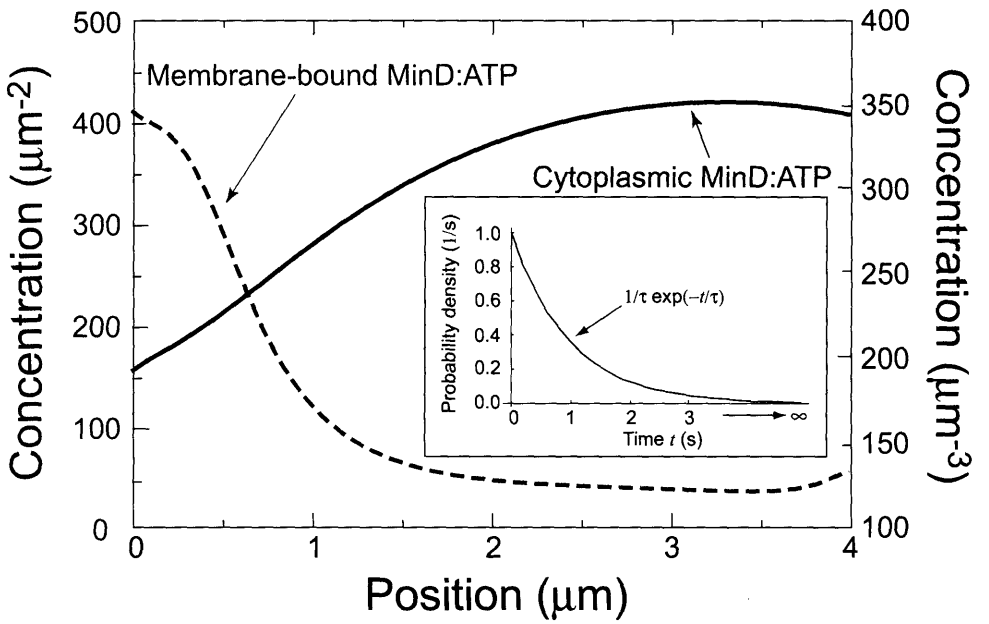

Figure 6-3: Concentration of ATP-bound MinD (MinD:ATP) in the cytoplasm corresponding to time $t = 5$s in Fig. 2. The distribution is peaked at the opposite end of the cell from the existing MinD:ATP polar zone, indicated by the peak of the dashed curve, leading to the accumulation of MinD:ATP in a new polar zone. Inset - waiting-time distribution for recovery of MinD:ATP, assuming a nucleotide-exchange rate $1/\tau = \sigma_D^{\mathrm{ADP}\to\mathrm{ATP}}$ of 1/s.

Proper formation of the new MinD:ATP polar zone requires that MinD have time to diffuse throughout the cytoplasm before rebinding ATP. The nucleotide exchange rate we use, $\sigma_D^{\mathrm{ADP}\to\mathrm{ATP}} = 1/\mathrm{s}$, is well within the observed range, which is known to span more than five orders-of-magnitude for guanine nucleotide exchange [53]. If the exchange rate is too large, cytoplasmic MinD:ATP reappears mainly near the old polar zone, eliminating the peaked distribution of cytoplasmic MinD:ATP (Fig. 3) which is responsible for the formation of a new polar zone. The delay of MinD:ATP recovery due to nucleotide exchange has been ignored in previous models.

Once MinE completes the hydrolysis of the old polar zone, it begins to diffuse through the cytoplasm. Since MinE sticks rapidly to available MinD:ATP in the membrane, most of the MinE attaches to the edge of the new MinD:ATP polar zone. This is the origin of the MinE ring. The subsequent movement of the MinE ring toward the end of the cell reflects release from the membrane, diffusion, and reattachment of individual MinE molecules (or homodimers). Since the diffusion length of MinE before reattaching is generally smaller than the $\sim 1\mu$m transverse dimension of the cell, it is important to model the oscillations in a fully three-dimensional cell, rather than in a one-dimensional approximation as employed in the MdB, HRdV, and Kruse models. We neglect membrane diffusion as too slow to affect the dynamics of the oscillations.

6.4 Oscillation period depends linearly on the ratio of MinD to MinE concentration

Figure 4 shows the period of oscillation for a range of protein concentrations. Consistent with experiment [74], the oscillation period is proportional to the total amount of MinD and inversely proportional to the total amount of MinE in the cell. The period is simply determined by the rate at which the MinE ring hydrolyzes the polar zone of MinD:ATP. This period increases almost linearly with the amount of MinD in the cell, and decreases inversely with both the amount of MinE and the hydroly-

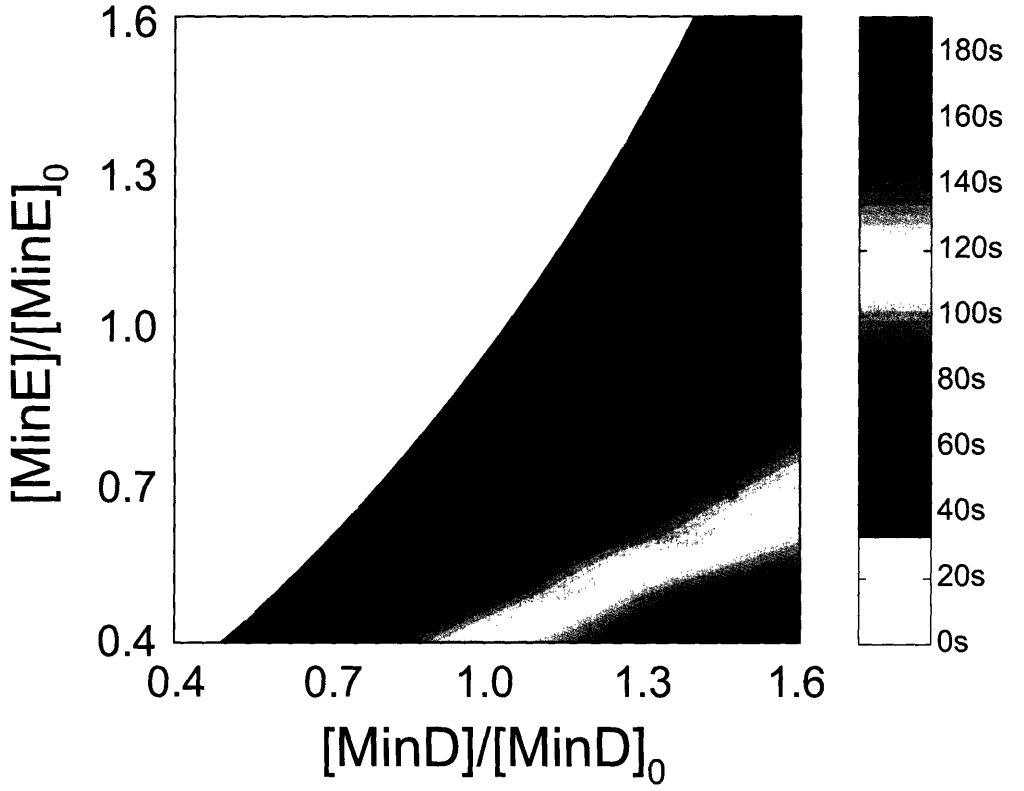

Figure 6-4: Dependence of the oscillation period on the average concentration of MinD and MinE in a 4μm cell. Wild-type values are $[\text{MinD}]_0 \sim 1000/\mu\text{m}$ and $[\text{MinE}]_0 \sim 350/\mu\text{m}$, respectively [80]. Isoperiod curves are shown in steps from 40s to 150s.

sis rate σ_{de}. We chose $\sigma_{de} = 0.7/\text{s}$ to match the observed wild-type period of ~ 40 seconds [74]. Varying the total amounts of MinD and MinE in the cell, we find a minimum oscillation period of $\sim$ 33s, also consistent with experiment [74]. Increasing the amount of MinE beyond this limit forces a majority of the MinD into the cytoplasm and eliminates oscillations. In contrast, decreasing the concentration of MinE results in slower and slower oscillations with no apparent limit, consistent with *in vivo* observations [74].

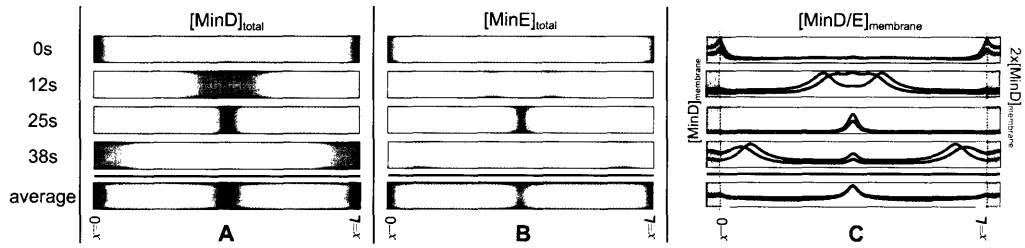

Figure 6-5: Time slices in 12.5s increments of one complete MinD,E oscillation in a 10 μm cell. (**A**),(**B**),(**C**) show the same quantities as in Fig. 2. The zebra-striped oscillation pattern now includes two half-wavelengths. The system exhibits two separate MinE rings and an alternation between two MinD polar zones and a central MinD tube. The final row shows the time average of each quantity over a complete cycle.

6.5 Filamentous cells have "doubled" oscillation patterns

A critical test of the model is the striking behavior of Min oscillations in long cells. Filamentous cells can be obtained using temperature-sensitive FtsZ mutants, which cannot undergo cell division at the non-permissive temperature. For cells longer than $\sim$ 10μm the number of wavelengths of Min oscillations present in the cell increases; zebra-striped cells with as many as 8 half-wavelengths have been observed [74]. Figure 5 shows the oscillation pattern obtained from our model for a 10 μm cell. Consistent with experimental observations, the oscillation pattern "doubles" – the oscillatory dynamics in each half of the cell mimics the dynamics of the normal 4 μm cell in Fig. 2. We find that this doubled oscillation pattern is stable for a three-dimensional cell, but collapses back to an undoubled pattern (Fig. 2) in the one-dimensional approximation. In addition, a nucleotide exchange rate of roughly 1/s or slower is necessary for stability of the doubled oscillation pattern. The bottom row of panels in Fig. 5 shows the time-averaged concentrations of MinD and MinE. The minima for membrane-bound MinD:ATP occur at 1/4 and 3/4 of the cell length, as observed by Gullbrand and Nordström for FtsZ ring placement in long cells [25]. Oscillations in a 20 μm cell closely correspond to a "doubled" 10 μm cell (not shown).

6.6 MinE "mutants": slow oscillations and no MinE ring formation

Another striking experimental observation is that cells with the wild-type $MinE^{1-88}$ protein replaced by the fragment $MinE^{1-53}$ display oscillations with a period of roughly 10 minutes with no detectable MinE ring, and with diffuse MinD polar zones [77]. Recent experiments with MinE mutants have correlated a weak or absent MinE ring with extended MinD polar zones and an increased minicelling probability [80]. Within our model, the oscillation period varies inversely with the hydrolysis rate σ_{de}, and ring formation depends on the attachment probability of MinE to available MinD:ATP in the membrane. In Fig. 6 we show oscillations of MinD and MinE with a reduced hydrolysis rate, $\sigma_{de} = 0.07/\text{s}$ which slows the oscillations, and a reduced MinE attachment coefficient $\sigma_E = 0.047\mu\text{m/s}$. With this value of σ_E, the MinE ring fails to form because MinE diffuses well into the new polar zone before reattaching to MinD:ATP (increasing the MinE diffusion constant has a similar effect). Importantly, this invasion of the MinD:ATP polar zone by MinE results in less accumulation of MinD:ATP and a more diffuse MinD:ATP polar zone, similar to experimental observations.

6.7 Discussion

Some aspects of Min protein oscillations are not captured by our minimal model. For example, the MinE ring is occasionally observed to reverse direction or "stutter" [80], likely reflecting the persistent presence of helical accumulations of MinD [81]. While the model cannot predict the fine structure of MinD polymerization [81], nevertheless, the agreement between model and experiment is close enough to indicate some fundamental properties of the real Min system. The model oscillations represent a limit cycle, that is, the same oscillation develops from any set of initial conditions. Moreover, the pattern of oscillation, particularly the formation of compact polar zones of MinD:ATP capped by a ring of MinE, is insensitive to fluctuations in the amounts

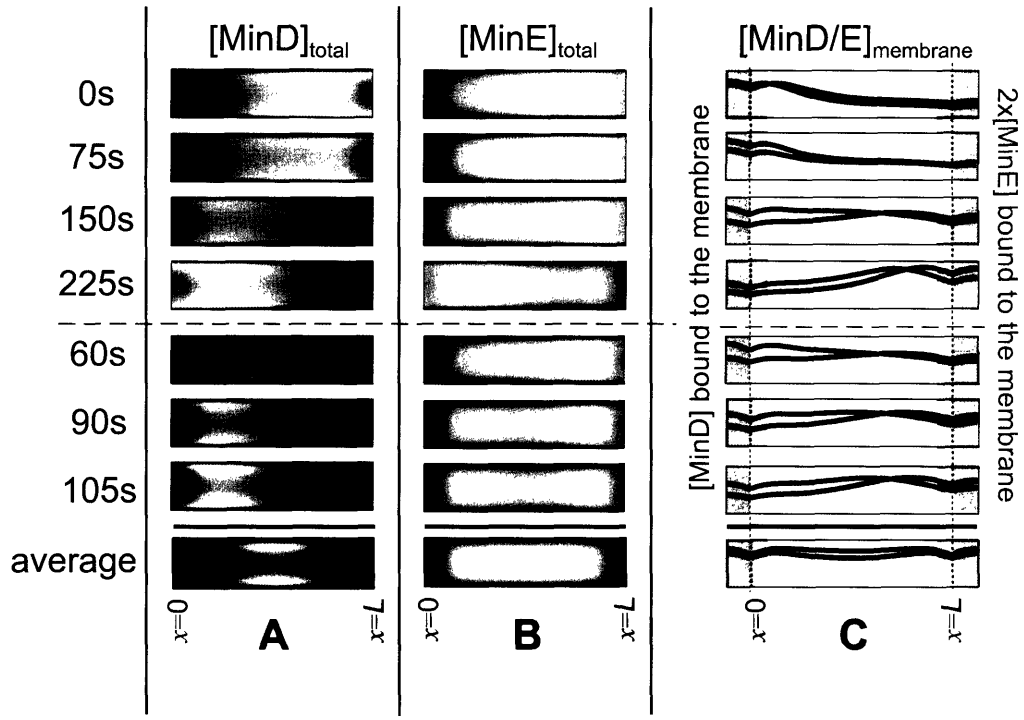

Figure 6-6: An oscillation period for a "MinE mutant" with reduced hydrolysis rate, $\sigma_{de} = 0.07$/s, and reduced MinE sticking coefficient, $\sigma_E = 0.047\mu$m/s. The upper half portrays time slices of half an oscillation cycle in 75s increments, while the lower half focuses on the time interval from 60s to 105s during which the MinE finishes hydrolyzing the old MinD polar zone, diffuses across the cell, and reforms on the opposite half. (**A**),(**B**), (**C**) show the same quantities as in Fig. 2. Note the long oscillation period and the suppression of a MinE ring.

of MinD and MinE. A linear-stability analysis around the uniform solution yields instability only for half-wavelengths greater than 2 μm. This minimum wavelength guarantees that oscillations can only develop in the cell's long dimension. Interestingly, the period of oscillations *is* sensitive to protein number fluctuations (Fig. 4), but periods of up to $\sim$ 120s [74] appear to yield a normal division phenotype.

Recent observations suggest a general role for protein oscillators in chromosome and plasmid partitioning [98, 18]. Nevertheless, it remains an open question why bacteria employ such oscillators. The Gram-positive bacterium *Bacillus subtilis* employs homologs to MinC and MinD to prevent minicelling. However, these proteins form static polar zones in *B. subtilis*. (*B. subtilis* also undergoes highly asymmetric cell division during sporulation.) In the absence of Min proteins in *E. coli*, nucleoid occlusion results in division sites either near the cell ends, resulting in minicelling, or medially, resulting in essentially normal divisions, but with considerably less division accuracy than in wild type [99]. In anucleate cells without nucleoid occlusion but with Min proteins, medial FtsZ ring placement is favored, but again with less accuracy than in wild type [99]. It is unknown whether Min protein oscillations alone can be sufficient for accurate FtsZ ring placement, or whether cooperation, and possibly direct interaction, between the Min system and nucleoid occlusion is required. In *B. subtilis*, the non-oscillatory MinCD homologs are *not* required for medial division accuracy [59]. One possible advantage of an oscillator for determining the cell center is that in each half cycle essentially the same amount of MinD protein accumulates in each polar zone. Thus, the time-averaged minimum of MinD, and hence the minimum of the division-site blocker MinC, will occur at the cell center independent of protein number fluctuations. Furthermore, recent indications [33] that MinC and MinE may competitively bind to MinD and that MinD forms dimers in the cytoplasm may enhance the FtsZ ring placement accuracy of the Min oscillator. Finally, the observation of FtsZ ring formation at the 1/4 and 3/4 points in long cells [25] very likely reflects the doubling of the Min-oscillation pattern. The multi-wavelength Min oscillations in long cells may play a role in proper fragmentation and reduce the likelihood of internal minicelling during recovery from filamentous growth induced by

the SOS response.

Chapter 7

Min-Protein Oscillations in Round Cells

Segments of this chapter have been submitted for publication in Physical Biology.

7.1 Introduction

In the rod-shaped bacterium *Escherichia coli*, the proteins MinC, MinD, and MinE are observed to oscillate from pole to pole [16, 74, 32, 24] every ~20 seconds [74]. Both MinD and MinE are required for oscillations [74]; MinC is not required, but is observed to oscillate because it forms complexes with MinD on the membrane [34]. MinD is an ATPase which associates to the membrane and forms helical polymers [81] there in its ATP-bound form (MinD:ATP) [31]. MinE is recruited to the membrane by MinD, where it activates hydrolysis of MinD:ATP resulting in dissociation of MinD from the membrane [31]. The oscillations concentrate MinCD complexes near the poles of the cell, where MinC blocks formation of a ring of FtsZ protein [4]. Formation of this FtsZ ring is required to initiate septum formation and cell division [5], so the net effect of the Min oscillations is to block cell divisions near the poles (minicelling). Placement of the FtsZ ring is also regulated by nucleoid occlusion [96, 99], a mechanism which blocks FtsZ ring formation in the vicinity of a nucleoid.

Homologs of the Min proteins have also been identified in round cells. In the

coccus *Neisseria gonorrhoeae*, loss of MinD_{Ng} results in abnormal cell division and morphology, and decreased cell viability [91]. MinD_{Ng} and MinE_{Ng} from *N. gonorrhoeae* were observed to oscillate when expressed in *E. coli* lacking its own MinD and MinE [71]. To date, there has been no direct observation of Min-protein oscillations in *N. gonorrhoeae* because of resolution limits associated with the small size of the bacteria, typically around 0.5μm in radius. [91]. However, in round *E. coli* cells, resulting from disruption of the *rodA* gene, both native MinD [10] and MinD_{Ng} from *N. gonorrhoeae* [71] have been observed to oscillate. Interestingly, while oscillations in wild-type *E. coli* display a ring of MinE protein, no MinE ring is observed in the round *rodA* cells. Taken together, the close homology of the *E. coli* and *N. gonorrhoeae* Min proteins, the complementation experiments, and the Min oscillations in round *E. coli* cells suggest that the Min proteins also form an oscillator in *N. gonorrhoeae* [71].

Here we demonstrate that a numerical model for Min-protein oscillations in rod-shaped cells [38] also leads to oscillations in round cells. The model is shown schematically in Fig. 1, and involves only *in vitro* observed interactions of MinD and MinE [31, 74]. In contrast to earlier modeling attempts [30, 58, 49], the model in Ref. [38] is fully three dimensional, so that extension to round cells is straightforward. The oscillations are driven by a cycle in which MinD:ATP binds to the membrane, preferentially at locations of high preexisting concentrations of MinD:ATP. MinE then attaches to the membrane-bound MinD:ATP, activates ATP hydrolysis, and MinE and MinD:ADP reenter the cytoplasm. In the cytoplasm, MinD:ADP undergoes nucleotide exchange to MinD:ATP to become competent to rebind the membrane.

7.2 Reaction-Diffusion Equations

The equations describing the time evolution of MinD and MinE concentrations in a spherical cell of radius R (see schematic of reaction cycle in Fig. 1) are:

$$\begin{aligned}
\frac{\partial \rho_{D:\text{ADP}}}{\partial t} &= \mathcal{D}_D \nabla^2 \rho_{D:\text{ADP}} - \sigma_D^{\text{ADP}\to\text{ATP}} \rho_{D:\text{ADP}} + \delta(r-R)\sigma_{de}\rho_{de} \qquad (7.1)\\
\frac{\partial \rho_{D:\text{ATP}}}{\partial t} &= \mathcal{D}_D \nabla^2 \rho_{D:\text{ATP}} + \sigma_D^{\text{ADP}\to\text{ATP}} \rho_{D:\text{ADP}}
\end{aligned}$$

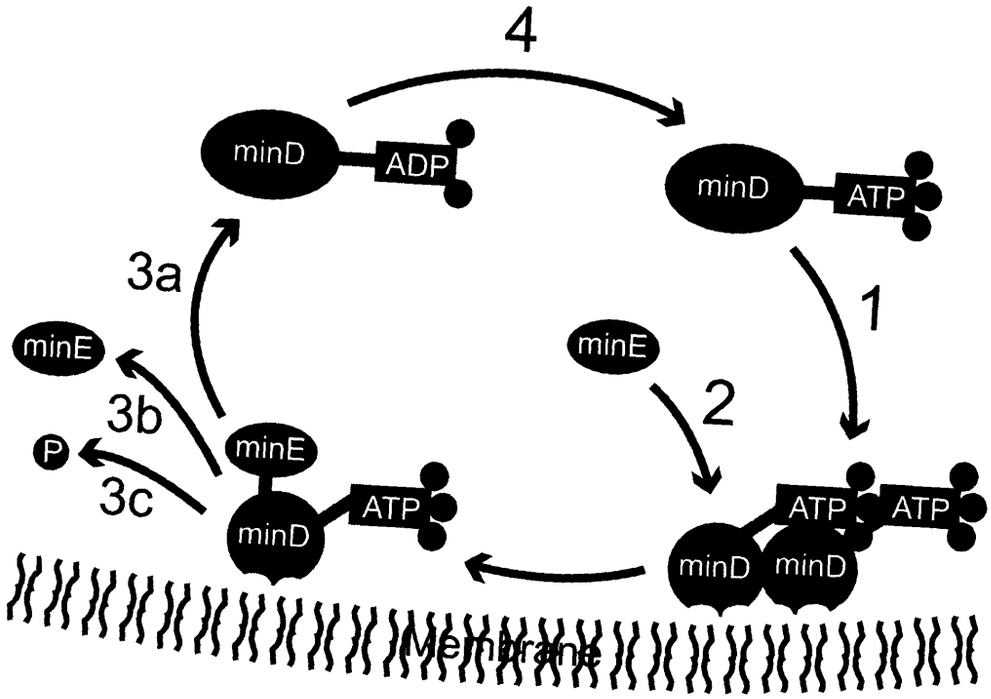

Figure 7-1: Model MinD,E cycle driven by ATP hydrolysis. (**1**) Cytoplasmic MinD:ATP complex attaches to the membrane, preferentially where other MinD:ATP is bound. (**2**) MinE in the cytoplasm attaches to a membrane-associated MinD:ATP complex. (**3**) MinE activates ATP hydrolysis by MinD, breaking apart the complex, and releasing (a) MinD:ADP, (b) MinE, and (c) phosphate into the cytoplasm. (**4**) MinD:ADP is converted back to MinD:ATP by nucleotide exchange. In wild-type cells, MinE is likely active as a homodimer [70].

$$-\delta(r-R)\left[\sigma_D+\sigma_{dD}(\rho_d+\rho_{de})\right]\rho_{D:\mathrm{ATP}} \tag{7.2}$$

$$\frac{\partial\rho_E}{\partial t} = \mathcal{D}_E\nabla^2\rho_E+\delta(r-R)\sigma_{de}\rho_{de}-\delta(r-R)\sigma_E\rho_d\rho_E \tag{7.3}$$

$$\frac{\partial\rho_d}{\partial t} = -\sigma_{de}\rho_{de}+\left[\sigma_D+\sigma_{dD}(\rho_d+\rho_{de})\right]\rho_{D:\mathrm{ATP}}(R) \tag{7.4}$$

$$\frac{\partial\rho_{de}}{\partial t} = -\sigma_{de}\rho_{de}+\sigma_E\rho_d\rho_E(R) \tag{7.5}$$

where $\rho_{D:\mathrm{ADP}}$, $\rho_{D:\mathrm{ATP}}$, ρ_E are the concentrations in the cytoplasm of MinD:ADP complexes, MinD:ATP complexes, and MinE, and ρ_d, ρ_{de} are the concentrations on the membrane of MinD:ATP and MinE:MinD:ATP complexes. Simulations with an intermediate free MinD species in the cytoplasm, thereby converting the single rate constant $\sigma_D^{\mathrm{ADP}\to\mathrm{ATP}}$ into two separate decay rates, do not show any significant differences.

The delta functions, $\delta(r-R)$, represent local exchange of proteins between membrane and cytoplasm. The total concentrations of MinD and MinE are $1250/\mu\mathrm{m}^3$ and $450/\mu\mathrm{m}^3$, respectively (assuming MinE is active as a homodimer, this implies 900 MinE monomers/$\mu\mathrm{m}^3$) [80]. The diffusion constants are

$$\mathcal{D}_D=\mathcal{D}_E=2.5\mu\mathrm{m}^2/\mathrm{s},$$

as measured for the cytoplasmic diffusion of a maltose binding protein in the *E. coli* cytoplasm [19], and the reaction rates are

$$\sigma_D^{\mathrm{ADP}\to\mathrm{ATP}}=1/\mathrm{s},\sigma_D=0.025/\mathrm{s},\sigma_{dD}=0.0015\mu\mathrm{m/s},\sigma_{de}=0.595/\mathrm{s},\sigma_E=0.2945\mu\mathrm{m/s}.$$

We have modified the MinE binding and hydrolysis rates from Ref. [38] to induce oscillations in cells of radius $R\sim 0.6\mu$m or larger. These parameters also produce oscillations in rod-shaped cells of length 4μm and radius 0.5μm. We discretize and solve Eqs. 7.1-7.5 on a three-dimensional lattice in spherical coordinates, with grid spacing $dr=0.03\mu$m, $d\theta=d\phi=\pi/20$.

7.3 Min-Protein Oscillations with No MinE Ring

The results of numerical integration in time of the model equations (cf. Fig. 1 and Eqs. 7.1-7.5) for a spherical cell with radius $R = 0.6\mu$m are shown in Fig. 2. In the spherical cell, independent of initial conditions, an oscillation develops which is rotationally symmetric about a "north-south" axis. The choice of oscillation axis does depend on initial conditions. The oscillation cycle has a period of 47s. As in cylindrical cells [38], zones of MinD:ATP grow from and shrink to the poles of the cell. However, in contrast to cylindrical cells, there is a notable absence of a MinE ring; rather, the MinE spreads throughout the entire MinD polar zone. The bottom row of panels in Fig. 2 shows the quantities in columns (a-c) averaged over one complete oscillation. The minimum for membrane-bound MinD:ATP occurs at the equator, indicating the most likely division site due to lower concentrations of the FtsZ ring-inhibitor MinC.

The basic mechanism for these oscillations is that a typical MinD, once released from the membrane, diffuses farther in the cytoplasm than a typical MinE before reattaching to the membrane. This allows formation of a new zone of MinD:ATP at the opposite pole, while MinE is at work progressively hydrolyzing the old polar zone. Growth of the new polar zone mirrors a gradient of MinD:ATP in the cytoplasm caused by the stickiness of the old polar zone [38]. The delay for nucleotide exchange allows MinD:ATP to diffuse away from the old polar zone and is essential to establishment of the cytoplasmic gradient. The absence of a MinE ring can be understood as purely an effect of geometry, as shown in Fig. 7-3. In either a round or a rod-shaped cell, a MinE that escapes the MinD:ATP zone at one pole of the cell is likely to rebind where it first contacts the opposite polar zone. In a round cell, this first contact is essentially equally likely to occur anywhere in the new polar zone. In a rod-shaped cell, however, the first contact is likely to occur near the medial edge of the new polar zone, resulting in a MinE ring as shown in Fig. 7-3(b).

Periodic oscillations occur for a wide range of model parameters. The period can be increased without limit by reducing the hydrolysis rate σ_e. Increasing σ_e

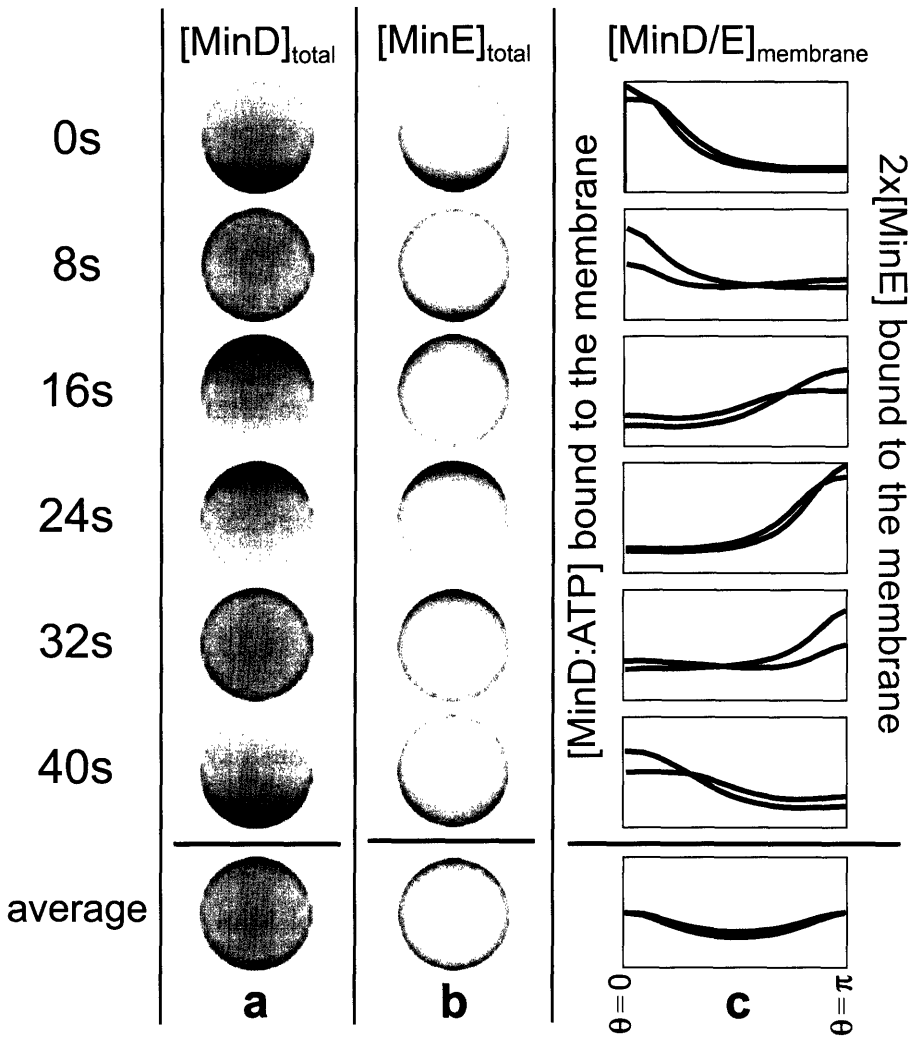

Figure 7-2: Time slices in 8s increments of one complete MinD,E oscillation in a spherical cell with radius $R = 0.6\mu$m. To mimic experimental observations of GFP fluorescence, we show two-dimensional projections onto the x-z plane (where the solution is rotationally symmetric about the z axis) of the concentrations of (**a**) MinD and (**b**) MinE. In (**a**), the MinD polar zone shrinks toward the south pole, and reforms at the north pole. In (**b**), the MinE also forms a polar zone which lags behind the MinD distribution. Note the absence of a MinE ring. Except during brief cytoplasmic-burst phases (8s, 32s for MinD) both MinD and MinE are primarily membrane bound. (**c**) shows the membrane-associated concentrations as a function of polar angle θ, MinD:ATP in blue and MinE in red.

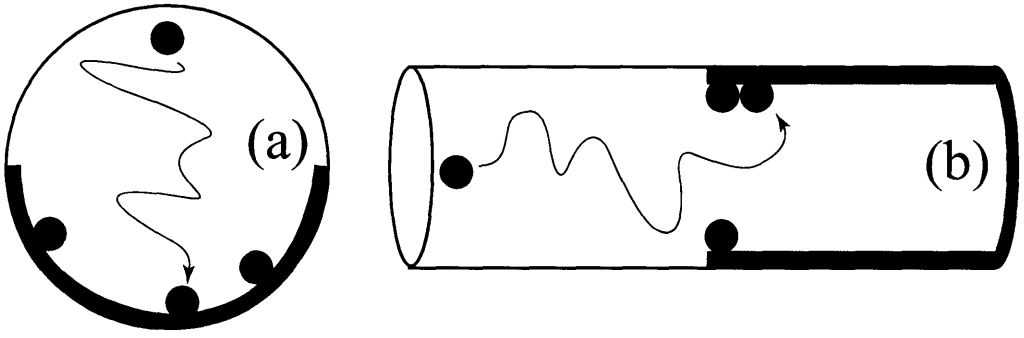

Figure 7-3: Geometric explanation for the absence of a MinE ring in round cells. (a) A MinE released from one pole of a round cell is approximately equally likely to bind anywhere within the new MinD zone at the opposite pole. (b) A MinE released from one pole of a rod-shaped cell is more likely to contact and bind to the nearest part of the new MinD polar zone. In rod-shaped cells, the result is a MinE "ring" – an accumulation of MinE near the medial edge of the new polar zone.

reduces the period down to a minimum of 43s, beyond which point most of the MinD is cytoplasmic and there are no oscillations. Oscillations also occur for a range of protein concentration with the period proportional to the ratio [MinD]/(σ_e[MinE]) [38], reflecting the time required for MinE to hydrolize a MinD:ATP polar zone.

7.4 Oscillations in Nearly Round Cells

Real cells are not perfectly round. In nearly round *rodA* mutants of *E. coli*, Min-protein oscillations were almost always observed to orient along the long axis [10]. Within our model, do the Min oscillations automatically select the long axis of a nearly round cell? In Fig. 7-4, we show the results of numerical integration in time of Eqs. 7.1-7.5 for an ellipsoidal cell with semi-major axis of length $R_1 = 0.63\mu$m and semi-minor axes of length $R_2 = 0.60\mu$m, starting from a random distribution of proteins. All diffusion constants, rate constants, and mean volume concentrations are the same as for the spherical cell in Fig. 2. Within a few oscillation periods, a stable oscillation is established precisely along the long axis of the ellipsoidal cell with a period of 49s.

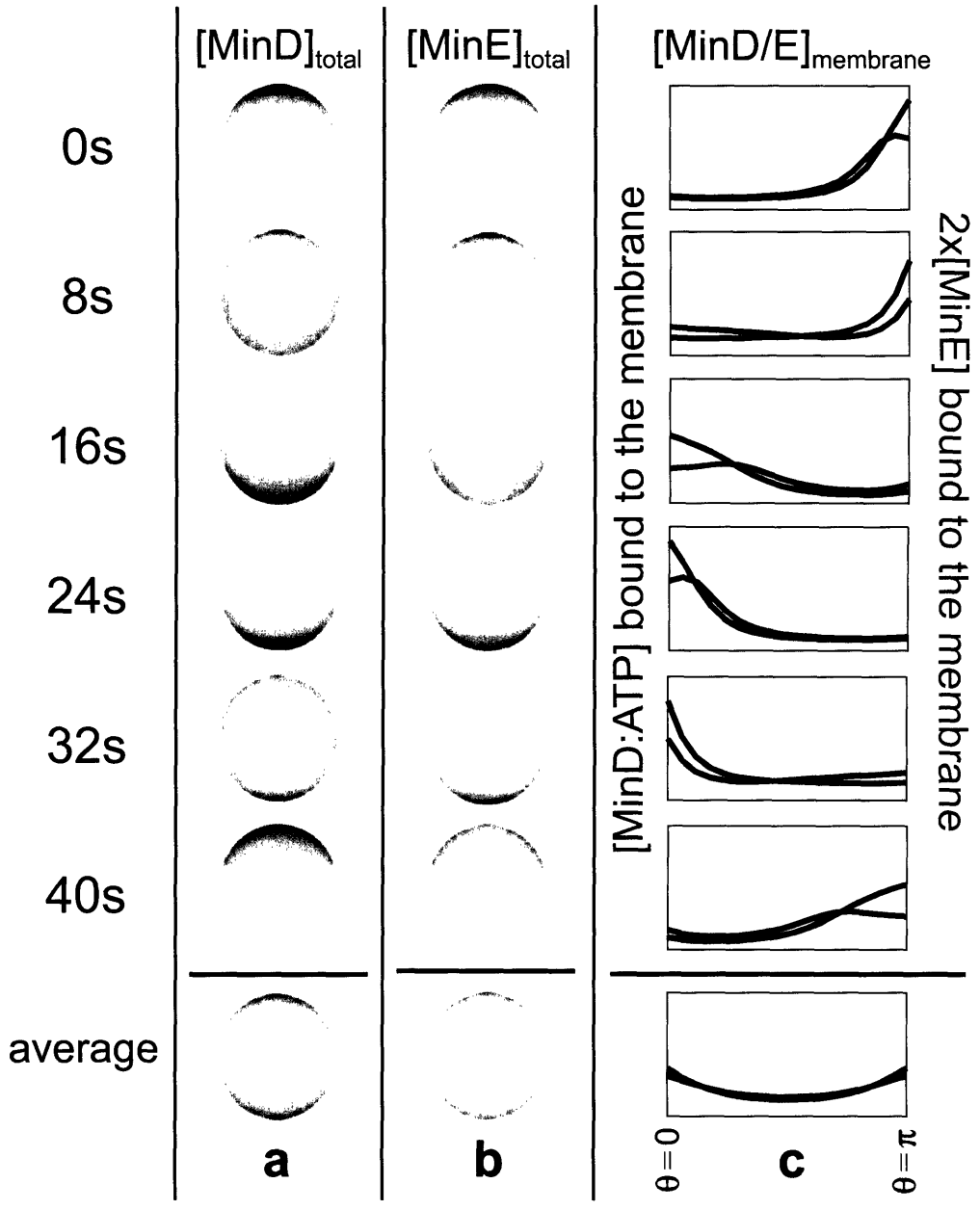

Figure 7-4: Time slices in 8s increments of one complete MinD,E oscillation in an ellipsoidal cell with semi-major axis of length $R_1 = 0.63\mu$m and semi-minor axes of length $R_2 = 0.60\mu$m. The quantities shown in (**a**), (**b**), and (**c**) are the same as in Fig. 7-2. Starting from a random initial distribution of proteins, pole-to-pole oscillations along the long axis become established within 3 oscillation periods.

7.5 Minimum Radius for Oscillations

We find that spherical cells below a minimum radius of $R_{\min} = 0.56\mu$m do not support oscillations. The non-oscillating solution of Eqs. 7.1-7.5 is spherically symmetric and has uniform concentrations of MinE and total MinD in the cytoplasm, which lacks sources or sinks of these proteins. However, the concentrations of the two species MinD:ADP and MinD:ATP can individually vary in the radial direction due to local exchange with the membrane. To analyze stability, we solve for the static concentrations: $\rho_i^0(r)$ where $i \in \mathcal{S} = \{D:\text{ADP}, D:\text{ATP}, E, d, de\}$, and then perturb about this static solution:

$$\rho_i^0(r) \rightarrow \rho_i^0(r)\left[1 + \varepsilon P_l(\cos\theta)\right], \tag{7.6}$$

where P_l is the lth Legendre polynomial, which is an eigenmode of the angular part of the diffusion equation in spherical coordinates with eigenvalue $\nu_l = l(l+1)/r^2$. In practice, we define the cytoplasmic densities on a grid of size $n_r = R/dr$:

$$\rho_i^0(r) \rightarrow \left(\rho_i^0\right)_j\Big|_{j=1}^{n_r}. \tag{7.7}$$

The perturbations in Eq. 7.6 evolve in time according to

$$\rho_i = \rho_i^0(r)\left[1 + e^{\Lambda t}P_l(\cos\theta)\right], \tag{7.8}$$

where the exponent $\Lambda \equiv \Lambda_1 + i\Lambda_2$, is an eigenvalue of the matrix $\mathbf{H} - \nu_l\mathbf{D}$. The Hessian matrix $\mathbf{H}$ is

$$\mathbf{H} = \left[\frac{\partial\left(\rho_i^0\right)_j}{\partial\left(\rho_k^0\right)_l}\right], \tag{7.9}$$

where i,k run over species in $\mathcal{S}$ and $j,l = 1$ if $i,k \in \{d,e\}$ and $j,l = 1,\ldots,n_r$ otherwise. The diffusion matrix is

$$\mathbf{D} = [D_{i,j}], \tag{7.10}$$

where $D_{i,j} \equiv \delta_{ij}\mathcal{D}_i$ and $\mathcal{D}_i$ is the diffusion constant of species ρ_i. Any mode with instability exponent $\Lambda_1 > 0$ represents an unstable (growing) perturbation about the static solution, and indicates that the solution of Eqs. 7.1-7.5 is oscillatory.

In Fig. 7-5(a), we plot the period of full nonlinear oscillations and in Fig. 7-5(b) the growth-rate exponent Λ_1 for the most unstable perturbation ($\sim \cos\theta$) from our linear-stability analysis. Both panels indicate a minimum radius for oscillations of $R_{\min} = 0.56\mu$m.

7.6 Discussion

Min-protein oscillations in rod-shaped *E. coli* cells block cell division at the poles, thereby preventing minicelling. The Min system may also contribute to the accuracy of cell division. Wild-type *E. coli* forms an FtsZ ring at the cell center with an accuracy better than $\pm 1\%$ of cell length, and this accuracy is lost in *min*$^-$ mutants [99]. An alternative view is that this loss of accuracy may simply reflect the onset of minicelling, rather than indicating a direct role for the Min system in division accuracy [56]. Division site placement in *E. coli* is regulated both by the Min-protein system and by nucleoid occlusion. [96] Certainly, in rod-shaped cells, Min oscillations and division accuracy, possibly based on nucleoid occlusion, could be independent, with both relying on the obvious long axis of the cell.

In round cells (cocci) such as *N. gonorrheoea* there is no obvious long axis. Nevertheless, cocci divide accurately along an equitorial plane into two daughter cells. If the Min proteins oscillate in *N. gonorrhoeae*, as experiments [91, 71, 10] and our numerical results suggest, then for the Min system to perform its usual function of blocking polar divisions requires that the poles and equator of the cell be consistently defined. This point is made in the cartoon in Fig. 7-6, with the schematic nucleoid segregation representing the full machinery of accurate cell division. The requirement for consistency between poles (MinCD accumulation zones) and equator (division plane) suggests that Min oscillations and division accuracy are directly coupled in *N. gonorrhoeae*, and hints that Min plays a similar direct role in the divi-

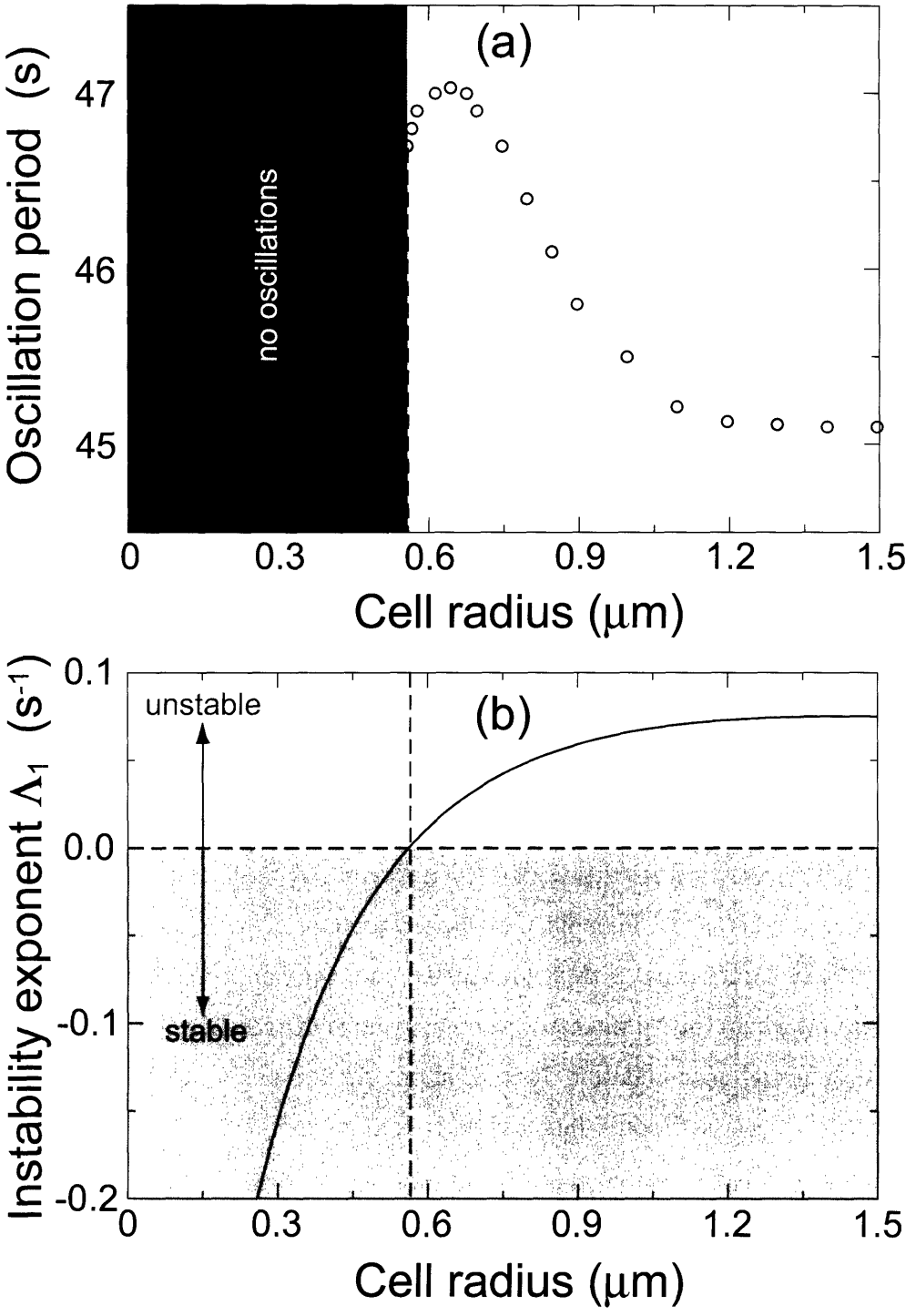

Figure 7-5: (a) The blue circles show the oscillation period as a function of cell radius. For cells with a radius smaller than $R_{\min} = 0.56\mu$m, no oscillations are possible. (b) Instability exponent Λ_1 as a function of cell radius for the most unstable perturbation ($\sim \cos\theta$) superimposed on a static, spherically symmetric solution.

sion process in *E. coli*. Experiments in round *E. coli* mutants [10] indicate that Min oscillations can pick out the long axis in slightly asymmetric cells. Our numerical simulations in ellipsoidal cells support this conclusion, and it is tempting to speculate that for cell division in *N. gonorrhoeae*, the Min oscillations actually define the poles and equator of the cell.

The ability of the Min oscillations to select the long axis of an ellipsoidal cell reflects the length dependence of the oscillatory instability. As shown in Fig. 7-5(b), the instability exponent Λ_1 increases with radius. Therefore, in asymmetric cells the oscillation pattern with the longest wavelength will become established. In the case of an ellipsoidal cell, the longest wavelength pattern corresponds to oscillations along the long axis of the cell. In both ellipsoidal and rod-shaped cells, a protein oscillator which prefers long wavelengths can provide a general mechanism for polar targeting of proteins.

In the most spherical of their round *rodA* mutant *E. coli* cells, Corbin *et al.* [10] observed rapid reorientation of Min oscillations of the MinD_{Ng} proteins. Ramirez-Arcos *et al.* [71] also observed uncoordinated oscillations in large *rodA E. coli* cells, but saw consistent pole-to-pole oscillations in smaller *rodA* cells. One possibility, suggested by our numerical results, is that the disorganized oscillation patterns observed in large cells reflects the instability of higher-order oscillation modes. Specifically, we found that larger cells, with radii $R > 0.85\mu$m, can support a symmetric oscillatory solution where the MinD distribution alternates between two polar distributions and an equatorial accumulation. Indeed, in our simulations we observe disorganized oscillations for cells with radii larger than $\sim 1.5\mu$m.

In large real cells, the existence of multiple instabilities is likely to amplify the effect of fluctuations. The specific movement of the MinD "pole" in large *rodA E. coli* cells is likely a consequence of these fluctuations, *i.e.* the first significant accumulation of MinD away from the old pole becomes the new pole. This nucleation effect is beyond the scope of our current mean-field model for Min oscillations. Even for rod-shaped cells, it remains an open question how fluctuations affect the stability and character of Min oscillations. The recent observation by Shih *et al.* [81] that MinD

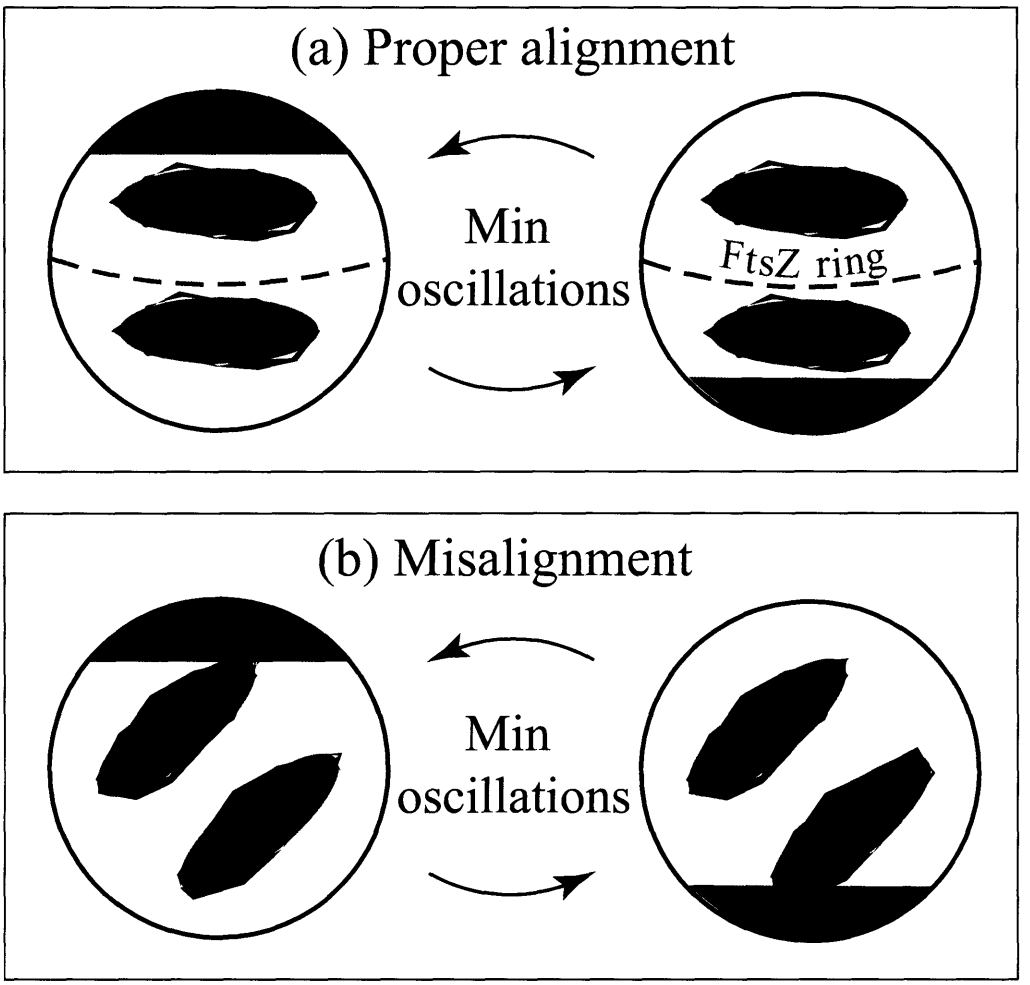

Figure 7-6: Schematic of pre-division round cell. (a) The alignment of the Min oscillations and nucleoid segregation ensures proper formation of the FtsZ ring. (b) Misalignment of the axial direction of the Min oscillations and the equator defined by the segregated nucleoids prohibits FtsZ-ring formation.

accumulates in helical polymers which remain present even at the "empty" pole may help explain why fluctuations do not lead to uncoordinated oscillations in wild-type cells.

Chapter 8

Pattern formation within *Escherichia coli*: diffusion, membrane attachment, and self-interaction of MinD molecules

Segments of this chapter have been submitted for publication in Physical Review Letters.

8.1 Introduction

Understanding how proteins are directed to specific locations within the cell is one of the key challenges of cellular biology. At the basic level, targeting of proteins to subcellular locations is governed by *physical processes*. A striking example is the system of Min proteins, which functions as an internal spatial oscillator in *E. coli*, and is necessary for accurate cell division [99]. The properties and interactions of the three Min proteins, MinC, D, and E, have been revealed by recent experiments [16, 17, 4, 5, 34, 31, 74, 32, 24, 81]. MinD is an ATPase – a protein which binds and hydrolyzes the nucleotide ATP to ADP. In its ATP-bound form, MinD associates with the inner membrane of the cell [31, 74], where it recruits cytoplasmic MinC [34] and

MinE [31] onto the membrane. Once on the membrane, MinE activates hydrolysis of ATP by MinD which results in MinD dissociating from the membrane. MinE and MinD together produce a spatial oscillator with a period of ~40 seconds [31, 74, 32, 24]. In each oscillation period, the majority of MinD molecules accumulate at one end of the cell forming a "polar zone". The MinD polar zone then shrinks toward the end of the cell and a new MinD polar zone forms at the opposite pole. MinE is observed to form a ring at the medial edge of the MinD polar zone [72]. The MinE ring moves along with the polar zone edge as the MinD polar zone shrinks toward the end of the cell. The dynamics of MinC follows that of MinD [73]. Complexes of MinC and MinD on the membrane block the formation of a ring of FtsZ protein [4], a necessary first step in determining the site of cell division [5]. The spatial oscillations of MinD and MinC from pole to pole thus ensure that an FtsZ ring does not form near the poles, so that cell division can only occur near midcell. Recently, several numerical models have been proposed to explain the oscillatory behavior [30, 58, 49, 29, 35]

One of the key emergent properties of the Min oscillations is the length scale for formation of a new MinD attachment zone. In filamentous cells (*i.e.* cells that grow but do not divide), several MinD zones are observed in a striped pattern with a characteristic length separating MinD attachment zones [74, 26]. In this work, we study the processes giving rise to new MinD attachment zones in the cell. Using a simple model, we demonstrate analytically that the length separating MinD zones depends on (*i*) the cytoplasmic diffusion coefficient and the nucleotide-exchange rate of MinD, and (*ii*) the rate of attachment of ATP-bound MinD to the membrane.

8.2 Model

Our 1D model is abstracted from the 3D numerical model of Ref. [35], which is based on measured properties of MinD and MinE and which reproduces the observed pattern in filamentous cells. Other models have also accounted for the oscillations of the Min proteins [58, 30, 49], including the striped pattern seen in filamentous cells. We begin by considering a fully formed "old" polar zone of ATP-bound MinD

(MinD:ATP) in one half of the cell. MinE activates the ATPase activity of MinD, giving rise to a source of cytoplasmic MinD:ADP. Subsequently, there are two stages leading up to reattachment of MinD to the membrane: (i) diffusion of each MinD:ADP until nucleotide exchange transforms it into MinD:ATP, and (ii) continued diffusion of the MinD:ATP until it attaches to the membrane (see inset to Fig. 8-1). The attachment rate of MinD:ATP increases with the local concentration of membrane-bound MinD due to polymerization; thus the old polar zone is much stickier than the bare membrane [35]. We approximate this situation by assuming that the old polar zone is infinitely sticky for cytoplasmic MinD:ATP. Our aim is to derive analytically the density of attachment $\rho(x)$ of MinD:ATP outside the old polar zone, in order to obtain the length scale of the new MinD attachment zone.

8.3 Filamentous cell, single source

We approximate a long, filamentous cell as an infinite 1D line. The old polar zone of MinD occupies $x < 0$, and bare membrane occupies $x > 0$ (see inset to Fig. 8-1). To model the effect of the MinE ring at the edge of the MinD polar zone, we consider that MinD:ADP dissociates from the membrane only at $x = 0$. After stage (i) – diffusion of MinD:ADP until nucleotide exchange – the probability density of each MinD:ATP is

$$P_1(x) = \int_0^\infty P_{\mathcal{D}}(x|t)Q_1(t)dt, \tag{8.1}$$

where $Q_1(t)$ is the waiting-time distribution for single-step nucleotide exchange with average waiting time τ_1,

$$Q_1(t) = \frac{1}{\tau_1}e^{-t/\tau_1}, \tag{8.2}$$

and $P_{\mathcal{D}}(x|t)$ is the distribution following diffusion in 1D for time t with diffusion coefficient $\mathcal{D}$,

$$P_{\mathcal{D}}(x|t) = \frac{1}{\sqrt{4\pi\mathcal{D}t}}\exp\left(-\frac{x^2}{4\mathcal{D}t}\right). \tag{8.3}$$

Substituting Eqs. 8.2 and 8.3 into Eq. 8.1 yields the initial distribution of MinD:ATP in the cytoplasm

$$P_1(x) = \frac{1}{2\sqrt{\mathcal{D}\tau_1}} \exp\left(-x\sqrt{\frac{1}{\mathcal{D}\tau_1}}\right). \tag{8.4}$$

During stage (ii) – diffusion of MinD:ATP until membrane attachment – we initially assume that the region of the old polar zone ($x < 0$) is infinitely sticky for MinD:ATP. Hence, if a MinD:ATP diffuses into $x < 0$, it will immediately reattach and become part of the old polar zone. Thus only those MinD:ATP molecules formed at $x > 0$ which *never* cross the origin in the course of cytoplasmic diffusion will attach to form the new zone. Given an initial position $x_0 > 0$ of a MinD:ATP, the probability that it diffuses to some $x > 0$ after time t is $P_{\mathcal{D}}(x - x_0|t)$. We define the probability that a MinD:ATP diffuses to some $x > 0$ after time t *without* crossing $x = 0$ by $P_2(x, x_0|t)$. The probability distribution $P_2(x, x_0|t)$ can be calculated using the continuum version of the Reflection Principle [22],

$$P_2(x, x_0|t) = P_{\mathcal{D}}(x - x_0|t) - P_{\mathcal{D}}(x + x_0|t). \tag{8.5}$$

The attachment density $\rho(x)$ for the bare membrane at $x > 0$ can now be obtained from

$$\rho(x) = \int_0^\infty dx_0 \int_0^\infty dt P_2(x, x_0|t) P_1(x_0) Q_2(t), \tag{8.6}$$

where $Q_2(t) = (1/\tau_2)\exp(-t/\tau_2)$ is the distribution of waiting times for membrane attachment with average waiting time τ_2. Integrating over t and x_0 in Eq. 8.6, we obtain (for $\tau_1 \neq \tau_2$)

$$\rho(x) = \frac{p_{\text{tot}}}{\sqrt{\mathcal{D}\tau_1} - \sqrt{\mathcal{D}\tau_2}} \left(e^{-x/\sqrt{\mathcal{D}\tau_1}} - e^{-x/\sqrt{\mathcal{D}\tau_2}}\right), \tag{8.7}$$

where the total probability of attachment to the bare membrane at $x > 0$ is

$$p_{\text{tot}} = \frac{\sqrt{\tau_1}}{2(\sqrt{\tau_1} + \sqrt{\tau_2})}. \tag{8.8}$$

In the limit $\tau_2 \to 0$, where the membrane is everywhere perfectly sticky for MinD:ATP,

Eq. 8.8 gives $p_{\rm tot} = 1/2$, as required by symmetry. In the opposite limit, $\tau_2 \gg \tau_1$, where sticking of MinD:ATP to the bare membrane at $x > 0$ is slow, only a small fraction, $p_{\rm tot} = \sqrt{\tau_1/4\tau_2}$, attach to the bare membrane.

The mean distance for attachment to the bare membrane is given by

$$\langle x \rangle = \frac{1}{p_{\rm tot}} \int_0^\infty x\rho(x)dx = \left(\sqrt{\mathcal{D}\tau_1} + \sqrt{\mathcal{D}\tau_2}\right), \tag{8.9}$$

precisely the sum of the independent diffusion lengths for processes with time scales τ_1 and τ_2. Another relevant length scale to characterize the new MinD:ATP zone is the position of the maximum in $\rho(x)$, which occurs at

$$x_{\rm max} = \frac{\sqrt{\mathcal{D}\tau_1\tau_2}}{2(\sqrt{\tau_2} - \sqrt{\tau_1})} \log\left(\frac{\tau_2}{\tau_1}\right). \tag{8.10}$$

We expect that polymerization of MinD:ATP on the membrane leads to an enhacement of the peak in the attachment density.

Note that for $\tau_1 = \tau_2 \equiv \tau$, we have

$$\rho(x) = xe^{-x/\sqrt{\mathcal{D}\tau}}/4\mathcal{D}\tau. \tag{8.11}$$

In this case, the average attachment distance is $\langle x \rangle = 2\sqrt{\mathcal{D}\tau}$ and the maximum occurs at $x_{\rm max} = \sqrt{\mathcal{D}\tau}/2$.

In Fig. 8-1, we plot the normalized MinD:ATP attachment density $\rho(x)/p_{\rm tot}$ from Eq. 8.7. At large distances, the profile decays exponentially as expected for a diffusive process (see Eq. 8.4). However, for a simple diffusive process we expect the profile to have a maximum at the source position *i.e.* at $x = 0$. In contrast, we find that the probability of attachment is *zero* at the edge of the old polar zone at $x = 0$. This "zero boundary condition" follows from the infinite stickiness of the old polar zone for MinD:ATP. Any MinD:ATP which forms near the old polar zone has a high probability of crossing into $x < 0$ and immediately reattaching as part of the old polar zone. Only those MinD:ATP which form sufficiently far from the old polar zone are likely to reattach as part of the new MinD:ATP attachment zone. The two

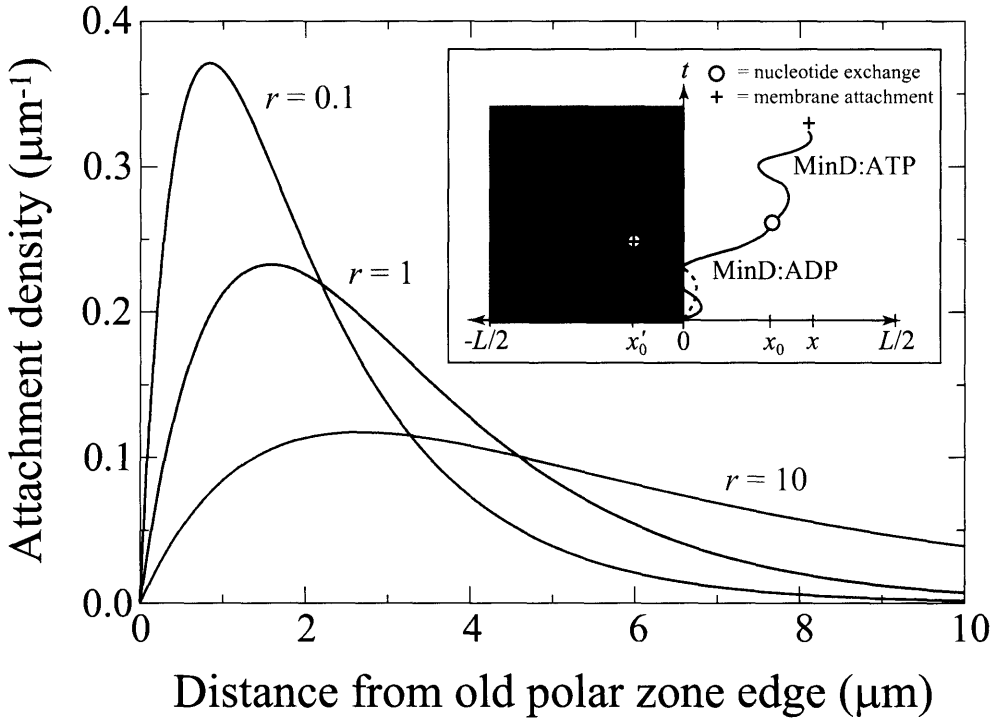

Figure 8-1: Normalized attachment density $\rho(x)/p_{\text{tot}}$ from Eq. 8.7 for different average attachment waiting times τ_2 from 0.1s to 10s, with the diffusion coefficient $\mathcal{D} = 2.5\mu\text{m}^2/\text{s}$ and average nucleotide-exchange waiting time $\tau_1 = 1\text{s}$ taken from Ref. [35] ($r = \tau_2/\tau_1$). Inset – cartoon of attachment processes. The solid blue line shows a MinD:ADP which diffuses to the position x_0 before undergoing nucleotide exchange. The resulting MinD:ATP then continues to diffuse until it attaches to the bare membrane at x, without ever crossing the edge of the old polar-zone at $x = 0$. In contrast, the dashed blue line shows a MinD:ADP which undergoes nucleotide exchange at the position x_0', where it immediately reattaches to the membrane in the old polar zone.

competing effects, the zero boundary condition at $x = 0$ and the exponential decay due to diffusion as indicated in Eq. 8.4, set the length scale for the formation of the new MinD:ATP attachment zone. In the model from Ref. [35], the time scale for sticking to a bare membrane is $\tau_2 \sim 10$s, giving $x_{\max} = 2.7\mu$m. This length scale agrees qualitatively with half the center-to-center distance ($\sim 3\mu$m) between neighboring MinD attachment zones as observed in Ref. [74].

8.4 Filamentous cell, distributed source

In the preceding analysis, to model the effect of the ring of MinE protein, the polar-zone edge at $x = 0$ was taken to be the only source of MinD:ADP. However, in experiments some MinE is observed throughout the MinD polar zone [72, 81], suggesting that cytoplasmic MinD:ADP is released throughout the old polar zone as well. What effect, if any, does this have on the length scale for formation of the new MinD attachment zone? Instead of assuming a single source for MinD:ADP at $x = 0$, we now consider a source with distribution $w(x_s)$, $x_s \leq 0$. This distributed source of MinD:ADP modifies Eq. 8.1:

$$P_1(x) \to \int_0^\infty dt \int_{-\infty}^0 dx_s w(x_s) P_{\mathcal{D}}\left(x - x_s|t\right) Q_1(t), \tag{8.12}$$

where x_s describes the position of the MinD:ADP when it leaves the membrane. Integrating over t, we find for $x > 0$,

$$P_1(x) = \frac{1}{2\sqrt{\mathcal{D}\tau_1}} e^{-x/\sqrt{\mathcal{D}\tau_1}} \left[\int_{-\infty}^0 dx_s w(x_s) e^{x_s/\sqrt{\mathcal{D}\tau_1}}\right]. \tag{8.13}$$

Comparing to Eq. 8.4, we see that a distributed source of MinD:ATP simply reduces $P_1(x)$ by the constant factor in square brackets. Therefore, the attachment density is the same as in Eq. 8.7, with p_{tot} reduced by the constant factor in square brackets. This leaves both $\langle x \rangle$ and $x_{\max}$ unchanged, so the length scale for formation of the new MinD attachment zone is unchanged.

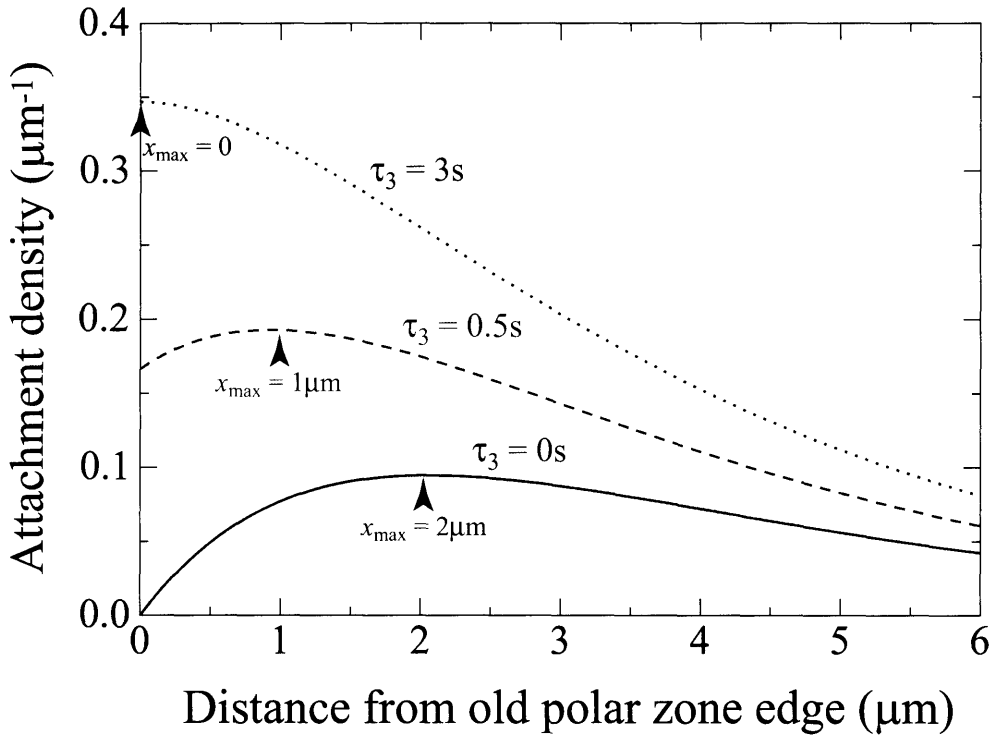

Figure 8-2: Normalized attachment density $f(x)/\tau_2$ from Eq. 8.19 for different binding times τ_3 in the old polar zone from 0s to 3s, with $\mathcal{D} = 2.5\mu\text{m}^2/\text{s}$, $\tau_1 = 1s$, and $\tau_2 = 3s$. Note the shift in the maximum toward $x = 0$ as $\tau_3 \rightarrow \tau_2$.

8.5 Finite polar zone attachment probability

Another assumption in our analysis so far is that the old MinD polar zone is infinitely sticky. How is the reattachment profile altered by relaxing this approximation to better reflect a realistic cell? We now consider the case where the attachment probability to the old polar zone is finite and characterized by a mean attachment time τ_3. To address this case, we introduce the quantities $\rho_c(x,t)$ and $\rho_m(x,t)$ denoting the density of cytoplasmic and membrane bound MinD:ATP, respectively, as a function of time. Our previous expression for the membrane attachment density $\rho(x)$ (Eq. 8.7) is then equivalent to $\rho_m(x, t \rightarrow \infty)$ for the case $\tau_3 = 0$ and $x > 0$. To avoid the difficult analytical task of integrating over *all* random walks in the cell, we instead utilize a Green's function approach.

Our system can now be described by the following set of reaction-diffusion equa-

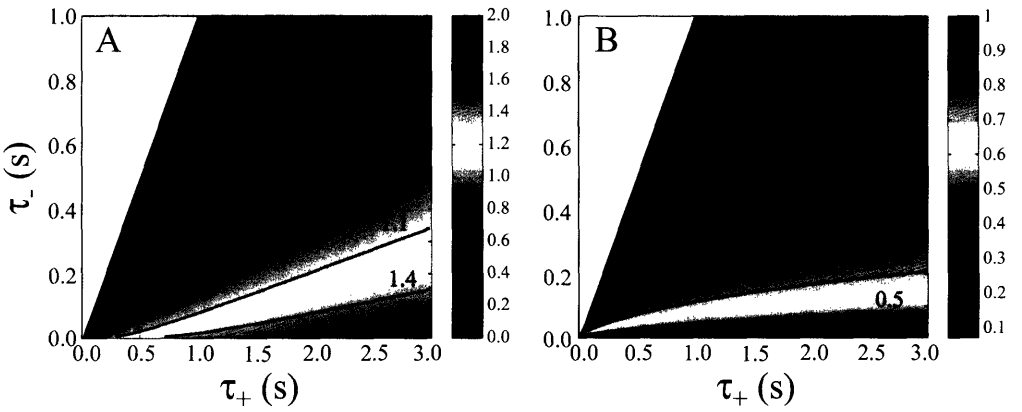

Figure 8-3: (a) The position of the maximum $\tilde{x}_{\max}$ as a function of $\tau_2 \in [0s, 3s]$ and $\tau_3 \in [0s, 1s]$ (see Eq. 8.20). (b) The ratio of densities $f(0)/f(\tilde{x}_{\max})$.

tions

$$\frac{\partial \rho_c(x,t)}{\partial t} = \mathcal{D}\frac{\partial^2 \rho_c(x,t)}{\partial x^2} - \frac{1}{\tau(x)}\rho_c(x) \tag{8.14}$$

$$\frac{\partial \rho_m(x,t)}{\partial t} = \frac{1}{\tau(x)}\rho_c(x,t) \tag{8.15}$$

where

$$\tau(x) = \begin{cases} \tau_2 & x > 0 \\ \tau_3 & x \leq 0 \end{cases} \tag{8.16}$$

We are interested in $\rho_m(x, t \to \infty)$ for $x > 0$ which, from integrating Eq. 8.15, is given by $\frac{1}{\tau_2}\int_0^\infty \rho_c(x,t)dt \equiv f(x)/\tau_2$. Similarly we set $\rho_m(x, t \to \infty) \equiv f(x)/\tau_3$ for $x \leq 0$. Then $f(x)$ so defined satisfies the equation

$$\rho_c(x,0) = D\frac{d^2 f}{dx^2} - \frac{1}{\tau(x)}f(x) \tag{8.17}$$

Note that $\rho_c(x,0)$ is the initial distribution of cytoplasmic MinD:ATP which is given by Eq. 8.4. We can now readily solve Eq. 8.17 for $f(x)$ in the regions $x \leq 0$ and $x > 0$ subject to the boundary conditions that $f(x)$ vanishes at $\pm\infty$ and $\rho_m(x = 0^-, t \to$

$\infty) = \rho_m(x = 0^+, t \to \infty)$, and the normalization condition on ρ,

$$\int_{-\infty}^{\infty} \frac{f(x)}{\tau(x)} dx = 1. \tag{8.18}$$

The new attachment profile in the presence of a finite binding rate in the new polar zone is

$$\rho(x) = \frac{f(x)}{\tau_2} = \frac{1}{2(\tau_1 - \tau_2)} \sqrt{\frac{1}{\mathcal{D}\tau_2}} \left(\sqrt{\tau_1 \tau_2} e^{-x/\sqrt{\mathcal{D}\tau_1}} - \frac{2\tau_2\sqrt{\tau_1\tau_3} + 2\tau_2\tau_3 + \tau_1\tau_2 - \tau_1\tau_3}{(\sqrt{\tau_1} + \sqrt{\tau_3})(\sqrt{\tau_2} + \sqrt{\tau_3})} e^{-x/\sqrt{\mathcal{D}\tau_2}} \right) \tag{8.19}$$

In Fig. 8-2, we plot $\rho(x)$ for $\tau_2 = 3s$ and three values of τ_3: 0s, 0.5s, and 3s. For $\tau_3 = 0s$, we again generate the infinite-stickiness profile in Eq. 8.7. For $\tau_3 = \tau_2 = 3s$, the profile is symmetric about $x = 0$, as expected since all binding rates are uniform. For $\tau_3 = 0.5s$, the profile lies somewhere in between, with a maximum located at 1μm - closer to the old polar zone than the value $x_{\text{eff}}|_{\tau_2 = 3s} = 2\mu$m from Eq. 8.10 - and a nonzero density at $x = 0$, since some of the MinD:ATP proteins now penetrate into $x < 0$ and still escape into the new polar zone to bind. The maximum occurs at

$$\tilde{x}_{\max} = \frac{\sqrt{\mathcal{D}\tau_1\tau_2}}{\sqrt{\tau_2} - \sqrt{\tau_1}} \log \left(\frac{\tau_2(\sqrt{\tau_1} + \sqrt{\tau_3})(\sqrt{\tau_2} + \sqrt{\tau_3})}{2\tau_2\sqrt{\tau_1\tau_3} + 2\tau_2\tau_3 - \tau_1\tau_3 + \tau_1\tau_2} \right), \tag{8.20}$$

which is less than $x_{\max}$ (see Eq. 8.10) for all nonzero τ_3. A second quantity of interest is the ratio of densities at the polar zone edge and the peak, $r = f(0)/f(x_{\max})$. This is a measure of the strength of selection for the new polar zone site.

In Fig. 8-3, we plot (a) $\tilde{x}_{\max}$ and (b) $f(0)/f(x_{\max})$ for $\tau_2 \in [0s, 3s]$ and $\tau_3 \in [0s, 1s]$, $\tau_3 < \tau_2$. Except for very small τ_3, $\tilde{x}_{\max}$ is a function only of the ratio τ_2/τ_3. The ratio r is $>\sim 0.5$ for practically all values of $(\tau_2, \tau_3$, demonstrating that the localization of the peak is significantly reduced by a finite binding rate.

There are several extensions to our approach which we feel would yield further insight into the processes involved. It would be interesting to consider the effect of low copy number of the MinD proteins as has been done in recent work by Howard

et al. [29]. It would also be interesting to consider if geometry can play a role in the process by altering attachment probabilities as has been proposed in the case of *B. subtilis* [28].

In summary, we have studied the processes that give rise to the length scale observed in cellular MinD attachment zones. Our analysis indicates that this length scale is an emergent property of the system which depends primarily on: (*i*) the rate of nucleotide exchange, (*ii*) the rate of membrane attachment and (*iii*) the diffusion constant for MinD. It is important to note that these are biochemical properties of MinD which can be fine tuned by evolution. Our analysis suggests that these parameters are tuned to block minicelling at the cell poles and at the same time to permit cell division at the center. Finally, we note that the Min system serves to illustrate the physical processes which underlie subcellular protein localization. While MinD is "targeted" to the cell poles, the mechanism is not based on recruitment by a biological target, but rather on a dynamical instability in the system.

Chapter 9

Final thoughts

The potential scope of future research in all areas of this thesis remains wide open. In Chapters 2-4, a relatively complete understanding of the band structure and field patterns of infinite two-dimensional polaritonic photonic crystals has been presented. A crucial feature is the large range of dispersion in polaritonic media, which provides a unique opportunity to explore extreme index contrasts and metallodielectric behavior in the same structure. The node switching and flux expulsion localization effects discussed in Chapters 2 and 3 suggest the possibility of exploring the behavior of nonlinear materials by sensitively controlling the electromagnetic intensity in particular regions of the crystal. It may also be possible to modify the polaritonic photonic crystal with negative effective permeability discussed in Chapter 4, by using a combination of polaritonic media or extending the crystal to three dimensions, thereby creating an effective left-handed material with negative permittivity that exhibits negative refraction. In addition, simulations involving three-dimensional crystals will help to connect theory with experiment, and may uncover novel localization phenomena.

The high degree of accuracy of the *ab-initio* approach used in Chapter 5 has allowed us to probe the electronic properties of the melting transition. We focused on melting from free surfaces and demonstrated the superheating and induced melting effects of single-layer coatings. There is also significant evidence that bulk semiconductors can melt from internal defects such as grain boundaries and dislocations [68]. The surface melting density functional simulations were the most computationally

exhausting tasks in this thesis, and as such they stand to benefit the most from increases in computational resources. Once larger supercell sizes are more tractable, comparisons between the melting mechanisms for different defects could be made using density functional molecular dynamics. Whether or not charge density disruption and the collapse of the band gap are universal signatures of melting is an open question whose answer will shed light on the fundamental nature of the phase transition from solid to liquid.

The reaction-diffusion model for Min-protein oscillations laid out in Chapters 6-8 has successfully reproduced most known phenomena in rod-shaped cells, and the predicted nucleotide exchange rate in *E. coli* cells has recently been verified to a high degree of accuracy. The stabilization of oscillations along the long axis in nearly round cells has important biological implications for the general role of oscillations for targeting and segregation in bacteria. Four primary questions about the Min-protein system remain unanswered at present. Recent experiments have shown that the MinD:ATP polymerizes into a helical pattern [81]. Such a detailed structure is unlikely to be reproduced by any of the existing mean-field models in Refs. [30, 58, 49] and Chapter 1-3. The low copy numbers of the Min proteins also suggest that extending the stochastic simulations in Chapter 8 to the full oscillatory cycle including MinE hydrolysis is crucial if we are to explain fluctuation effects such as the stuttering of the MinE ring [26, 29, 28]. Furthermore, the incredible accuracy of the division site selection in *E. coli* is still a mystery. Finally, other division-site selection regulatory mechanisms in organisms such as *Bacillus subtilis* could lead to a more general picture of the evolutionary development of complex spatial dynamics and targeted localization in bacterial protein networks.

Every answer to a question posed in this thesis has led to a Lernean proliferation of more complex unknowns. Nonetheless this work represents an important step towards a more complete understanding of the fundamental physical properties of the systems under review. For these, we have demonstrated that the existing theoretical and computational tools are flexible enough to be used both practically and efficiently to make verifiable predictions in the future. With advances in technology, the gap

between the complexity of simulations and experiment promises to shrink, revealing the bright road ahead for modelling of the development of structure in physics.

Bibliography

[1] N. G. Ainslie, J. D. Mackenzie, and D. Turnbull. Melting Kinetics of Quartz and Cristobalite. *J. Phys. Chem.*, 65:1718–1724, 1961.

[2] R. W. Alexander, G. S. Kovener, and R. J. Bell. Dispersion Curves for Surface Electromagnetic Waves with Damping. *Phys. Rev. Lett.*, 32(4):154–157, 1974.

[3] A. S. Barker, Jr. and R. Loudon. Response Functions in the Theory of Raman Scattering by Vibrational and Polariton Modes in Dielectric Crystals. *Rev. Mod. Phys.*, 44(1):18–47, 1972.

[4] E. Bi and J. Lutkenhaus. Cell division inhibitors SulA and MinCD prevent formation of the FtsZ ring. *J. Bacteriol.*, 175(4):1118–1125, 1993.

[5] E. Bi and Joe Lutkenhaus. FtsZ ring structure associated with division in *Escherichia coli*. *Nature*, 354:161–164, 1991.

[6] Peter Bienstman and Roel Baets. Optical modelling of photonic crystals and vcsels using eigenmode expansion and perfectly matched layers. *Opt. Quantum Electron.*, 33(4-5):327–341, 2001.

[7] L. L. Boyer. Theory of Melting Based on Lattice Instability. *Phase Transitions*, 5:1–48, 1985.

[8] Robert W. Cahn. Crystal defects and melting. *Nature*, 273:491–492, 1978.

[9] Robert W. Cahn. Melting and the surface. *Nature*, 323:668–669, 1986.

[10] Brian D. Corbin, Xuan-Chuan Yu, and William Margolin. Exploring intracellular space: function of the Min system in round-shaped *Escherichia coli*. *EMBO J.*, 21(8):1998–2008, 2002.

[11] R. L. Cormia, J. D. Mackenzie, and D. Turnbull. Kinetics of Melting and Crystallization of Phosphorus Pentoxide. *J. Appl. Phys.*, 34(8):2239–2244, 1963.

[12] R. M. J. Cotterill. The Physics of Melting. *J. Cryst. Growth*, 48:582–588, 1980.

[13] R. M. J. Cotterill, E. J. Jensen, and W. D. Kristensen. A molecular dynamics study of the melting of a three-dimensional crystal. *Phys. Lett. A*, 44:127–128, 1973.

[14] Timothy F. Crimmins, Nikolay S. Stoyanov, and Keith A. Nelson. Heterodyned impulsive stimulated Raman scattering of phonon-polaritons in $LiTaO_3$ and $LiNbO_3$. *J. Chem. Phys.*, 117(6):2882–2896, 2002.

[15] J. Daeges, H. Gleiter, and J. H. Perepezko. Superheating of Metal Crystals. *Phys. Lett. A*, 119(2):79–82, 1986.

[16] Piet A. J. de Boer, Robin E. Crossley, and Lawrence I. Rothfield. A Division Inhibitor and a Topological Specificity Factor Coded for by the Minicell Locus Determine Proper Placement of the Division Septum in *E. coli*. *Cell*, 56:641–649, 1989.

[17] Piet A. J. de Boer, Robin E. Crossley, and Lawrence I. Rothfield. Roles of MinC and MinD in the site-specific septation block mediated by the MinCDE system of *Escherichia coli*. *J. Bacteriol.*, 174:63–70, 1992.

[18] Gitte Ebersbach and Kenn Gerdes. The double *par* locus of virulence factor pB171: DNA segregation is correlated with oscillation of ParA. *Proc. Nat. Acad. Sci. USA*, 98(26):15078–15083, 2001.

[19] Michael B. Elowitz, Michael G. Surette, Pierre-Etienne Wolf, Jeffry B. Stock, and Stanislas Leibler. Protein Mobility in the Cytoplasm of *Escherichia coli*. *J. Bacteriol.*, 181(1):197–203, 1998.

[20] N. Eradat, A. Y. Sivachenko, M. E. Raikh, and Z. V. Vardeny. Evidence for braggoriton excitations in opal photonic crystals infiltrated with highly polarizable dyes. *Appl. Phys. Lett.*, 80(19):3491–3493, 2002.

[21] S. Fan, P. R. Villeneuve, J. D. Joannopoulos, M. J. Khan, C. Manolatou, and H. A. Haus. Theoretical analysis of channel drop tunneling processes. *Phys. Rev. B*, 59:15882–15892, 1999.

[22] William Feller. *An Introduction to Probability Theory and Its Applications.* Wiley, New York, 3rd edition, 1968.

[23] Y. Fink, J. N. Winn, S. Fan, C. Chen, J. Michel, J. D. Joannopoulos, and E. L. Thomas. A dielectric omnidirectional reflector. *Science*, 282:1679–1682, 1998.

[24] Xiaoli Fu, Yu-Ling Shih, Yan Zhang, and Lawrence I. Rothfield. The MinE ring required for proper placement of the division site is a mobile structure that changes its cellular location during the *Escherichia coli* division cycle. *Proc. Nat. Acad. Sci. USA*, 98(3):980–985, 2001.

[25] Björn Gullbrand and Kurt Nordström. FtsZ ring formation without subsequent cell division after replication runout in *Escherichia coli*. *Mol. Microbiol.*, 36(6):1349–1359, 2000.

[26] Cynthia A. Hale, Hand Meinhardt, and Piet A. J. de Boer. Dynamic localization cycle of the cell division regulator MinE in *Escherichia coli*. *EMBO J.*, 20(7):1563–1572, 2001.

[27] P. Hohenberg and W. Kohn. Inhomogeneous Electron Gas. *Phys. Rev.*, 136(3 B):B864, November 1964.

[28] M. Howard. A mechanism for polar protein localization in bacteria. *J. Mol. Biol.*, 335:655–663, 2004.

[29] M. Howard and A. Rutenberg. Pattern formation inside bacteria: fluctuations due to the low copy number of proteins. *Phys. Rev. Lett.*, 90:128102, 2003.

[30] Martin Howard, Andrew D. Rutenberg, and Simon de Vet. Dynamic Compartmentalization of Bacteria: Accurate Division in *E. coli*. *Phys. Rev. Lett.*, 87(27):278102, 2001.

[31] Zonglin Hu, Edward P. Gogol, and Joe Lutkenhaus. Dynamic assembly of MinD on phospholipid vesicles regulated by ATP and MinE. *Proc. Nat. Acad. Sci. USA*, 99(10):6761–6766, 2002.

[32] Zonglin Hu and Joe Lutkenhaus. Topological regulation of cell division in *Escherichia coli* involves rapid pole to pole oscillation of the division inhibitor MinC under the control of MinD and MinE. *Mol. Microbiol.*, 34(1):82–90, 1999.

[33] Zonglin Hu, Cristian Saez, and Joe Lutkenhaus. Recruitment of MinC, an Inhibitor of Z-Ring Formation, to the Membrane in *Escherichia coli*: Role of MinD and MinE. *J. Bacteriol.*, 185(1):196–203, 2003.

[34] Jian Huang, Chune Cao, and Joe Lutkenhaus. Interaction between FtsZ and Inhibitors of Cell Division. *J. Bacteriol.*, 178(17):5080–5085, 1996.

[35] Kerwyn Casey Huang, Peter Bienstman, John D. Joannopoulos, Keith A. Nelson, and Shanhui Fan. Field Expulsion and Reconfiguration in Polaritonic Photonic Crystals. *Phys. Rev. Lett.*, 90(19):196402, 2003.

[36] Kerwyn Casey Huang, Peter Bienstman, John D. Joannopoulos, Keith A. Nelson, and Shanhui Fan. Phonon-Polariton Excitations in Photonic Crystals. *Phys. Rev. B*, 68(7):075209, 2003.

[37] Kerwyn Casey Huang, Elefterios Lidorikis, Xunya Jiang, John D. Joannopoulos, Keith A. Nelson, Peter Bienstman, and Shanhui Fan. The nature of lossy Bloch states in polaritonic photonic crystals. *Phys. Rev. B*, 69:195111, 2004.

[38] Kerwyn Casey Huang, Yigal Meir, and Ned Wingreen. Dynamic structures in *Escherichia coli*: Spontaneous formation of MinE rings and MinD polar zones. *Proc. Nat. Acad. Sci. USA*, 100(22):12724–12728, 2003.

[39] Sohrab Ismail-Beigi and T. A. Arias. New Algebraic Formulation of Density Functional Calculation. *Computer Physics Communications*, 128:1–45, 2000.

[40] Xunya Jiang and C. M. Soukoulis. Time Dependent Theory for Random Lasers. *Phys. Rev. Lett.*, 85(1):70–73, 2000.

[41] J. D. Joannopoulos, R. D. Meade, and J. N. Winn. *Photonic Crystals: Molding the Flow of Light.* Princeton University Press, Princeton, NJ, 1995.

[42] Sajeev John. Strong Localization of Photons in Certain Disordered Dielectric Superlattices. *Phys. Rev. Lett.*, 58(23):2486–2490, 1987.

[43] S. G. Johnson, P. R. Villeneuve, S. Fan, and J. D. Joannopoulos. Linear waveguides in photonic-crystal slabs. *Phys. Rev. B*, 62:8212–8222, 2000.

[44] CAMFR is freely available from http://camfr.sourceforge.net.

[45] C. Kittel. *Introduction to Solid State Physics.* John Wiley & Sons Inc., New York, seventh edition, 1996.

[46] Charles Kittel. *Introduction to Solid State Physics.* John Wiley & Sons, Inc., New York, NY, seventh edition, 1966.

[47] W. Kohn and L. J. Sham. Self-Consistent Equations Including Exchange and Correlation Effects. *Phys. Rev.*, 140(4 A):A 1133, November 1965.

[48] A. A. Krokhin and P. Halevi. Influence of weak dissipation on the photonic band structure of periodic composites. *Phys. Rev. B*, 53(3):1205–1214, 1996.

[49] Karsten Kruse. A Dynamic Model for Determining the Middle of *Escherichia coli*. *Biophys. J.*, 82:618–627, 2002.

[50] Karl S. Kunz and Raymond J. Luebbers. *The Finite Difference Time Domain Method for Electromagnetics.* CRC Press LLC, Boca Raton, FL, 1993.

[51] V. Kuzmiak, A. A. Maradudin, and A. R. McGurn. Photonic band structures of two-dimensional systems fabricated from rods of a cubic polar crystal. *Phys. Rev. B*, 55(7):4298–4311, 1997.

[52] V. Kuzmiak, A. A. Maradudin, and F. Pincemin. Photonic band structures of two-dimensional systems containing metallic components. *Phys. Rev. B*, 50(23):16835–16843, 1994.

[53] Christian Lenzen, Robbert H. Cool, Heino Prinz, Jürgen Kuhlmann, and Alfred Wittinghofer. Kinetic Analysis by Fluorescence of the Interaction between Ras and the Catalytic Domain of the Guanine Nucleotide Exchange Factor $Cdc25^{Mm}$. *Biochemistry*, 37:7420–7430, 1998.

[54] E. Lidorikis, M. M. Sigalas, E. N. Economou, and C. M. Soukoulis. Tight-Binding Parameterization for Photonic Band Gap Materials. *Phys. Rev. Lett.*, 81(7):1405–1408, 1998.

[55] Joe Lutkenhaus. private communication.

[56] William Margolin. private communication.

[57] E.G. McRae. *Surface Science*, 11:479, 1968.

[58] Hans Meinhardt and Piet A. J. de Boer. Pattern formation in *Escherichia coli*: A model for the pole-to-pole oscillations of Min proteins and the localization of the division site. *Proc. Nat. Acad. Sci. USA*, 98(25):14202–14207, 2001.

[59] Margaret D. Migocki, Marcelle K. Freeman, R. Gerry Wake, and Elizabeth J. Harry. The Min system is not required for precise placement of the midcell Z ring in *Bacillus subtilis*. *EMBO Rep.*, 3(12):1163–1167, 2002.

[60] A. Modinos, N. Stefanou, and V. Yannopapas. Applications of the layer-KKR method to photonic crystals. *Optics Express*, 8(3):197–202, 2001.

[61] Esteban Moreno, Daniel Erni, and Christian Hafner. Band structure computations of metallic photonic crystals with the multiple multipole method. *Phys. Rev. B*, 65(15):155120–1–155120–10, 2002.

[62] N. A. Nicorovici, A. A. Asatryan, L. C. Botten, K. Busch, R. C. McPhedran, C. M. de Sterke, P. A. Robinson, G. H. Smith, D. R. McKenzie, and A. R. Parker. Multipole methods for photonic crystal calculations. In C. M. Soukoulis, editor, Conference on Photonic Crystals and Light Localization in the 21st Century, *Vol. 563 of NATO Science Series C: Mathematical and Physics Sciences*, pages 527–534, Dordrecht, 2001. Kluwer.

[63] Stephen O'Brien and John B. Pendry. Photonic band-gap effects and magnetic activity in dielectric composites. *J. Phys.: Condens. Matter*, 14:4035–4044, 2002.

[64] T. Ochiai and K. Sakoda. Nearly free-photon approximation for two-dimensional photonic crystal slabs. *Phys. Rev. B*, 64(4):045108, 2001.

[65] M. C. Payne, M. P. Teter, D. C. Allan, T. A. Arias, and J. D. Joannopoulos. Iterative Minimization Techniques for *ab initio* Total-Energy Calculations: Molecular Dynamics and Conjugate Gradients. *Rev. Mod. Phys.*, 64(4):1045, October 1992.

[66] J. B. Pendry, A. J. Holden, D. J. Robbins, and W. J. Stewart. Magnetism from Conductors and Enhanced Nonlinear Phenomena. *IEEE Transactions on Microwave Theory and Techniques*, 1999.

[67] J. B. Pendry, A. J. Holden, W. J. Stewart, and I. Youngs. Extremely Low Frequency Plasmons in Metallic Mesostructures. *Phys. Rev. Lett.*, 76(25):4773–4776, 1996.

[68] S. R. Phillpot, J. F. Lutsko, D. Wolf, and S. Yip. Molecular-dynamics study of lattice-defect-nucleated melting in silicon. *Phys. Rev. B*, 40(5):2831–2840, 1989.

[69] Simon R. Phillpot, Sidney Yip, and Dieter Wolf. How Do Crystals Melt? *Computers in Physics*, pages 20–31, Nov/Dec 1989.

[70] Sébastien Pichoff, Benedikt Vollrath, Christian Touriol, and Jean-Pierre Bouché. Deletion analysis of gene *minE* which encodes the topological specificity factor of cell division in *Escherichia coli*. *Mol. Microbiol.*, 18(2):321–329, 1995.

[71] Sandra Ramirez-Arcos, Jason Szeto, Jo-Anne R. Dillon, and William Margolin. Conservation of dynamic localization among MinD and MinE orthologues: oscillation of *Neisseria gonorrhoeae* proteins in *Escherichia coli*. *Mol. Microbiol.*, 46(2):493–504, 2002.

[72] David M. Raskin and Piet A. J. de Boer. The MinE Ring: An FtsZ-Independent Cell Structure Required for Selection of the Correct Division Site in *E. coli*. *Cell*, 91:685–694, 1997.

[73] David M. Raskin and Piet A. J. de Boer. MinDE-Dependent Pole-to-Pole Oscillation of Division Inhibitor MinC in *Escherichia coli*. *J. Bacteriol.*, 181(20):6419–6424, 1999.

[74] David M. Raskin and Piet A. J. de Boer. Rapid pole-to-pole oscillation of a protein required for directing division to the middle of *Escherichia coli*. *Proc. Nat. Acad. Sci. USA*, 96:4971–4976, 1999.

[75] W. M. Robertson, G. Arjavalingam, R. D. Meade, K. D. Brommer, A. M. Rappe, and J. D. Joannopoulos. Measurement of Photonic Band Structure in a Two-Dimensional Periodic Dielectric Array. *Phys. Rev. Lett.*, 68(13):2023–2026, 1992.

[76] C. J. Rossouw and S. E. Donnelly. Superheating of small solid-argon bubbles in aluminum. *Phys. Rev. Lett.*, 55:2960–2963, 1985.

[77] S. L. Rowland, X. Fu, M. A. Sayed, Y. Zhang, W. R. Cook, and L. I. Rothfield. Membrane Redistribution of the *Escherichia coli* minD protein Induced by MinE. *J. Bacteriol.*, 182(3):613–619, 2000.

[78] M. Schall, H. Helm, and S. R. Keiding. Far infrared properties of electro-optic crystals measured by THz time-domain spectroscopy. *International Journal of Infrared and Millimeter Waves*, 20(4):595–604, 1999.

[79] R. A. Shelby, D. R. Smith, S. C. Nemat-Nasser, and S. Schultz. Microwave transmission through a two-dimensional, isotropic, left-handed metamaterial. *Appl. Phys. Lett.*, 78(4):489–491, 2001.

[80] Yu-Ling Shih, Xiaoli Fu, Glenn F. King, Trung Le, and Lawrence Rothfield. Division site placement in *E. coli*: mutations that prevent formation of the MinE ring lead to loss of the normal midcell arrest of growth of polar MinD membrane domains. *EMBO J.*, 21(13):3347–3357, 2002.

[81] Yu-Ling Shih, Trung Le, and Lawrence Rothfield. Division site selection in *Escherichia coli* involves dynamic redistribution of Min proteins within coiled structures that extend between the two cell poles. *Proc. Nat. Acad. Sci. USA*, 100, 2003.

[82] G. Shvets. Photonic approach to making a material with a negative index of refraction. *Phys. Rev. B*, 67(3):035109, 2003.

[83] M. Sigalas, C. M. Soukoulis, E. N. Economou, C. T. Chan, and K. M. Ho. Photonic band gaps and defects in two dimensions: Studies of the transmission coefficient. *Phys. Rev. B*, 48(19):14121–14126, 1993.

[84] M. M. Sigalas, C. M. Soukoulis, C. T. Chan, and K. M. Ho. Electromagnetic-wave propagation through dispersive and absorptive photonic-band-gap materials. *Phys. Rev. B*, 49(16):11080–11087, 1994.

[85] A. Yu. Sivachenko, M. E. Raikh, and Z. V. Vardeny. Excitations in photonic crystals infiltrated with polarizable media. *Phys. Rev. A*, 64:013809–1–013809–8, 2001.

[86] D. R. Smith, Willie J. Padilla, D. C. Vier, S. C. Nemat-Nasser, and S. Schultz. Composite Medium with Simultaneously Negative Permeability and Permittivity. *Phys. Rev. Lett.*, 84(18):4184–4187, 2000.

[87] D. R. Smith, S. Schultz, P. Markoš, and C. M. Soukoulis. Determination of effective permittivity and permeability of metamaterials from reflection and transmission coefficients. *Phys. Rev. B*, 65(19):195104, 2002.

[88] David R. Smith and Norman Kroll. Negative Refractive Index in Left-Handed Materials. *Phys. Rev. Lett.*, 85(14):2933–2936, 2000.

[89] A. M. Steinberg, P. G. Kwiat, and R. Y. Chiao. Measurement of the Single-Photon Tunneling Time. *Phys. Rev. Lett.*, 71(5):708–711, 1993.

[90] F. H. Stillinger and T. A. Weber. Computer simulation of local order in condensed phases of silicon. *Phys. Rev. B*, 31(8):5262, 1985.

[91] Jason Szeto, Sandra Ramirez-Arcos, Claude Raymond, Leslie D. Hicks, Cyril M. Kay, and Jo-Anne R. Dillon. Gonococcal MinD Affects Cell Division in *Neisseria gonorrhoeae* and *Escherichia coli* and Exhibits a Novel Self-Interaction. *J. Bacteriol.*, 183(21):6253–6264, 2001.

[92] Noboru Takeuchi, A. Selloni, and E. Tosatti. Metallization and Incomplete Melting of a Semiconductor Surface at High Temperature. *Phys. Rev. Lett.*, 72(14):2227–2230, 1994.

[93] A. R. Ubbelohde. *Melting and Crystal Structure.* Oxford University Press, London, 1965.

[94] Alfred René Ubbelohde. *The Molten State of Matter: Melting and Crystal Structure.* John Wiley & Sons, London, 1978.

[95] V. G. Veselago. . *Sov. Phys. Usp.*, 10:509, 1968.

[96] C. L. Woldringh, E. Mulder, J. A. Valkenburg, F. B. Wientjes, A. Zaritsky, and N. Nanninga. Role of the Nucleoid in the Toporegulation of Division. *Res. Microbiol.*, 141(1):39–49, 1990.

[97] Eli Yablanovitch. Inhibited Spontaneous Emission in Solid-State Physics and Electronics. *Phys. Rev. Lett.*, 58(20):2059–2062, 1987.

[98] Yoshiharu Yamaichi and Hironori Niki. Active segregation by the *Bacillus subtilis* partitioning system in *Escherichia coli*. *Proc. Nat. Acad. Sci. USA*, 97(26):14656–14661, 2000.

[99] Xuan-Chuan Yu and William Margolin. FtsZ Ring Clusters in *min* and Partition Mutants: Role of Both the Min System and the Nucleoid in Regulating FtsZ Ring Localization. *Mol. Microbiol.*, 32(2):315–326, 1999.

[100] Weiyi Zhang, An Hu, Xinya Lei, Ning Xu, and Naiben Ming. Photonic band structures of a two-dimensional ionic dielectric medium. *Phys. Rev. B*, 54(15):10280–10283, 1996.

[101] The difference in the periods of MinD-GFP and MinE-GFP oscillations is due solely to the presence of GFP-tagging on only one protein; when both are tagged, they oscillate with the same frequency.